FACULTAD DE CIENCIAS
Departamento de Química Física Aplicada

FISCHER-TROPSCH SYNTHESIS OVER CARBON-SUPPORTED Ru-BASED CATALYSTS

Memoria para aspirar al Grado de

DOCTOR EN CIENCIAS QUÍMICAS

(con Mención Internacional)

José Luis Eslava Castillo

Instituto de Catálisis y Petroleoquímica

Consejo Superior de Investigaciones Científicas

Madrid, 2017

FACULTAD DE CIENCIAS
Departamento de Química Física Aplicada

Memoria para aspirar al Grado de

DOCTOR EN CIENCIAS QUÍMICAS

(con Mención Internacional)

José Luis Eslava Castillo

FISCHER-TROPSCH SYNTHESIS OVER CARBON-SUPPORTED Ru-BASED CATALYSTS

Directores:

Dra. Inmaculada Rodríguez Ramos

Profesora de investigación, CSIC

Dr. Antonio Guerrero Ruiz

Catedrático, UNED

Instituto de Catálisis y Petroleoquímica

Consejo Superior de Investigaciones Científicas

Madrid, 2017

Acknowledgments

Esta Tesis doctoral comenzó en Diciembre de 2012 y no hubiera sido posible sin la ayuda científica y humana de muchas personas a las cuales les estoy muy agradecido.

En primer lugar, me gustaría agradecer a mis directores de tesis, la Dra. Inmaculada Rodríguez Ramos y el Dr. Antonio Guerrero Ruiz. Muchas gracias por la dirección, consejos, apoyo y confianza a lo largo de estos 4 años que ha durado esta tesis doctoral. Muchas gracias por hacerme sentir un miembro más de este grupo de investigación desde el primer día.

Al Dr. Adolfo Arcoya por aconsejarme y animarme durante estos duros años. Han sido muchas las conversaciones compartidas y todas ellas muy fructíferas. A la Dra. Belén Bachiller por su constante disposición y ayuda siempre que fuera necesario. Os estaré agradecido eternamente y aquí me tenéis para lo que esté en mi mano.

Quiero expresar mi agradecimiento a mis compañeros que han formado parte o han pasado por el grupo GDMCH. A los de la UNED: Esther, por su apoyo y ayuda incondicional; María Pérez, por recibirme siempre con una sonrisa y disposición; Eva, por sus útiles consejos; María Almohalla, compañera de nervios y emociones, hemos superado muchos obstáculos y también hemos disfrutado de momentos inolvidables, te doy las gracias por brindarme tu amistad y generosidad, cuenta conmigo siempre que lo necesites; Mariví, llegaste unos meses después pero prácticamente emprendimos juntos este proyecto, siempre tan trabajadora y constante, muchas gracias por tener siempre una sonrisa y hacerme reír, vas a ser una gran investigadora; Ángel, simpatía y caballerosidad; Jesús, bondad y generosidad; Adrián, muchas gracias por transmitirme siempre tanta positividad, eres un hombre con clase y muy seguro de ti mismo, estas dos cualidades te harán llegar muy lejos. A mis compañeros del ICP: Mayka, muchas gracias por tu amistad sincera, eres una mujer grande, cuenta con mi ayuda siempre; Wendy (我餓了); Cristina, puro Málaga, te deseo lo mejor; Carolina, disposición, estoy seguro que te va a ir fenomenal; Nadia, soltura y seguridad; Irene, alegría, we´ll see; Margarida, naturalidad y pasión; Cedric, eterna amistad; Pablo, chico 10; y especialmente a mi compañero de batallas Esteban Gallegos por su continua ayuda. No he conocido a alguien más versátil y resolutivo, estoy seguro que vas a conseguir aquello

que te propongas. Siempre guardaremos en la memoria los momentos vividos y siempre tendréis tú y tu María las puertas de mi casa abiertas.

I am very grateful to Prof. Freek Kapteijn for giving me the opportunity to make a stay in the Catalysis Engineering research group at Delft University of Technology. It was a very fruitful experience and I hope you keep good memories about that period. Prof. Jorge Gascón, muchas gracias por el apoyo, dedicación y consejos que me proporcionaste durante la estancia los cuales fueron fundamentales para obtener buenos resultados. A todos mis compañeros del grupo "Catalysis Engineering", gracias por acogerme, ayudarme y hacerme sentir como si estuviera en casa. Especialmente quiero agradecer a: Els, Bart, Willy, Francesc, Eduardo, Xiahoui, Vjay, Jara, Dimitrii, Tim, Filipe, Elena, Beatriz, Alla, Sonia y Alma.

No me puedo olvidar de la gente que me ha rodeado estos años en el trabajo en Madrid, Dr Marcos Fernández, persona que transmite confianza debido a su sabiduría. Gracias por aconsejarme y tener paciencia aquellos duros días de trabajo en el ESRF. Estoy deseando llevarte a Cádiz y empacharte a pescadito frito junto a un buen vino de mi tierra. Ten cuidado y tráete una Rebequita que allí a veces refresca. Ana Iglesias, una aventura que empezó en el sincrotrón de Grenoble y finalmente terminó en una bonita amistad. Tengo que agradecerte todo lo que me has enseñado, el apoyo y la fuerza que me has transmitido durante esta larga etapa de mi vida. A Mario Jesús Muñoz, una amistad que comenzó en Holanda y que durará toda la vida. Sabes lo importante que eres para mí y aunque nunca tuve a un hermano tú eres lo más parecido a ello. Siempre sabes despejar mis dudas, mis problemas y siempre lo haces con una actitud positiva. A Álvaro Blanco, un conserje excepcional y una brillante persona. Me has demostrado todos estos años la calidad humana que tienes y te puedo asegurar que sin ti y esos momentos de desahogo hubiera sido todo mucho más difícil. Estáis tú y Raquel invitados a Cádiz siempre que queráis. Tengo que agradecer a los chicos superhéroes de mantenimiento: José, Andrés y Eduardo. Ellos son personas imprescindibles en este centro de investigación con los que he tenido la suerte de tener una gran familiaridad. A Armando, encargado del suministro de gases del ICP. Eres una persona cojonuda, he disfrutado mucho contigo jugando a pádel, riéndome de tonterías y contándonos confidencias, te aprecio y deseo mantener esta amistad contigo para siempre. A Conchi Diaz, técnica del XRD. ¿Hay persona que me quiera más en el instituto que tú? Muchas gracias por brindarme siempre una sonrisa y preocuparte tanto por hacer los análisis lo

mejor posible, eres una auténtica profesional. A Rosa, Patricio y José Antonio, gracias por ayudarme siempre que os lo he pedido, gracias por tan fructíferas conversaciones, siempre tendréis a un amigo a vuestra disposición. A Pilar y Aurelio, un matrimonio espectacular, dos personas luchadoras y de mucho valor personal, gracias por tratarme como a un hijo. A Olga, una auténtica castellonense con mucha marcha que siempre muestra una sonrisa en la cara. Me encantaba resolverte y ayudarte con los problemas de laboratorio, siempre estaré a tu disposición. A Uriel, magnífico mexicano, tienes mucho valor y coraje y vas a ser un gran investigador. A Mariela y Lucía, sois la bomba en estado puro, vaya dos personas más majas que llegaron al ICP en la etapa final de mi tesis. Ahora puedo decir a boca llena ¡viva Sevilla! Sería imposible y daría para otra tesis doctoral nombrar a todas las personas que aprecio en el ICP. Todos me habéis demostrado una calidad humana indescriptible y creo que en este centro somos más que trabajadores, somos una gran familia.

A mis profesores de la carrera: Ginesa Blanco, gracias por instruirme en el mundo de la catálisis y por ofrecerme siempre tu ayuda; Roció Litrán, desde nivelación de física me demostraste lo buena persona además de profesora que eres. Gracias por tratarme siempre tan bien; Loli Bellido; no he conocido a alguien con más clase en un laboratorio químico. De ti aprendí a ser cuidadoso y fino. Por supuesto quiero agradecer a todos mis profesores de la Universidad de Cádiz que prestaron su tiempo transmitiéndome los conocimientos que hoy tengo.

A mis profesores del Instituto Drago, especialmente a tres personas que cambiaron mi forma de ver la vida: Charo Sánchez, Eloy Rodríguez y Máximo Manso. Sois los responsables de que me enamorara la ciencia. Charo muchas gracias por enseñarme tan bien química y física, te estaré agradecido toda la vida. Nunca olvidaré aquel examen de inglés en el que andaba justo de tiempo y te quedaste conmigo, tienes un corazón enorme. Eloy, no he vivido nunca clases más productivas a la vez que divertidas, creo que en todas las clases nos sacabas a cada uno lo mejor de nosotros además de varias sonrisas. Nunca olvidaré aquel ascenso del Cádiz C.F. a 1º división que vivimos en el estadio del Chapín. Máximo, confiabas en mí desde el primer día, me decías que era como la hormiguita que guardaba comida para el invierno, poco a poco pero en buena dirección. Magníficas tus clases de filosofía y consejos.

I am very grateful to Alanna de Freitas, she is a great English teacher who has helped to me increasing my English skills during these years. Thank you very much for your help and positive energy.

A mis amigos que me acompañan desde pequeño: Jesús Domínguez, Oscar Carrasco, Oscar Moreno, Fernando García, Alfonso Orellana, Ariana García, Asia Camacho, Rubén Delgado. Muchas gracias por animarme y acompañarme, todos y cada uno de vosotros habéis contribuido a que este trabajo sea hoy una realidad.

Gracias a toda mi familia por su apoyo durante toda mi vida. Especialmente quiero agradecer a mi abuela Nico, una mujer que además de enseñarme muchos valores extraordinarios, era capaz de dar su vida por su nieto. Siempre me acuerdo de ti y sé que me muestras el camino que debo seguir en mi vida. A mis padres, Ana María y José Luis, muchas gracias por levantarme cuando estaba hundido, gracias por la educación maravillosa que me habéis dado y por hacer posible que fuera a Madrid a ampliar mis estudios. Espero haberos hecho sentir felices con mi trabajo y esfuerzo. A mis dos tesoros que tengo como hermanas, Ana María y Patricia, muchas gracias por el continuo apoyo recibido, gracias por diluir mis preocupaciones buscando siempre la forma de hacerme reír, permaneciendo unidos sé que podemos superar todo en la vida. También agradecer a Agustín Grimaldi y a Pablo Galindo por vuestros ánimos recibidos durante todos estos años. A mis tíos y primos, gracias por vuestro aliento y preocupación constante.

A Trini, Aurora y Ángel, no se puede tener un equipo mejor en Madrid. Vaya buenos ratos que hemos compartido tanto gastronómicos como culturales. Muchas gracias por vuestros ánimos y os agradezco enormemente todo lo que habéis hecho por mí.

Por último querría agradecer profundamente a la persona que desde hace 6 años me acompaña en mi vida. Aurora, tú me has enseñado a ser un chico responsable, me ayudaste a superar momentos cruciales en la carrera y ahora lo haces en mi vida. Gracias por mostrarme siempre la mejor solución a mis inquietudes. Te quiero.

A Nico,

A mis padres

"*If you have a positive attitude and constantly strive to give your best effort, eventually you will overcome your immediate problems and find you are ready for greater challenges*".

Pat Riley

"*Everybody is a genius. But if you judge a fish by its ability to climb a tree it will live its whole life believing that it is stupid*"

Albert Einstein

Table of Contents

Chapter 0

Summary/Resumen

Summary and concluding remarks

In order to secure the energy supplies to an increasing population and at the same time limit the damage to Earth, so that future generations may continue to live on a healthy planet, immediate actions are required. The oil is still the main source of obtaining chemicals and fuels but its use is not sustainable from an environmental point of view. The use of fossil fuels is the major contributor to CO_2 emissions (this being an important greenhouse gas). Transport sector is the one most dependent on fossil energy. So, in EU-25 member states transportation stands for 30 % of the total final energy consumption and relies to 98 % on oil, mainly due to its high energy density and hitherto vast concentrated reserves. But, the high and volatile price of crude oil, the concern of governments to ensure the supply of fuels and the increasingly strict environmental laws make necessary to search for alternative energy sources. In this way, a possible alternative to the use of petroleum is the GTL process (Gas-To-Liquids). GTL process includes a set of reactions and chemical operations that transform natural gas, whose main component is methane, in different types of liquid fuels and chemicals highly versatile to the industry. A variant of this technology consists in replacing methane by coal (CTL process, Coal-To-Liquids). But, amongst the alternative energy sources, biomass plays a major role. The only natural, renewable carbon resource and with large options to substitute fossil fuels is biomass. The conversion of biomass into transportation fuels is preferentially done via its gasification into syngas followed by the liquid fuel synthesis. This is the BTL process, Biomass-To-Liquids.

In general these processes will result in an important shift from crude oil to natural gas and coal and finally to bio-wastes, as feedstock for the production of

fuels and chemicals in the decades to come. Industry projections estimate that by 2020 5% of the production of chemicals could be based on Fischer-Tropsch (FT) technology with methane, coal and biomass instead of crude oil refining operations. In the FT synthesis are obtained a complex mixture of hydrocarbons of linear and branched chain, and also oxygenates (alcohols, aldehydes and esters), although the majority are linear paraffins and α-olefins. The hydrocarbons obtained, with a boiling point in the range of gasoline and diesel are high quality because they do not have heteroatoms (S, N), do not contain polyaromatic structures and the fraction of middle distillate presents a high cetane index.

Active elements in FT synthesis are the elements of groups 8-10 of the periodic table, and of them, only the metals: Fe, Co and Ru have the required FT activity for commercial application. Co and Fe are the most commonly employed however, ruthenium catalysts, despite their higher price, possess some unique features in FT synthesis. Ru catalysts possess higher intrinsic activity and can work under higher partial pressures of water or other oxygenate-containing atmospheres, being particularly important for the conversion of syngas produced from biomass. In addition, Ru catalysts are suitable for fundamental research to gain insights into the catalyst functioning and/or reaction mechanisms.

The main objective of this Doctoral Thesis is to comprehend how parameters such as nature of the support, promoters, particle size, morphology and reaction conditions affect to the performance of Ru-based catalysts for the production of hydrocarbons from syngas.

In chapter 4 is presented a time-resolved in situ X-ray absorption spectroscopy (XANES) investigation of the local chemical environment and the electronic structure of the active metal (Ru) and the promoter (Cs) present in

catalysts supported over high-surface-area graphite. XANES analysis at both Ru *K* and Cs L_1 edges was carried out under temperature programmed reduction conditions. This allowed us to find that Ru reduction is a complex process, occurring in two steps via an intermediate oxidation state, and to show the concomitant Cs partial reduction. It is also demonstrated a close association between Cs and Ru atoms as first neighbors. Ru-Cs particle morphology is reversely changed (from flat 2D to 3D shape with low first- and second-shell coordination numbers) when the H_2 atmosphere is switched to CO, staging the strong interaction of CO with the surface of the Ru-Cs nanoparticles supported on graphite, a point confirmed by microcalorimetry of CO adsorption. This in turn results in higher olefin selectivity and more long-chain hydrocarbon production in the Fischer-Tropsch reaction. To our knowledge, this is the first time that this reversible particle reconstruction upon syngas reactant switching has been demonstrated.

In chapter 5, the effect of ruthenium particle size on Fischer-Tropsch synthesis has been studied at 513 K, $H_2/CO = 2$ and 15 bar. The use of a suitable support (graphitic materials) with large surface area and weak interactions with Ru allows to independently study these effects without the influence of parasitic metal-support interactions. Moreover, the effect of promotion with Cs was also evaluated.

It is observed that the turnover frequency (*TOF)* for CO conversion increases significantly with Ru particle size from 1.7 to 7.1 nm or 4.2 to 7.5 nm for non-promoted and promoted catalysts, respectively, and then change slightly up to 12 nm. The selectivity to C_{5+} hydrocarbons increases gradually with the Ru particle size. The olefin to paraffin ratio for Cs-promoted catalysts in the C_2-C_4

hydrocarbons range is independent of the Ru particle size, whereas it decreases for the non-promoted catalysts. Altogether, our results demonstrate the structure sensitive nature of FT reaction over Ru catalysts for Ru particles <7 nm, and highlight the great stability of these catalysts and the potential of Cs promotion for the preferential formation of waxes, even at high conversion levels.

In chapter 6 two different ruthenium and cesium precursors were used to prepare catalysts supported on a high surface area graphite material for application in the Fischer-Tropsch process. In this work we observe significant modifications in the selectivity values for FT reaction depending on the Cs promoter precursor (CsCl vs $CsNO_3$). Specifically the bimetallic catalyst (4Ru-4Cs), prepared from nitrogen containing metal and promoter precursors, showed a high selectivity to CO_2 provably result of the water gas shift reaction (WGS).

XANES analysis at Cs L_1 edge was recorded during the temperature-programmed reduction (TPR), observing a partial reduction of the CsCl species for the 4Ru-Cl-4Cs-Cl catalyst. By contrast, for the 4Ru-N-4Cs-N sample similar Cs spectrum with equal absorption edge energy values were observed along all the H_2 TPR which is attributed to the formation of hardly reducible CsOH and Cs_2O species over the catalyst surfaces as consequence of the $CsNO_3$ precursor decomposition. These species are able to adsorb water molecules (co-product of the FT reaction), and then these water intermediates can interact with the CO molecules adsorbed on the Ru nanoparticles improving the WGS reaction and giving place to undesired production of CO_2.

Finally, **in chapter 7** molybdenum promotion effect on ruthenium based FT catalysts is investigated. The effects of Mo loading (0-5 wt%) on Ru (2 wt%) were studied at 523 K, H_2/CO = 2 and 3.5 bar. Mean diameters of Ru were all

close to 3 nm independently of the molybdenum loading used. The presence of molybdenum in a bimetallic ruthenium-molybdenum catalyst improved the catalytic behavior of ruthenium in terms of catalytic activity (more than four times), long-chain hydrocarbon selectivity and the olefin-to-paraffin ratio. Microcalorimetric characterization during CO adsorption at 331 K revealed a clear interaction between Ru and Mo observing an important increase of CO adsorption heats when Mo/Ru ratio was ≤ 0.26. This fact was explained because CO molecules might bind to metal oxides of Mo through the O atom while being simultaneously bound to the Ru metal through the C atom increasing significantly the adsorption heat. X-ray photoelectron spectroscopy analysis, performed to 2Ru0.5Mo/G catalyst after in-situ H_2 reduction treatment, determined the presence of Mo^{VI} (MoO_3) and Mo^{IV} (MoO_2), MoC and Mo^0 species on the catalyst surface. It is considered that Mo particles could be located around the ruthenium nanoparticles acting as a Lewis acid and therefore facilitating the CO dissociation. These conclusions represent a major contribution to the understanding of the Mo promotion effect in the FT process because realistic deductions have been obtained using a proper inert support.

Resumen y aspectos más relevantes

Con el fin de asegurar el suministro de energía a una población cada vez mayor y al mismo tiempo limitar el daño a la Tierra, para que las generaciones futuras puedan seguir viviendo en un planeta saludable, se requieren acciones inmediatas. El petróleo sigue siendo la principal fuente de obtención de productos químicos y combustibles, pero su uso no es sostenible desde el punto de vista medioambiental. Así, el uso de combustibles fósiles es el principal contribuyente de las emisiones de CO_2 (siendo éste un importante gas de efecto invernadero). El sector del transporte es el que más depende de la energía fósil. Por lo tanto, en los estados miembros de la UE-25, el transporte representa el 30% del consumo total de energía siendo en un 98% procedente del petróleo. Esto se debe principalmente a su alta densidad energética y a la, hasta la fecha, concentración de vastas reservas. Pero, el alto y volátil precio del petróleo crudo, la preocupación de los gobiernos de asegurar el suministro de combustibles y las leyes ambientales cada vez más estrictas hacen necesario buscar fuentes alternativas de energía. De esta manera, una posible alternativa al uso del petróleo es el proceso GTL (Gas-To-Liquids). El proceso GTL consiste en un conjunto de reacciones y operaciones químicas que transforman el gas natural, cuyo principal componente es el metano, en diferentes tipos de combustibles líquidos y químicos altamente versátiles para la industria. Una variante de esta tecnología consiste en sustituir el metano por el carbón (proceso CTL, Carbon-To-Liquids). Pero, entre las diferentes fuentes alternativas de energía, la biomasa juega un papel fundamental siendo el único recurso de carbono natural, renovable y con grandes opciones de sustituir a los combustibles fósiles. La conversión de biomasa en combustibles para el transporte se realiza preferentemente a través de su gasificación en gas de síntesis seguida de

la síntesis del combustible líquido. Este proceso se conoce como BTL, Biomass-To-Liquids.

En general, estos procesos darán lugar a un cambio importante reemplazando el petróleo crudo por gas natural y carbón, apuntando finalmente hacia la biomasa, como fuente de materia prima para la producción de combustibles y productos químicos en las próximas décadas. Las proyecciones de la industria estiman que para 2020 el 5% de la producción de productos químicos podría basarse en la tecnología de Fischer-Tropsch (FT) usando metano, carbón y biomasa en lugar de operaciones de refinado de crudo. En la síntesis de FT se obtiene una mezcla compleja de hidrocarburos de cadena lineal y ramificada, y también compuestos oxigenados (alcoholes, aldehídos y ésteres), aunque la mayoría son parafinas lineales y α-olefinas. Los hidrocarburos obtenidos, con un punto de ebullición en el rango de la gasolina y el gasóleo son de alta calidad porque no poseen heteroátomos (S, N), no contienen estructuras poliaromáticas y la fracción de destilado medio presenta un alto índice de cetano.

Los elementos activos en la síntesis de FT son los elementos de los grupos 8-10 de la tabla periódica, y de ellos, sólo los metales: Fe, Co y Ru tienen la actividad requerida en FT para su aplicación comercial. Co y Fe son los más comúnmente empleados sin embargo, los catalizadores de rutenio, a pesar de su precio más alto, poseen algunas características únicas en la síntesis FT. Ru posee una actividad intrínseca superior y puede trabajar bajo presiones parciales más altas de agua u otras atmósferas que contienen oxígeno, siendo particularmente importante para la conversión de gas de síntesis producido a partir de biomasa. Además, los catalizadores de Ru son adecuados para la investigación fundamental

permitiendo obtener conocimientos sobre el funcionamiento del catalizador y/o los mecanismos de reacción.

El objetivo principal de esta Tesis Doctoral es comprender el modo en que parámetros, tales como, naturaleza del soporte, promotores, tamaño de partícula, morfología y condiciones de reacción afectan al rendimiento de los catalizadores basados en Ru para la producción de hidrocarburos a partir del gas de síntesis.

En el capítulo 4 se presenta una investigación (in-situ) de absorción de rayos X (XAS) del entorno químico local y de la estructura electrónica del metal activo (Ru) y del promotor (Cs) presentes en catalizadores soportados sobre un grafito de alta superficie. Los análisis XANES realizados en ambos bordes, Ru-*K* y Cs-L_1, se llevaron a cabo en condiciones de reducción a temperatura programada. Esto nos permitió descubrir que la reducción de Ru es un proceso complejo ocurriendo en dos etapas a través de un estado intermedio de oxidación, y se confirmó la reducción parcial de Cs. También se demuestra una estrecha asociación entre los átomos de Cs y Ru en la primera esfera de coordinación. La morfología de las partículas de Ru-Cs se transforma de forma reversible (desde la forma plana 2D, a la 3D con bajos números de coordinación en la primera y segunda capa) cuando la atmósfera de H_2 se cambia a CO, poniendose de manifiesto la fuerte interacción del CO con la superficie de las nanopartículas Ru-Cs soportadas sobre grafito, hecho confirmado mediante microcalorimetría de adsorción de CO. Esto a su vez resulta en una mayor selectividad a olefinas y una mayor producción de hidrocarburos de cadena larga durante la reacción de Fischer-Tropsch. Hasta donde sabemos, esta es la primera vez que se demuestra esta reconstrucción reversible de partículas tras el intercambio entre los reactantes que componen el gas de síntesis.

En el capítulo 5, se ha estudiado el efecto del tamaño de partícula de rutenio en la síntesis de Fischer-Tropsch a 513 K, $H_2/CO = 2$ y 15 bar. El uso de un soporte adecuado (materiales grafíticos) con gran área superficial que muestre débiles interacciones con el Ru permite estudiar independientemente estos efectos evitando la influencia de las interacciones parásitas entre el metal y el soporte. Además, se evaluó el efecto de la promoción de Ru con Cs.

Se ha observado que el número de moléculas convertidas de CO por centro activo superficial en la unidad de tiempo (TOF) aumenta significativamente con el tamaño de partícula de Ru desde 1,7 hasta 7,1 nm o desde 4,2 hasta 7,5 nm, dependiendo si se usan catalizadores de Ru no promovidos o promovidos respectivamente, y se modifica levemente hasta tamaños de partículas de 12 nm. La selectividad hacia hidrocarburos C_{5+} aumenta gradualmente con el tamaño de partícula Ru. La relación de olefinas y parafinas en el rango C_2-C_4 para catalizadores promovidos con Cs es independiente del tamaño de partícula del Ru, mientras que esta disminuye para los catalizadores no promovidos. En conjunto, nuestros resultados demuestran la naturaleza sensible a la estructura de la reacción de FT sobre los catalizadores de Ru para partículas de Ru <7 nm y destacan la gran estabilidad de estos catalizadores y el potencial de la promoción con Cs para conseguir preferentemente la formación de ceras, incluso trabajando a altos niveles de conversión.

En el capítulo 6 se utilizaron dos precursores diferentes de rutenio y cesio para la preparación de catalizadores soportados sobre un grafito de alta superficie y finalmente se aplicaron en el proceso Fischer-Tropsch. En este trabajo observamos significativas modificaciones en los valores de selectividad en la reacción de FT dependiendo del precursor del promotor de Cs empleado (CsCl vs

$CsNO_3$). Concretamente, el catalizador bimetálico (4Ru-4Cs), preparado a partir del precursor nitrato del metal y del promotor, mostró una alta selectividad hacia CO_2, como resultado de la reacción de desplazamiento de gas de agua (WGS).

Se registraron análisis XANES en el borde Cs-L_1 durante la reducción a temperatura programada (TPR), observándose una reducción parcial de la especie CsCl en el catalizador 4Ru-Cl-4Cs-Cl. Por el contrario, en la muestra 4Ru-N-4Cs-N se observó un espectro de Cs similar durante todo el proceso de reducción en H_2 con valores de energía en el borde de absorción prácticamente iguales, esto se atribuye a la formación de especies de CsOH y Cs_2O, apenas reducibles, originadas durante la descomposición de la sal de $CsNO_3$. Estas especies son capaces de adsorber moléculas de agua (subproducto de la reacción de FT) que podrían interaccionar con las moléculas de CO adsorbidas sobre las nanopartículas de Ru promoviendo la reacción de WGS y por lo tanto dando lugar a la producción no deseada de CO_2.

Finalmente, en el capítulo 7 se investigó el efecto promotor del molibdeno sobre el rutenio durante la reacción de FT. Se estudiaron los efectos de la carga de Mo (0-5% en peso) sobre Ru (2% en peso) a 523 K, H_2/CO = 2 y 3,5 bar. Los diámetros medios de Ru fueron todos cercanos a 3 nm independientemente de la carga de molibdeno utilizada. La presencia de molibdeno en el sistema bimetálico Ru-Mo mejoró el comportamiento catalítico del rutenio en términos de actividad (en más de cuatro veces), selectividad hacia hidrocarburos de cadena larga y la relación entre olefinas-parafinas. La caracterización mediante microcalorimetría de quimisorción de CO a 331 K reveló una clara interacción entre Ru y Mo observándose un importante aumento de los calores de adsorción de CO cuando la relación Mo/Ru fue $\leq$ 0,26. Este hecho fue explicado porque las moléculas de CO

podrían unirse a los óxidos de Mo a través del átomo de O mientras que al mismo tiempo enlazarse al metal de Ru a través del átomo de C aumentando significativamente el calor de adsorción. El análisis de XPS realizado a la muestra 2Ru0,5Mo/G después de la reducción in-situ en H_2, determinó la presencia de Mo^{VI} (MoO_3) y Mo^{IV} (MoO_2), MoC y Mo^0 en la superficie del catalizador. Se considera que las partículas de Mo podrían estar localizadas alrededor de las nanopartículas de rutenio actuando como un ácido de Lewis y por lo tanto facilitando la disociación de CO. Estas conclusiones representan una importante y realista contribución para la comprensión del efecto promotor del Mo en el proceso de FT, ya que estas deducciones fueron obtenidas usándose un soporte adecuado e inerte.

Chapter 1

Introduction

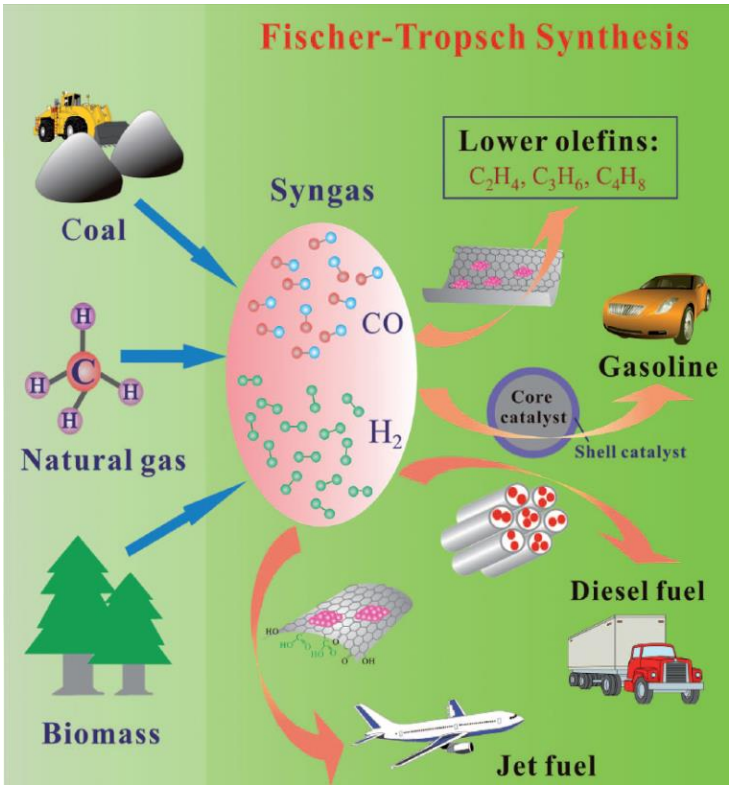

Obtained from reference [138].

1.1. Current energy situation. Obtaining synthetic liquid fuels.

Nowadays, the oil is still the main source of obtaining chemicals and fuels but its use is not sustainable from an environmental point of view. The high and volatile price of fossil fuels (figure 1.1), the concern of governments to ensure the supply of fuels and the increasingly strict environmental laws make necessary to search for alternative energy sources. World energy consumption is continuously growing and it is partly due to emerging countries like China (in 2010 it has become the largest consumer of global energy [1]), India or Brazil. So it is required to establish a sustainable development to reach the agreements on greenhouse gas emissions effects established in the Kyoto protocol in 1997 [2].One of the main focal points of energy demand is the transport sector. Waiting for an enough development of alternative technologies such as renewable H_2 production and their use in fuel cells, synthetic liquid fuels are those that will face this increase in energy demand (in the transport sector) during this century. The recent report: Annual Energy Outlook 2015 from U.S. Energy Information Administration [3] indicates that liquid fuel consumption for transport is going to grow since 13.41 million barrels per day in 2012 to 13.90 in 2020. It is here where the collectively referred to as feed-to-liquids (XTL) conversion processes have a particular relevance. Feed stock from various sources can be used: natural gas, coal or biomass.

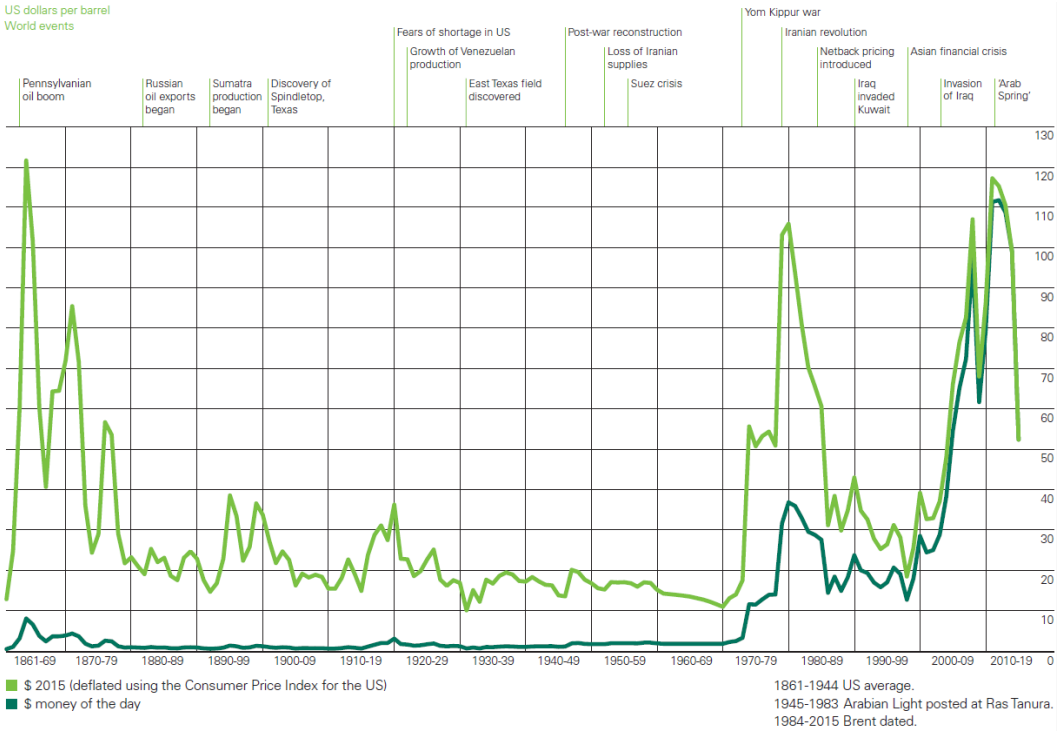

Figure 1.1. Crude oil prices 1861-2015 (U.S. dollars per barrel) [4].

In this way, a possible alternative to the use of petroleum is the GTL process (**G**as-**T**o-**L**iquids). GTL process includes a set of reactions and chemical operations that transform natural gas, whose main component is methane, in different types of liquid fuels and chemicals highly versatile to the industry. A variant of this technology consists in replacing methane by coal (CTL process, **C**oal-**T**o-**L**iquids), or biomass (BTL process, **B**iomass-**T**o-**L**iquids) in order to obtain liquids fuels. It should be taken into account that in order to these processes be sustainable it is necessary to capture and store the CO_2 produced. When synthetic liquids are produced from coal without CO_2 capture, the emissions are twice those emitted when the fuels are obtained from petroleum. Regarding BTL process, net emissions of CO_2 are smaller than those produced by conventional processes becoming negative if CO_2 is captured and stored. But nevertheless, this process is limited by the amount of biomass that can be stored in a specific place

and furthermore BTL plants can convert only one third part of carbon contained in the biomass into liquid fuels [5]. GTL technology is a fact; currently two companies have implemented this process industrially (Sasol in South Africa and Shell in Malaysia) and others are being implemented in areas where natural gas reserves are important. Companies in the oil sector such as: ExxonMobil, British Petroleum, Syntroleum, Chevron, etc, are designating significant resources to the development of this process and some of them are in the construction phase of the industrial plant [6].

The XTL developed processes depends mainly on the following factors:

a) Global reserves of fossil fuels.

b) Location of these reserves.

c) Demand for cleaner fuels.

a) Global reserves of fossil fuels. The Statistical Review of World Energy 2015 [4] estimated that the relationship between the proven reserves and the production by the end of 2015 is twice greater for coal and slightly higher for natural gas in relation to oil. This way of expressing the fossil fuel reserves provides an estimate of the time it would take to sell out if production is maintained at the same level. However, every year new natural gas reserves are discovered whereas petroleum ones are practically deadlocked. In the not too distant future it is expected that natural gas becomes very important in the energy sector as a primary carbon source, so that GTL process will be an essential route.

b) Location of these reserves. The world's major reserves of natural gas are concentrated in the Middle East, Russia and North Africa (figure 1.2), while the major consumer are located in Europe and North America (figure 1.3). The transportation of natural from production area to consumer countries requires a

very expensive physical process of liquefaction which limits this option. However, the chemical liquefaction through the GTL technology considerably reduces the cost of transportation.

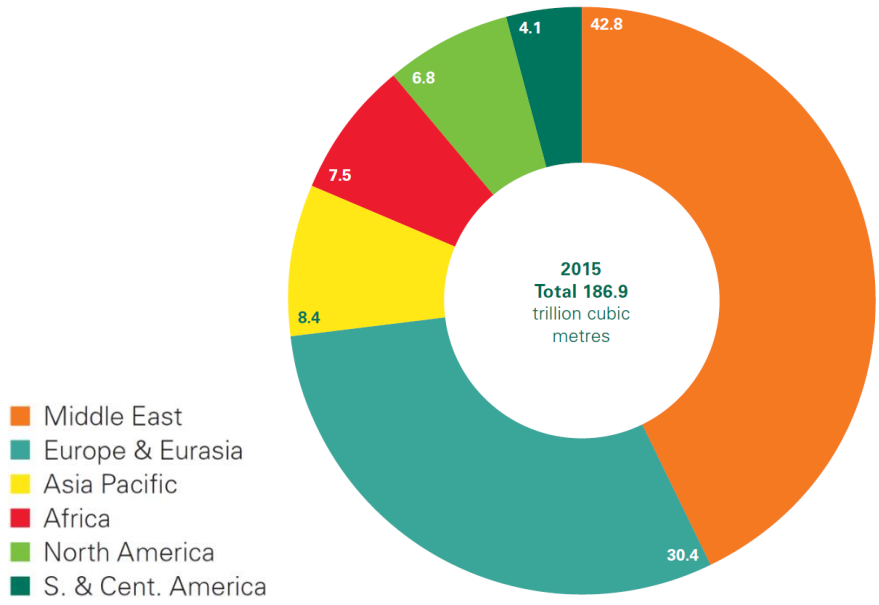

Figure 1.2. Proved reserves of natural gas in 2015 [4].

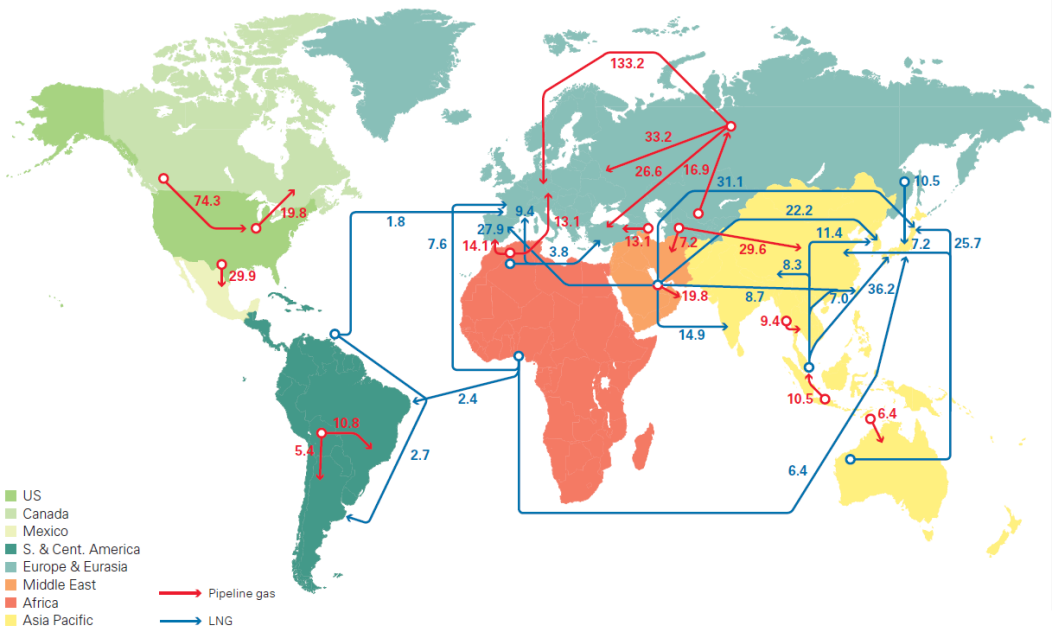

Figure 1.3. Major trade movements in 2015 (billion cubic metres) [4].

On the other hand, the fact that great coal reserves exist in places like China, India, Australia, South Africa and the United States, together with the significant advances in clean combustion technologies make reasonably attractive the use of coal as a source of fossil energy. But to avoid the massive emissions of CO_2, SO_2 and NO_x inherent in coal combustion, applied technologies for the capture of these gaseous pollutants must be performed in streams afterburner. An example of liquid fuels production using CTL process and electricity through combined cycle has recently been proposed as a clean and efficient solution [7].

c) Demand for cleaner fuels. Generally, automotive fuels derived from the distillation of petroleum contain high levels of aromatic hydrocarbons and hetero-atoms of nitrogen and sulfur compounds. Besides the new oil wells have more and more unwanted products. All these compounds are sources of additional pollution to own CO_2 emissions. Therefore, it is essential to carry out different processes in refineries for disposal (hydrodearomatization, hydrodenitrogenation and hydrodesulfurization) [7]. Environmental legislations are becoming every time less permissive at this point. Therefore, as it is shown in Table 1.1, the maximum permitted of sulfur level in gasoline and diesel should be reduced drastically in the European Union [8]. This implies that purification processes of fuels are increasingly complex and expensive. However, through the GTL, CTL and BTL routes, clean mixtures of hydrocarbons free of aromatics and compounds containing nitrogen or sulfur are obtained.

Table 1.1. Evolution of the maximum S levels in the European Union (ppm).

Fuel	1994	1996	2000	2005	2011*
Gasoline 95/85, CEN228	1000	500	150	50	10
Diesel CEN590	2000	500	350	50	10

* These levels have been maintained since 2011.

1.2. Syngas Production.

Synthesis gas or syngas is a gaseous mixture of carbon monoxide and hydrogen ($CO + H_2$) wherein the molar ratio depends on the carbon source from which it is obtained. Synthesis gas can be obtained from natural gas, coal or biomass. Coal gasification is a process used since 1850 when the gases derived from gasification process were used in the heating and lighting of various British and American cities. However, it was in the early twentieth century when it began to be used on a large scale for the production of synthetic fuels [9]. Throughout the 1935-1945 in Germany coal was used due to the abundant reserves of this fossil precursor and the inaccessibility of petroleum. A similar situation occurred in South Africa since 1955 where it even at the present keeps on applying commercially. Today, because of economic reasons and CO_2 emission regulations, the predominant technology for obtaining syngas is from natural gas [10]. The biomass is still not used commercially for obtaining syngas but it has recently been demonstrate its application at the laboratory scale [11].

There are three main routes to obtain syngas from natural gas: (i) methane steam reforming (SR), (ii) dry reforming (DR) and (iii) partial oxidation of methane (POM). The predominant technology is methane steam reforming (SR). In this process, a mixture of methane and water is reacted on a Ni catalyst at temperatures in the range 1073-1173 K and operating pressure between 1-3 MPa, obtaining carbon monoxide and hydrogen in accordance with the reaction:

$$CH_4 + H_2O \rightarrow CO + 3\ H_2 \qquad (\Delta H = 226\ kJ/mol) \qquad [1.1]$$

This route of synthesis gas production, despite being the most widely used commercially, has a number of disadvantages. It is a highly endothermic reaction, that is, it requires the input of large amount of energy. Moreover, the molar ratio

of H_2/CO obtained is close to 3 and that is too high to be used directly in the conventional Fischer-Tropsch synthesis reactor.

The reforming process of methane with carbon dioxide (DR) is a possibility to produce rich CO synthesis gas (H_2/CO = 1), that it may be advisable to the production of high molecular weight hydrocarbon [12]. The reaction is, as in steam reforming, a highly endothermic process:

$$CH_4 + CO_2 \rightarrow 2\ CO + 2\ H_2 \qquad (\Delta H = 247\ kJ/mol) \qquad [1.2]$$

This process can also be used to reduce emissions of CO_2 and CH_4, two gases that contribute to the greenhouse effect [13,14]. Nevertheless, dry reforming process provides a ratio H_2/CO too low to feed it directly into a conventional Fischer-Tropsch synthesis reactor.

In the partial oxidation of methane is reacted a mixture of methane and pure oxygen in the molar ratio $CH_4/O_2 = 2$ on a metal catalyst, which is usually nickel or a noble metal such as Rh, in the temperature range from 1073-1173 K and at atmospheric pressure [15, 16]:

$$CH_4 + \tfrac{1}{2}\ O_2 \rightarrow CO + 2\ H_2 \qquad (\Delta H = -22\ kJ/mol) \qquad [1.3]$$

This reaction has the advantage of being an exothermic process so the reaction equipment design can be more compact. The H_2/CO ratio obtained it is suitable for Fischer-Tropsch synthesis [17] or methanol synthesis [18]. But, the major drawback is the need to install an oxygen plant which increases the costs.

In general terms, production of purified synthesis gas in a commercial GTL plant represents approximately 60% of the overall cost [19] which gives an idea of the importance of this stage when it comes to ensuring the economic viability of a plant. Researches in this direction are being made with the aim of reducing the energy cost of this process.

1.3. Fischer-Tropsch Synthesis (FTS).

1.3.1. Brief history and main reactions

Franz Fischer, head of the Max-Planck Institut für Kohlenforschung in Mülheim (Germany) and Hans Tropsch, a co-worker of Fischer and professor of chemistry in Prague (Czech Republic), Mülheim (Germany) and Chicago (Illinois, USA), discovered in 1922 a catalytic reaction between CO and H_2, which yields mixtures of higher alkanes and alkenes [20, 21, 22, 23]. This invention made possible for Germany to produce fuels from its coal reserves and by 1938 nine Fischer-Tropsch (FT) plants were in operation having a combined capacity of about 660 x 10^3 t per year [24].The expansion of these plants stopped around 1940, but existing plants continued to operate during World War II. It is worthwhile to notice that in 1944, Japan was operating three FT plants based on coal reserves. Whilst being a major scientific as well as a technical success, the FT process could not compete economically with the refining process of crude oil, which becomes important starting from the 1950s. All this coincided with major discoveries of oil fields in the Middle East and consequently the price of crude oil dropped. Although a new FT plant was built in Brownsville (Texas, USA) in 1950, the sharp increase in the price of methane caused the plant to shut down. Thus, due to bad economics FT technology became of little importance for the industrial world after World War II and no new FT plants were constructed. An exception was South Africa, which started making fuels and chemicals from gasified coal based on the FT process a half century ago due to embargoes initiated by the country's apartheid policies. Till today, South Africa's Sasol (South African Coal, Oil and Gas Corporation, Ltd.), which built its first

commercial FT plant in 1955, Exxon Mobil and Shell Global Solutions are known as the major players in this field [25, 26].

The world oil crisis in 1973 led developed countries to conclude the need to search for alternative energy sources to petroleum. One of the options was the reactivation and relaunching of the FT process oriented towards the synthetic fuel production. This impetus continues today, such as it is reflected in the operating industrial plants and forecasts for the construction in the near future (see table 1.2.).

Table 1.2. Main companies involved in the Fischer-Tropsch synthesis for the production of synthetic fuels and chemicals [27, 28, 29].

Company	Country	Capacity (barrels/day)	Syngas source
Sasol	South Africa	150.000	Carbon
	China	160.000	Carbon
	Australia	30.000	Natural Gas
	Nigeria	34.000	Natural Gas
	Qatar	34.000	Natural Gas
Shell	Malaysia	12.500	Natural Gas
	Qatar	140.000	Natural Gas
	Indonesia	75.000	Natural Gas
	Iran	70.000	Natural Gas
	Egypt	75.000	Natural Gas
	Argentina	75.000	Natural Gas
	Australia	75.000	Natural Gas
Shell; Choren	Germany	300	Biomass
Mossgas	South Africa	22.500	Natural Gas
Eni Technologie	Italy	20	Natural Gas
BP	USA	300	Natural Gas
Rentech	USA	1.000	Natural Gas
	South Africa	10.000	Natural Gas
	Bolivia	10.000	Natural Gas
Rentech; Pertamina	Indonesia	15.000	
Syntroleum	USA	70	Natural Gas
	Australia	11.500	Natural Gas
	Chile	10.000	Natural Gas
	Peru	5.000	Natural Gas
Gazprom; Syntroleum	Russia	13.500	Natural Gas
Repsol-YPT;	Bolivia	13.500	Natural Gas
Syntroleum	Bolivia	90.000	Natural Gas
ExxonMobil	Qatar	90.000	Natural Gas
Conoco	Qatar	60.000	Natural Gas
	USA	400	Natural Gas

It is remarkable to notice that there is today a renewed interest in FT technology mainly due to:

i. The rising costs of crude oil. For some time now, the oil prices are well above $ 50 per barrel.

ii. The drive to supply environmentally friendly automotive fuels, more in particularly, the production of synthetic sulphur-free diesel, especially interesting for the European car fleet.

iii. The commercialization of otherwise unmarketable natural gas at remote locations. CO_2 emission regulations will certainly lead in the future to a ban on natural gas flaring near crude oil production wells.

This will result in an important shift from crude oil to natural gas and coal as well as bio-wastes, as feedstock for the production of fuels and chemicals in the decades to come [30, 31, 32, 33]. Industry projections estimate that by 2020 5% of the production of chemicals could be based on FT technology with methane and coal instead of crude oil refining operations.

In the FT synthesis are obtained a complex mixture of hydrocarbons of linear and branched chain, and also oxygenates (alcohols, aldehydes and esters), although the majority are linear paraffins and α-olefins. The hydrocarbons obtained, with a boiling point in the range of gasoline and diesel are high quality because they do not have heteroatoms (S, N), do not contain polyaromatic structures and the fraction of middle distillate presents a high cetane index. The reactions involved in the FT synthesis are numerous and complex, the most important are summarized in Table 1.3.

Table 1.3. Major overall reactions in the Fischer-Tropsch Synthesis [34].

Main reaction	
Paraffins	$(2n+1)H_2 + nCO \rightarrow C_nH_{2n+2} + nH_2O$
Olefins	$2nH_2 + nCO \rightarrow C_nH_{2n} + nH_2O$
Water gas shift reaction (WGS)	$CO + H_2O \leftrightarrow CO_2 + H_2$
Side reaction	
Alcohols	$2nH_2 + nCO \rightarrow C_nH_{2n+2} + (n\text{-}1)H_2O$
Boudouard reaction	$2CO \rightarrow C + CO_2$
Modification of the catalyst	a. $M_xO_y + y\ H_2 \leftrightarrow xM + y\ H_2O$
Oxidation /Reduction catalyst	b. $M_xO_y + y\ CO \leftrightarrow xM + y\ CO_2$
Carbide formation	$xM + yC \rightarrow M_xC_y$

1.3.2. Reaction Mechanism

Fischer-Tropsch synthesis is a polymerization reaction including the following steps [35]: a) reactant adsorption, b) chain initiation, c) chain growth, d) chain termination, e) product desorption and f) readsorption and further reaction. Although the reaction has been known for almost 100 years, there is still much controversy about the nature of the monomer species and the road that follows the growth of a hydrocarbon chain [34, 35, 36, 37, 38]. Traditionally, three mechanisms have been proposed:

1. **Carbide mechanism.** This mechanism was initially proposed by Fisher and Tropsch [39] and still remains the most accepted regarding the formation of hydrocarbons from H_2/CO using catalysts based on Fe, Co and Ru. This mechanism involves the adsorption of CO and its subsequent dissociation, followed by the reaction between carbon (C*) and hydrogen

(H*) to form the reaction monomers (CH_2*), the asterisk refers to a surface species adsorbed in an active catalytic center. These species polymerize by adding more monomers resulting in long chains. Presence of methylenes groups have been identified using transient isotopic techniques over Ru/SiO_2, Ru/Al_2O_3 and Fe/Al_2O_3 catalysts [40, 41, 42, 43]. Chain growth ends by the removal or addition of hydrogen to form olefins or paraffins respectively [44]. However, this reaction mechanism does not explain the formation of oxygenates compounds which are also a reaction coproduct.

2. **Hidroxi-carbenes mechanism.** This mechanism suggests the formation of a hydroxy-carbene (CHOH*) as reaction intermediate. This species is formed by the partial hydrogenation of undissociated CO adsorbed. C-C link is produced by the condensation of two hydroxy-carbenes with the subsequent elimination of H_2O. This model explains the formation of hydrocarbons and oxygenates compounds [45].
3. **CO insertion mechanism.** In this mechanism, the chain growth occurs by insertion of a carbonyl intermediate (M-CO) in a metal-alkyl chain link [46]. Subsequently, these species undergo various reactions to form acids, aldehydes, alcohols and hydrocarbons.

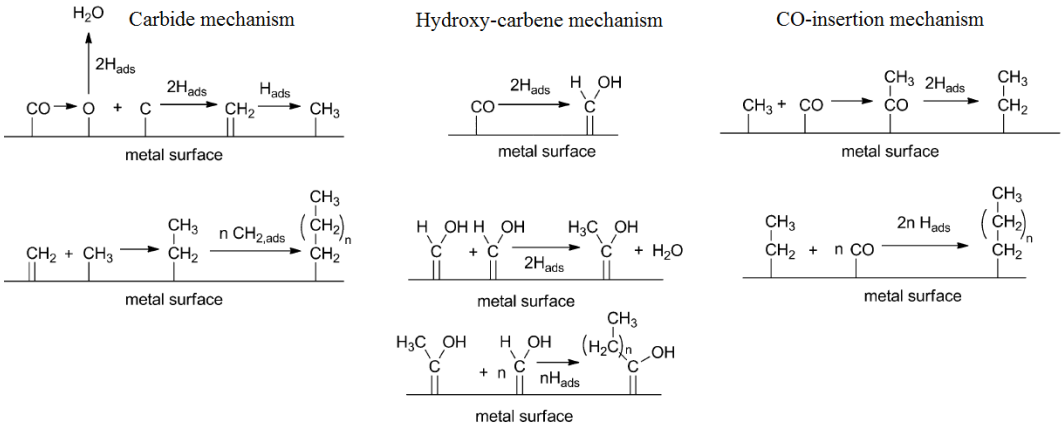

Figure 1.4. Different mechanisms proposed for the Fischer-Tropsch synthesis on heterogeneous catalysts [47].

All mechanisms share the idea of the presence of a reaction intermediate responsible for the chain growth (CH_2*, CHOH* or CO*). However, none of them is able to explain by itself the great diversity of products formed in the Fischer-Tropsch synthesis, so some researchers have proposed other mechanisms where participate more than a reaction intermediate. According to Dry [48] hydrocarbons are produced by insertion of -CH_2- units in alkyl chains, whereas insertion of CO produces oxygenates compounds. Biloen and Sachtler have proposed similar mechanisms [49].

In the case of Ru catalysts, recent theoretical studies suggest that the CO hydrogenation occurs through carbides mechanism or by means of hydrogen-assisted CO dissociation [50, 51, 52, 53]. The relevance of each CO dissociation route depends on the type of center where the CO is adsorbed. Thus, several authors have found that on Ru particles terraces, hydrogen-assisted CO dissociation pathway is more energetically favored than direct dissociation of CO [50, 51, 54, 55] while on the Ru particles defects (corners and edges) the most favored mechanism is the direct dissociation of CO [50, 51, 52, 56, 57].

In addition to the primary reactions explained above, many other mechanistic analyses indicate the presence of side reactions during the synthesis of FT. These reactions occur when α-olefins (one of the primary reaction products) are readsorbed in the surface active centers before leaving the reactor being able to experience reactions such as: isomerization to internal olefin, cracking and hydrogenolysis, hydrogenation to paraffin, insertion into a chain of growth and the beginning of a new chain [58, 59].

In the mechanistic study of FT synthesis it is also important to consider the mechanism of the water gas shift reaction (WGS) because of it is a main reaction in the process (see table 1.3). The study of WGS is essential for catalysts of Fe for the reason that these systems are active in the reaction raising the ratio H_2/CO. On the contrary, other catalyst systems such as Co and Ru hardly exhibit activity in the WGS reaction [60]. Since in this thesis the catalysts studied are based on Ru and this is not active in this reaction, non-detailed explanation of the various mechanisms that have been proposed for this reaction is going to be made, although it is possible to find more information in the following references [61, 62, 63, 64].

1.3.3. FT products distribution

The Fischer-Tropsch reaction produces a wide range of hydrocarbons and oxygenated products via primary and/or secondary reactions. The selectivity for these various products appears to be controlled by mechanistic and kinetic factors of the various reactions occurring during FT synthesis [65]. The spread in carbon number products is dependent on the type of catalyst, the operating temperature and/or pressure, the type or amount of catalyst promoter, the feed gas composition

or the type of reactor [66]. Figure 1.5 presents the different product fractions obtained via FT from syngas.

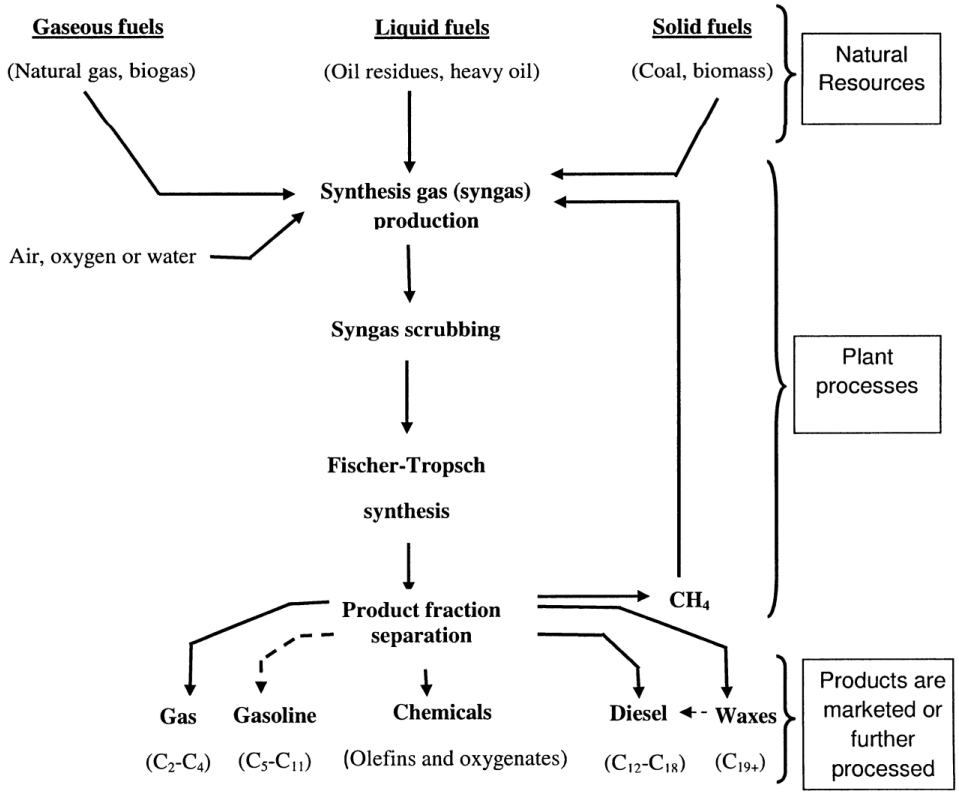

Figure 1.5. Industrial process overview for the production of fuels and chemicals by FTS [67].

Although these parameters have a big influence in product selectivity, all the proposed FT reaction mechanisms compare the FT synthesis to a conventional polymerization process with the assumption that chain growth occurs by stepwise insertion of the -CH_2- monomer chemisorbed on the catalyst surface into the chain, which is well suited for selectivity modelling [68].

1.3.3.1. Ideal distribution model (Anderson-Schulz-Flory distribution)

Approximately, the molar amount of the sums of products in individual carbon number fractions declines exponentially with carbon number. This

behaviour, which is indicative of a polymerization reaction that proceeds stepwise from a C_1 monomer, was originally noticed by Herrington [69], Friedel and Anderson [70]. In the ideal case where the chain growth probability (α) of surface species is independent of the carbon number (n), the products distribution in FT synthesis is determined by the expression:

$$W_n = n \cdot (1-\alpha)^2 \cdot \alpha^{n-1} \qquad [1.4]$$

The complete derivation of this equation was first developed by Schulz [71] and Flory [72]. *Wn* is the fraction in weight of chains with n carbons atoms, *n* is the number of carbon atoms in a chain and α is the chain growth probability to pass from n to n+1 carbon atoms. Figure 1.6 shows the hydrocarbon selectivity as function of α.

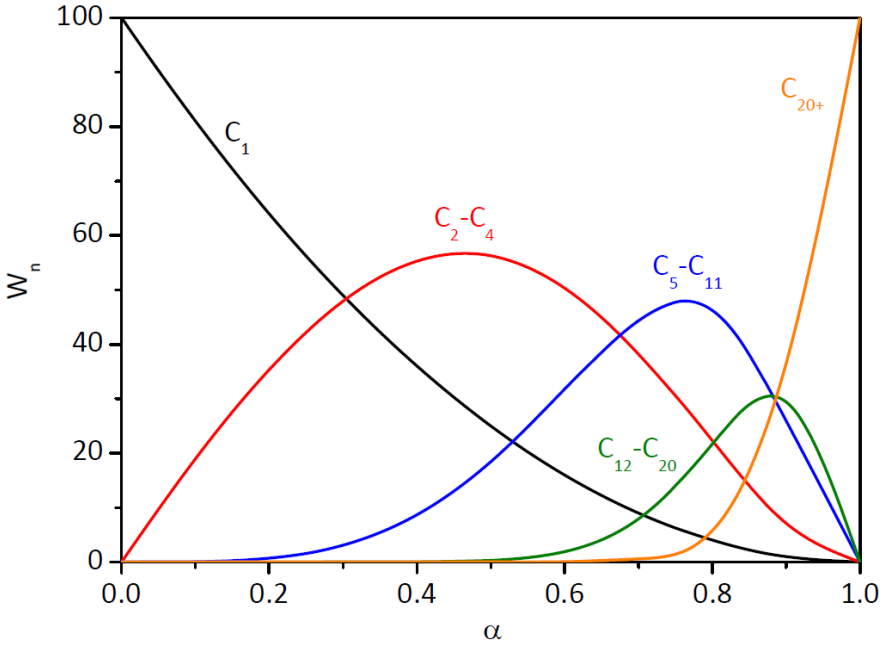

Figure 1.6. Hydrocarbon selectivity as function of the chain growth probability factor α [27,73].

The probability of the chain growth or α parameter determines the product distribution and is defined by the following expression:

$$\alpha_n = \frac{\sum_{i=n+1}^{\infty} \phi_i}{\sum_{i=n}^{\infty} \phi_i} = \frac{K_{p,n}}{K_{p,n} + K_{t,n}} \qquad [1.5]$$

Wherein $k_{p,n}$ is the velocity of propagation of the chain growth of n carbon, $k_{t,n}$ is the rate of termination of the chain of n carbon atoms, and $\phi\ i$ is the mole fraction of the products of n carbon atoms. Experimentally, the value of α can be determined from equation 1.4 as expressed in logarithmic form, plotting log (Wn/n) compared to n according to the following equation:

$$\log \frac{W_n}{n} = n \cdot (\log \alpha) + \frac{(1-\alpha)^2}{\alpha} \qquad [1.6]$$

Equation 1.5 implies that the Fischer-Tropsch synthesis is not selective to a single reaction product or a specific range of carbon numbers, methane being the only exception, which can occur with a selectivity of 100 % (α = 0). However, there is the possibility to control, within certain limits, the composition of the products mixture obtained by changing the reaction conditions or the composition of catalysts. Dry [74] reported typical ranges of α on Ru, Co, and Fe of: 0.85-0.95, 0.70-0.80, and 0.50-0.70, respectively. The chain growth probability α decreases with an increase of the reactor temperature or at higher H_2/CO ratios [74, 75, 76, 77, 78]. Table 1.4 shows the influence of some experimental variables on the product distribution in FTS.

Table 1.4. Selectivity control in Fischer-Tropsch synthesis by means of the process conditions modifications [79].

Parameter	Chain length	Chain branching	Olefin select.	Alcohol select.	Carbon deposition	Methane select.
Temperature	↓	↑	*	↓	↑	↑
Pressure	↑	↓	*	↑	*	↓
H_2/CO	↓	↑	↓	↓	↓	↑
Conversion	*	*	↓	↓	↑	↑
Space velocity	*	*	↑	↑	*	↓

Increase with increasing parameter: ↑
Decrease with increasing parameter: ↓
Complex relation: *

1.3.3.2. Deviations from ideal distributions

Significant deviations from the Anderson-Schulz-Flory distribution are reported in literature. The deviations were sometimes assigned to analytical difficulties [80] and non-steady state conditions of the reactor system [81]. However, novel analytical techniques usually rule out these explanations as the major source for the observed deviations. Firstly, the monomer has to be formed *in situ* on the surface of the catalyst from the CO and H_2 molecules. Secondly, the surface reaction rates depend on the size of the chain in the case of C_1-C_4 hydrocarbons. Finally, the reaction products may suffer secondary reactions that affect the overall distribution. Commonly observed deviations from ideal distributions are:

a) A relatively high molar methane content.

Wojciechowski [82] and Sarup [83] modeled the distribution of linear and branched paraffins with the use of termination probabilities. This way, the excess

of methane yield was described with a separate parameter for the increased termination probability of C_1 precursors. The methane termination probability parameter appears to be between 5 to 20 times larger than the termination probability to paraffins [83]. Dry [74] reported that mass transfer limitations will result in an increase of the thermodynamically favoured product, which is methane. The existence of hot spots, due to high reaction heats, may result in a decrease of the chain growth parameter and a higher yield of methane [74, 75].

b) Selectivity towards ethylene and ethane abnormally low and high respectively [84, 85, 86, 87, 88, 89, 90]. Secondary reactions are often reported as the most probable reason for the anomalies of C_2 products: i) incorporation of ethene in growing chains [91, 92], ii) rapid readsorption of ethene [88, 93, 94]. iii) hydrogenolysis of ethene [95], and iv) hydrogenation of ethene to ethane [87, 89, 96].

c) Probability of chain growth dependent on its length, resulting in a higher selectivity than the expected for the heavier hydrocarbons due to the involvement of the secondary reaction. At a carbon number of about 10, the slope of the semi-logarithmic mole fractions of hydrocarbons against carbon number increases. This phenomenon has been observed on iron [75, 97, 98, 99], cobalt [82, 83, 97, 100], and ruthenium catalysts [97, 101, 102]. It is widely considered that the occurrence of secondary reactions (hydrogenation, reinsertion, hydrogenolysis and isomerization) gives the most reasonable explanation for these deviations of the ASF distribution [89, 96, 103, 104, 105].

1.3.3.3. Improving the quality of FT products

Compounds obtained by the Fischer-Tropsch synthesis require a further purification step in order to be commercially attractive and competitive. Sasol and Shell have developed the hydrocarbon synthesis technology via FT on a commercial scale [106, 107, 108]. Particularly, attending to the kind of product desired, two types of processes have been developed:

- Low temperature Fischer-Tropsch (LTFT): high probability of chain growth (α).
- High temperature Fischer-Tropsch (HTFT): low probability of chain growth (α).

The products obtained are different when the operating temperature is varied during FT synthesis reaction and therefore different improvements in the processes are needed.

In the case of LTFT process, mixtures of linear high molecular weight hydrocarbons (waxes) of high purity are produced. It may have diverse applications: pharmaceutical products, cosmetics industry, etc. A fraction of these paraffins obtained can be used in the manufacture of lubricants achieving exceptional viscosity properties and thermal resistance. However, the main application of the wax produced in the Fischer-Tropsch synthesis is the production of synthetic fuels such as gasoline and diesel. The ideal gasoline consists of a mixture of C_5-C_{12} alkanes with a high level of branching, while the ideal diesel is formed by alkanes of C_{13}-C_{18} linear chain [48].

The heavy paraffins (waxes) obtained in the FT synthesis must be converted into others of less length through a hydrocracking process. Linear paraffins have a low octane number and it is a negative factor for the quality of the gasoline, so it

is necessary a series of transformation processes such as: isomerization, catalytic reforming, alkylation and oligomerization. Nevertheless, the linear hydrocarbons obtained in the C_{13}-C_{18} fraction are excellent for using them as diesel fuels because they possess a high cetane number, about 75 (when the minimum required is within the 45-50 range) [108]. These synthetic fuels are considered of high quality because they do not contain aromatic hydrocarbons, nitrogen and/or sulfur compounds. Normally, the processes for the improvement of the products obtained in this LTFT process such as, cracking, isomerization and oligomerization, account for 15 % of the cost of the GTL process [109].

In the HTFT process, the main products are light olefins, which have a great interest as raw material for polymerization processes [106]. An alternative to improve the performance of LTFT process is by fusing the COD route (**C**onversion of **O**lefins to **D**iesel and Gasoline). This process involves synthesizing petrol and diesel by adding together the syngas short-chain unsaturated carbons to form by oligomerization longer chain hydrocarbons in the petrol and diesel boiling range. Thus a final selectivity of 47 % in the gasoline fraction (C_5-C_{12}) is achieved. The economic viability of this process against LTFT and subsequent hydrocracking will depend on the economic impact of large amounts of methane and ethane produced and the cost difference between oligomerization and hydrocracking. Although currently COD process does not apply to any plant GTL, BTL or CTL, it should be taken into account for future developments.

1.3.4. Reactors and operating condition

The Fischer-Tropsch process comprises the following stages: FT reactors, recycle and compression of unconverted synthesis gas, removal of hydrogen and carbon dioxide, reforming of methane produced and separation of the FT products. The most important aspects to consider for development of commercial Fischer-Tropsch reactors are the high reaction heats and the large number of products with varying vapor pressures (gas, liquid, and solid hydrocarbons). The main reactor types which have been proposed and developed after 1950 are [110, 111, 112]:

1. Three-phase fluidized (ebulliating) bed reactors or slurry bubble column reactors with internal cooling tubes (SSPD: Sasol; GasCat: Energy International, AGC-21: Exxon, see Figure 1.7a).
2. Multitubular fixed bed reactor with internal cooling (Arge: Sasol; SMDS: Shell, see Figure 1.7b).
3. Circulating fluidized bed reactor with circulating solids, gas recycle and cooling in the gas/solid recirculation loop (Synthol: Sasol) (Figure 1.7c).
4. Fluidized bed reactors with internal cooling (SAS: Sasol) (Figure 1.7d).

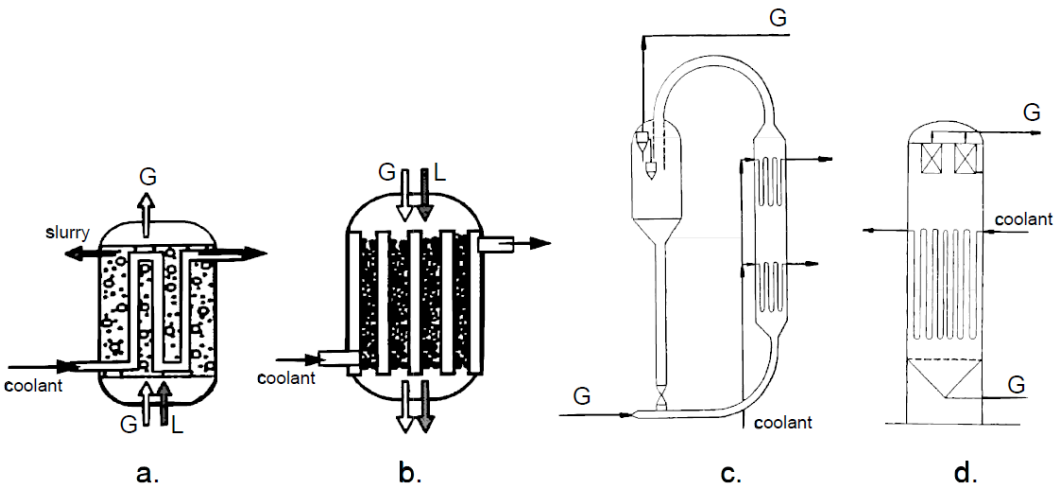

Figure 1.7. Reactors for Fischer-Tropsch synthesis [110, 112], a. Slurry Bubble column reactor; b. Multitubular trickle bed reactor; c. Circulating fluidized bed reactor; d. Fluidized bed reactor.

Typical operation conditions in the Fischer-Tropsch synthesis reaction are between 473 and 633 K and a total pressure between 20 and 60 bar. Usually FT reaction operates in one the following two systems [113]: a low temperature (Low temperature Fischer-Tropsch, LTFT) at temperatures between 473 and 533 K and with Fe and Co based catalysts to form high molecular weight hydrocarbons; and high temperature (high temperature Fischer-Tropsch, HTFT), between 573 and 633 K and with Fe-based catalysts to form short-chain hydrocarbons, meanly. The Fischer-Tropsch Synthesis is a process with a high, exothermic reaction enthalpy (-158 kJ mol^{-1}). For any practical application of this process, when a reasonable reaction rate is desired, the reactor system, including the catalyst inside, should have a function of removing the heat generated by the reaction rapidly. The moving bed reactors are normally used in HTFT processes while multitubular fixed bed reactors and Slurry reactors are used in LTFT processes.

Table 1.5. Advantages (+) and disadvantages (-) of the FTS reactors. Adapted from [113].

Type of reactor	**Fixed bed**	**Bubble column**
Diffusion through the pores	-	+
Mass transfer	+	-
Heat removal	-	+
Change of catalyst	-	+
Attrition of the catalyst	+	-
Cost	-	+

Currently, attempts have been made to improve the performance of these reactors. Among the different options, one that is being investigated is the variation of the geometry of the catalyst. In this line, the honeycomb monoliths (high number of parallel and identical channels with high cell density) have the advantage of having a high surface area and low probability of creating pressure drops. Also, is significantly improved the mass transfer between the gas, liquid and catalyst. However, the recirculation of the liquid is necessary to maintain a high flow rate and thus maintain Taylor regime inside the capillaries.

Other types of technologies are the membrane reactors. These are a technological option still underdeveloped but are attracting great interest in recent years. The membranes can have different functions, such as for example the elimination of water which is a co-product of reaction and which could transform the active sites of the catalysts into inactive species.

1.3.5. Active Metals for Fischer-Tropsch Synthesis Reactions

Active elements in FTS are the elements of groups 8-10 of the periodic table, and of them, only the metals: Fe, Co and Ru have the required FT activity for commercial application [23, 58, 114]. The following is a summary of the major properties of catalysts based on Fe and Co. Since Ru is the active metal studied in this doctoral thesis, it will be discussed in detail in a later section.

1.3.5.1. Iron.

Fe is one of the most studied active metals in the FTS due to its low cost and the wide distribution of formed products which includes paraffins, olefins (linear and branched) and oxygenates compounds, although it is true that this product distribution depends on the whole catalyst composition (use of promoters) and the reaction conditions. Metallic iron exhibits low FT activity; however, under reaction conditions several iron carbide phases, elemental carbon and iron oxides are formed increasing the catalyst activity [115, 116, 117, 118, 119, 120, 121]. It has been concluded that carbide formation is necessary before iron oxide FT catalyst can exhibit any activity [122]. Iron based catalysts are the preferred catalysts for FTS utilizing synthesis gas derived from coal because of their excellent activity in WGSR which allows using a synthesis gas with a low H_2/CO ratio directly without an external shift step [121]. FT iron catalysts need alkali promotion to attain high activity and stability (e.g. K_2O). Addition of SiO_2, Al_2O_3 for structural promotion and maybe some manganese can be applied for selectivity control (e.g. high production of olefins).

With iron catalysts two directions of selectivity have been pursued. One direction at high temperature (HTFT) where low molecular weight olefinic hydrocarbon mixture is produced and the second one at low temperature (LTFT)

in order to form high molecular weight hydrocarbons as it has been described in the previous section.

1.3.5.2. Cobalt.

Co based catalysts are highly active. These catalysts are only used in the LTFT process where they possess high activity and selectivity for heavy waxy product and low WGS reaction activity compared to Fe catalysts. The catalytic behavior of Co for FTS is influenced by many factors such as catalyst preparation method, pretreatment conditions, type of support, Co dispersion, particle size, type of promoters, etc. In general, it is widely accepted that Co metal is the active phase in FTS on Co catalysts. Before reduction, Co is present as Co_3O_4 spinel phase. The reduction process occurs in two stages ($Co_3O_4 \rightarrow CoO \rightarrow Co^0$) until to obtain Co metallic. Typically the cobalt metal loadings vary from 10 to 30 g per 100 g of support. Because of the high price of Co it is desirable to minimize the amount used but to maximize the available surface area of the metal. To achieve this, Co is dispersed on high area stable supports such as Al_2O_3, SiO_2 or TiO_2 [123]. The catalysts are also usually promoted with a small amount of noble metal, e.g. Pt, Ru, Re which is claimed to enhance the reduction process and also keep the Co metal surface "clean" during FT [124]. Metal oxides such as MnO_x, ZrO_2, MgO and CeO_2 improve the activity, selectivity and stability during FT reaction whereas that group 1 alkali metals, including potassium, are a poison for cobalt catalysts [125, 126, 127].

Cobalt based catalysts are not active in the reaction of water gas shift and therefore they are used normally with synthesis gas proceeding from natural gas ($H_2/CO = 2$). Both Co and Fe catalysts are permanently poisoned by sulphur

compounds and thus the sulphur content of the syngas should be kept below about 0.02 mg/m^3 (STP).

1.4. Fischer-Tropsch Synthesis using Ru catalysts.

Among all the metals of group 8 in the periodic table, Ru is the most active metal for the CO hydrogenation reaction. Ruthenium produces high molecular weight hydrocarbons working at high pressure and low temperature [128, 129]. In general, the probability of chain growth (α) obtained with catalysts based on Ru is from 0.85 to 0.95, while the α values obtained with Co and Fe are 0.70-0.80 and 0.50-0.70 respectively [129]. Despite its high price, its study and use at scientific level is fully justified because it produces hydrocarbons even at atmospheric pressure. The high activity of Ru-based catalysts implies a decrease in the FT fuels production costs [130, 131].

As occurs with Fe or Co, product distribution depends strongly on the reaction conditions and catalyst composition. Thus, the chain length depends on the temperature, pressure or nature of the support and this value enhances when the total pressure increases and the reaction temperature decreases.

Ru-based catalysts have the advantage that can operate under conditions of high partial pressure of H_2O. There are studies that confirm that the addition of H_2O into H_2/CO mixture has a positive effect on the catalytic activity and selectivity toward heavy hydrocarbons, since it acts as a source of hydrogen to form reaction intermediates [132]. Besides, Ru can operate in the presence of other atmospheres of oxygenated compounds, which is vital when working with synthesis gas proceeding from biomass [133]. As Co, Ru is not active in the

reaction of water gas shift, therefore it is used normally with synthesis gas proceeding from natural gas whose H_2/CO ratio is equal to 2 [133].

The Ru catalysts are deactivated during the FTS reaction due principally to deposition of carbonaceous species on the surface of the catalysts. The oxidation of the active phase and/or agglomeration of the particles of ruthenium during the reaction condition do not appear to play an important role in the mechanism of deactivation for these catalysts [134]. As with the Fe and Co-based catalysts, the catalytic performance of the Ru catalysts is modified with the addition of different elements which improves the catalytic activity, the selectivity and thermal stability. In this thesis, cesium and molybdenum will be studied as promoters of ruthenium catalysts. It will be explained in more detail in the next sections. Table 1.6 compares the performance and properties of Fe, Co and Ru catalysts.

Table 1.6 Comparison of the performance and properties of the Fe, Co, and Ru catalysts.

Property	**Fe**	**Co**	**Ru**
FT activity	Active	Active	Active
Selectivity	Light hydrocarbons	Heavy hydrocarbons	Heavy hydrocarbons
Syngas	Coal, biomass, natural gas	Natural gas	Natural gas
WGS activity	Active	Inactive	Inactive
Poison	H_2S	H_2S	H_2S
Reaction temperature	573-633 K	473-533 K	473-533 K
Cost*	4.46×10^{-3} \$/g	0.2 \$/g	1.41 \$/g

* Obtained from reference [135]

As already it was mentioned, Ru is the most active metal and which has a higher selectivity to heavy hydrocarbons (higher α), thus explaining the scientific

interest of this metal. In addition, Ru catalysts are suitable for fundamental research to gain insights into the catalyst functioning and/or reaction mechanisms [23, 136, 137,138]. A quick search on Scopus reflects the growing interest in the study of this metal in the Fischer-Tropsch reaction. The figure 1.8 also reflects the large number of existing published studies of Fe and Co versus Ru in the last decade. It shows that Ru is the least studied of the three active metals in FTS.

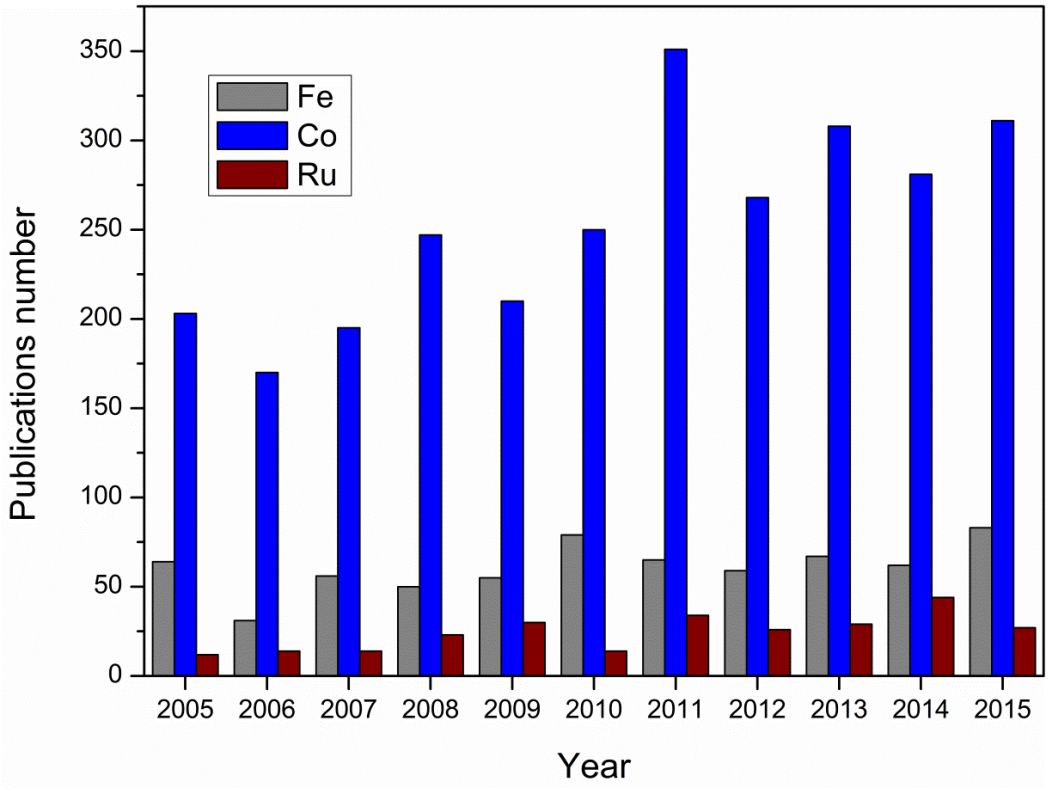

Figure 1.8. Publications number of Fe, Co and Ru in FTS in the last decade (January 2016).

The major drawback of this metal for industrial application is its high cost and its limited availability. Therefore it is necessary to maximize its efficiency in terms of activity and hydrocarbons production with the goal of making this route more competitive industrially with regard to Fe or Co processes. In fact, if it is attempted to use biomass as feedstock syngas in order to mitigate emissions of

CO_2 and taking into account that it is a raw material delocalized around the world, it may be necessary a local and efficient use of same smaller dimension plants. This fact will depend largely on the use of highly active catalysts in the Fischer-Tropsch synthesis in order to have the best possible performance in the process [38, 139]. In this sense, it is necessary to obtain catalysts based on Ru, very active in the Fischer-Tropsch synthesis and with high selectivity to diesel fraction (C_{13}-C_{18}, α~0.85). In this context, it has been chosen to maximize the selectivity to diesel fraction by a suitable support election in terms of physico-chemical properties, the determination of the optimum Ru particle size for which the activity is maximum and the use of Cs or Mo as promoter. In the following chapters of this doctoral thesis it will be reviewed more extensively the works that have been performed following this line. The next section briefly discusses the importance of the support in the preparation of catalysts.

1.5. Influence of the support in the Fischer-Tropsch synthesis.

Most catalysts used in heterogeneous catalysis consist of one or more active components deposited on a high surface area support whose main objective is to obtain an optimum dispersion and stabilization of the active components againsts agglomeration. However, in some reactions the support is not inert and has a significant effect on the reducibility, activity and selectivity of the active phase and promoters [140, 141, 142, 143]. Selection of a support with a proper interaction with the active phase (or metal precursor) is of prime importance because of the balance between the reducibility and the dispersion of the active phase that defines FTS performance. Supports such as alumina [144, 145], silica[146, 147], titania [148], and carbon materials [133, 149, 150, 151, 152, 153]

have been reported by many groups. Among them, carbon materials are considered to be more inert than the conventional oxide materials. The inertness of the carbon surface facilitates the reduction of the metal precursor to the zero valence state and favors the interaction metal-promoter instead of the metal-support one [138, 152]. Furthermore, carbon materials usually have high surface area and good stability at high temperatures in inert or reducing atmospheres. This allows the study of the intrinsic properties of the ruthenium particles, in contrast to oxidic supports where poorly reducible mixed oxides may interfere during catalyst synthesis or FT catalysis. Tauster [154, 155] was one of the first researchers to use the term strong-metal-support interaction (SMSI) to explain the lower adsorption capacity of CO and H_2 molecules of noble metals when are deposited on materials such as TiO_2.

Among the carbon materials the high surface area graphite, in particular, possesses high external surface area without micropores which precludes mass transfer problems during the reaction [153]. In Figure 1.9 the typical structure of graphite it is shown.

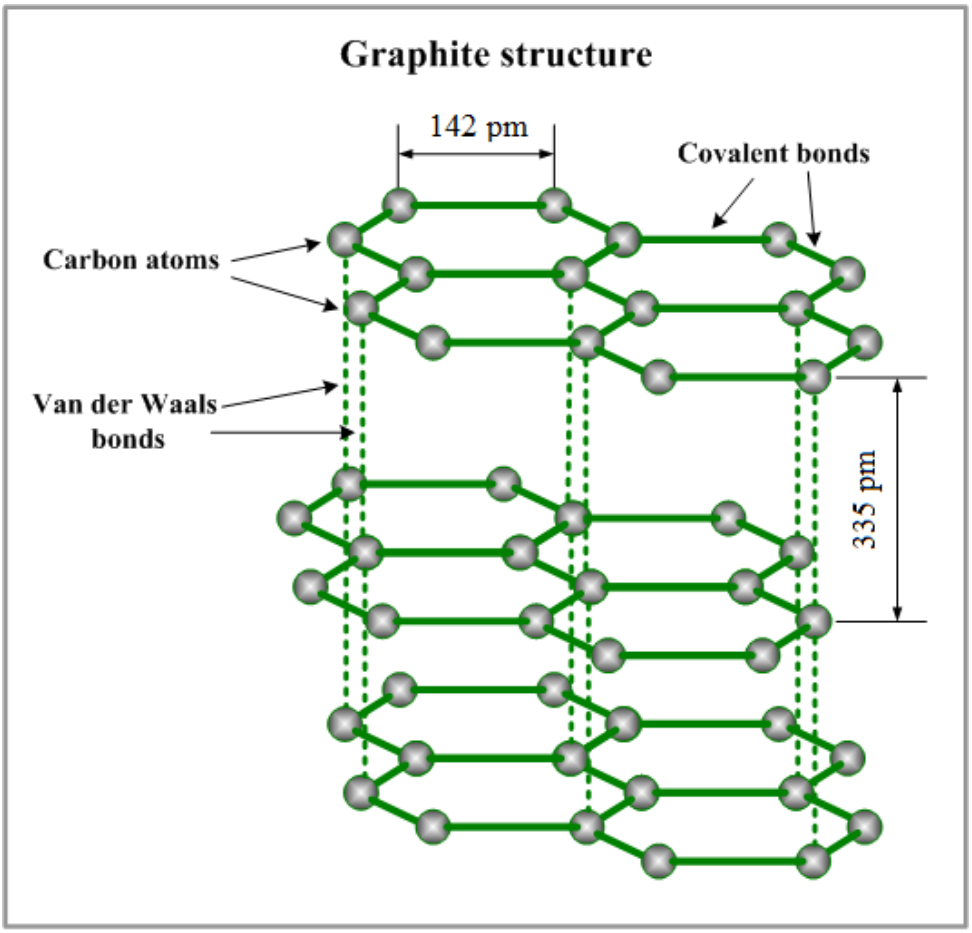

Figure 1.9. Side view of the graphite structure.

Atoms in the plane are bonded covalently, with only three of the four potential bonding sites satisfied. The fourth electron is free to migrate in the plane, making graphite electrically conductive which is very interesting from the catalytic point of view. However, it does not conduct in a direction perpendicular to the plane. Bonding between layers is via weak Van der Waals bonds, which allows layers of graphite to be easily separated, or to slide past each other. Another very important factor that can affect to the catalytic ability of the carbon materials is the presence of surface oxygen groups which may be modified by various chemical or thermal treatments.

In this doctoral thesis it has been used two different high surface area graphites from TIMCAL as catalyst supports in order to modify the Ru dispersion and to study the effect of Ru particle size on catalytic performance in FT synthesis. It will be discussed in detail in a later section.

1.6. Ru particle size effect in Fischer-Tropsch synthesis.

Fischer-Tropsch synthesis is recognized as a structure sensitive reaction, which means that the surface-specific activity (turnover frequency, TOF) is a function of the metal particle size [133, 150, 156, 157]. The effect of metal particle size on the catalytic performance has been extensively studied by several authors for cobalt [158, 159, 160], with earliest contributions from Bartholomew [161] and Yermakov [162], and for iron [163, 164, 165]. However, in the case of ruthenium, the number of research studies is limited. During the 80s, a few studies pointed out the increase in TOF for CO hydrogenation with increasing the size of Ru supported on alumina (or decreasing the metal dispersion from 0.78 to 0.16) [166, 167]. It was also shown that the TOFs over Ru catalysts loaded on metal oxides such as SiO_2, Al_2O_3 and TiO_2 were independent of the dispersion of Ru in the range studied (0.0009−0.60) [168]. Recently, Kang *et al*. [161, 169] studied the size-effects for FT synthesis catalyzed by Ru nanoparticles loaded on carbon nanotubes. They reported that the TOF increased significantly with the mean size of Ru up to approximately 6 nm and then decreased only slightly with further size increases. The C≥5 selectivity also underwent a gradual increase with increasing the mean Ru particle size from 2.3 to 6.3 nm. Carballo *et al*. [170] investigated the size effect of Ru particles supported on γ-Al_2O_3 and found that the FT synthesis with Ru/γ-Al_2O_3 catalysts is a strongly structure-sensitive reaction when the size

of Ru particles was smaller than 10 nm. Theoretical understanding of the origin of the effect of metal particle size on reaction rates of a given reaction has been tackled by Van Santen *et al*. [50, 156,]. They stated that the CO activation in the FT reaction needs a reaction center with a particular configuration of several metal atoms and step-edge sites, which geometrically may not be present below a particle size of 2 nm.

As the support material may mask the metal particle size effects, research focused on intrinsic ruthenium particle size effects may be advantageously performed using an inert support material, such as graphitic carbon. To clarify the effect of Ru particle size on catalytic performance in FT synthesis, we have prepared Ru catalysts supported on high surface area graphite (HSAG) varying the size of Ru particles from 1.7 to 12 nm by using two HSAGs with different surface area (100 and 400 m^2/g) and various Ru loadings. These results are shown in chapter 5.

1.7. Cs promotion effect in Fischer-Tropsch synthesis.

It is known that FT catalysts usually require promoters such as alkali metals, noble metals or transition metal oxides to attain the optimal catalytic performance [23]. Modification with alkali metal ions increases both the activity and selectivity for high molecular weight hydrocarbons and favors the formation of olefins [163, 171]. This behavior could be explained by the basicity of the alkali promoter, which is proposed to raise the CO dissociative adsorption rate, increasing the surface coverage of dissociated CO and lowering the hydrogen coverage. In this sense, the alkali promoter shifts the hydrocarbon selectivity towards longer chain hydrocarbons and olefin products [172]. Furthermore, it has been reported that such alkali elements (Na, K or Cs) are electronic promoters that transfer part of

their electron density to Ru even in its oxidized state, which strengthens the CO-metal interaction whereas weakening the C-O bond [173, 174, 175, 177]. This is schematically shown in the figure 1.10. Recently, some experimental evidences of the partial reduction of Cs in Cs-Ru/C catalysts during temperature-programmed reduction have been provided by X-ray absorption spectroscopy [151].

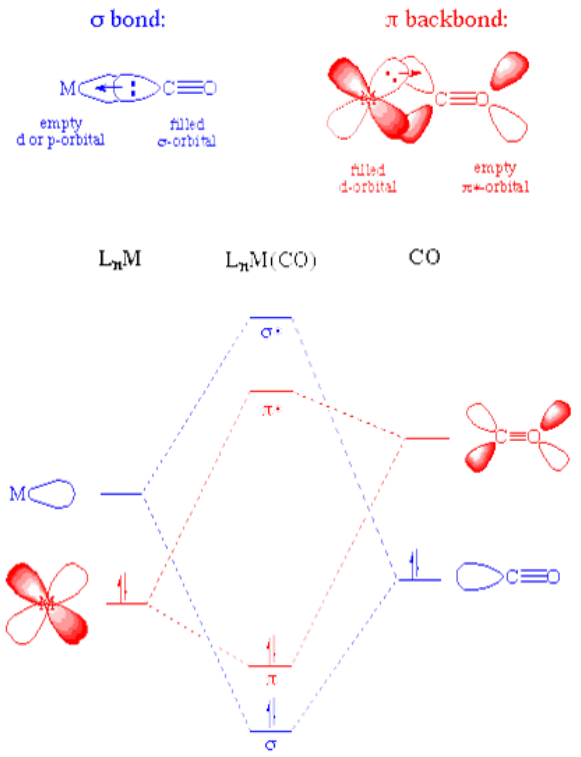

Figure 1.10. Scheme of π-backbond between CO-metal.

On the other hand, the selection of the metal and promoter precursors is also an important issue. It might affect the intrinsic reactivity of the active centers located on the catalyst surface during Fischer-Tropsch synthesis [176, 177, 178]. The type of metal precursor employed in the impregnation of the support has a significant effect on the metal-support interactions, reduction properties and dispersion. Besides, residual species (such as Cl^-) might remain anchored on the

metal after the pretreatment step [153] blocking or modifying some adsorption active sites on the catalyst. In this thesis we have studied the effect of different ruthenium and cesium precursors on a high surface area graphite support in the Fischer-Tropsch synthesis. It was also performed an extensive characterization work in an attempt to gain further insights into the system.

1.8. Mo promotion effect in Fischer-Tropsch synthesis.

One of the principal requirements for FTS processes to be economically viable is to achieve a high activity and selectivity toward C_{5+} hydrocarbons together with a low selectivity to byproducts such as methane. In order to accomplish this purpose as well as increasing the olefin content, transition metal oxides might be expected to have inherently interesting properties since early metals tend to be quite oxophilic forming strong bonds with oxygen. In contrast the latter metals bind weaker to oxygen and are easily reduced [179]. Used in combination, these differences in the metal-oxygen bond strengths determine the metal catalytic properties when in contact with oxide support surfaces. Preparation methods of catalysts should be designed which lead to interaction of the two metals with each other, rather than separately with the support. Alternatively an inert support such as a graphitic material can be used to foster the metal-promoter interaction [180]. Several explanations for the manner by which oxide promoters affect the FTS performance of metal catalysts have been introduced by numerous authors. Burch and Flambard [181] have suggested that the active sites in the oxide promoted catalysts are located at the metal/metal oxide interface. Sachtler, Ichikawa and coworkers [182, 183] extended this proposal by suggesting that a Lewis acid/base bonding interaction occurs between the oxygen end of the adsorbed CO and the oxide promoter at the oxide/metal

interface. Miyamoto et al [184] studied the hydrogenation of CO over Ru/Al_2O_3 catalysts using different oxides promoter such as V, Nb, Mo, W, and Re. They observed that these promoters markedly increased the rate constant for the dissociation of CO to form $(CH_x)_{ad}$ (k_{CO}) on the catalyst surface, whereas the rate constant for the hydrogenation of CO to form CH_4 (k_{CH4}) decreased. Higher concentrations of $(CH_x)_{ad}$ are favorable for the production of higher hydrocarbons, because they are considered to be formed through the polymerization of CH_x, followed by the hydrogenation of the resultant surface species [53].

A promoter of particular interest for FTS catalysts is Mo. It has been reported by several authors [179, 185, 186, 187, 188, 189, 190, 191, 192, 193] that Mo promotion increases catalyst activity, decreases C_1 formation, increases the olefin to paraffin (O/P) ratio of the C_2-C_4 fraction, and enhances the formation of C_{5+}. It has been shown that the addition of MoO_3 and alkali metal, i.e., K or Na, to Ru/Al_2O_3 [188, 194] and Ru/SiO_2 [193] greatly favors the alcohol production from CO and H_2. Nevertheless, there are relative few studies where an inert support is used to favor the metal-promoter interaction instead of the metal-support one. Here, we present a comprehensive study aimed at investigating the influence of Mo promotion on the activity and selectivity of Ru supported on a high surface area graphite (G). The key in producing an effective promoted metal catalyst lies in the intimate promoter-metal interaction, as catalyst promotion is a local effect. Carbon materials are considered to be more inert than the convectional oxide materials [138,152]. The inertness of the carbon surface facilitates the reduction of the metal precursor to the zero valence state and favors the interaction metal-promoter. FT experiments were conducted at 3.5 bar and CO conversions below 15% (in order to ensure differential conditions limiting the extent of secondary

reactions) using G-supported Ru both unpromoted and promoted with varying Mo loadings. The yield and selectivity for C_{5+} formation were considerably increased with the presence of Mo promoter. To interpret the scientific bases of these feature, the different catalysts were characterized by temperature programmed reduction (TPR), transmission electron microscopy (TEM) and microcalorimetry of CO chemisorption. See chapter 7 for more details.

1.9. References

[1] BP Energy Outlook 2030, www.bp.com, (2010).

[2] Framework Convention on Climate Change (United Nations, 1997), http://unfccc.int/kyoto_protocol/items/2830.php.

[3] Annual Energy Outlook 2015, Energy Administration Information USA, http://www.eia.gov/forecasts/aeo/pdf/0383(2015).pdf

[4] BP Statistical Review of World Energy 2015. www.bp.com.

[5] G. Liu, E.D. Larson, R.H. Williams, T.G. Kreutz, X. Guo, *Energ. Fuel*, 25 (2011) 415-437.

[6] T. H. Fleisch, R. A. Sills, M. D. Briscoe, J. Nat. *Gas Chem*. 11 (2002) 1-14.

[7] A. P. Steynberg, H.G. Nel, *Fuel*, 83 (2004) 765-770.

[8] C. Marcilly, *J. Catal*. 216 (2003) 47-62.

[9] D. Vallentin, *Energ. Policy*, 36 (2008) 2030-2043.

[10] D. J. Wilhelm, D. R. Simbeck, A. D. Karp, R. L. Dickenson, *Fuel Process. Technol*. 71(1-3) (2001) 139-148.

[11] H. Boerrigter, H. den Uil, *Proceedings of the 12th European Biomass Conference 1152*. ETA-Florence and WIP-Munich: (2002).

[12] A. K. Prabhu, R. Radhakrishnan, S. T. Oyama, *Appl. Catal. A: Gen*. 183 (1999) 241-252.

[13] Rostrup-Nielsen, J. *Appl. Catal. A: Gen*. 255(1) (2003) 3.

[14] J. H. Edwards, *Catal. Today*, 23 (1995) 59-66.

[15] M. A. Peña, J. P. Gómez, J. L. G. Fierro, *Appl. Catal. A: Gen*. 144(1-2) (1996) 7-57.

[16] M. A. Peña, J. L. G. Fierro, Supported metals in the production of hydrogen. In *Supported metals in catalysis;* M. Fernández-García, J. A. Anderson, Eds.; Chapter 7. Imperial College Press: (2005).

[17] H. Pichler, in: W. G. Frankenburg, V. I. Komarewsky, E. K. Rideal (Eds.), *Adv. Catal*. 4 (1952) 271-341.

[18] K. Klier, *Adv. Catal*. 31 (1982) 243-313.

[19] A. C. Vosloo, *Fuel Proc. Tech.* 71(1-3) (2001) 149-155.

[20] A historical account on Fischer-Tropsch synthesis can be found on the web: http://www.fischer-tropsch.org.

[21] M. E. Dry. *Catal. Today*, 71 (2002) 227–241.

[22] F. Fischer, H. Tropsch, *Brennstoff-Chem*. (1926) 97.

[23] H. Schulz, *Appl. Catal. A: Gen*. 186 (1999) 3-12.

[24] R. B. Anderson, in: P. H. Emmett (Ed.), Catalysis, Vol. IV, Reinhold, New York, 1956.; R.B. Anderson, The Fischer-Tropsch Synthesis, Academic Press, New York, (1984).

[25] Exxon Mobil press release on July 14 2004 (http://www.exxonmobil.com).

[26] Shell press release on March 9 2004 (http://www.shell.com).

[27] G. P. van der Laan, Kinetics, selectivity and scale up of the Fischer-tropsch synthesis. PhD Thesis, Groningen University (1999).

[28] *Foc. Catal*. 10 (2005) 3.

[29] Thackeray, F. Fischer-Tropsch GTL Approaches Threshold. In *World Petroleum Congress* (2003) pp. 150-154.

[30] J. Jacometti, A. Ekvall, Shell in the Middle East, issue 17, April (2002), 1-3.

[31] G. Coupe, Step on the gas, in *The Engineer*, August 6 (2004).

[32] F. Thackeray, Fischer-Tropsch GTL Approaches Treshold, in *World Petroleum Congress*, (2003) pp. 150-151.

[33] A. H. Tullo, Catalyzing GTL, in *Chem. Eng. News*, 81 (2003) 18.

[34] G. P. van Der Laan, A. A. C. M. Beenackers, Catal. *Rev. Sci. Eng*. 41 (1999) 255-318.

[35] A. A. Adesina, *Appl. Catal. A: Gen*. 138 (1996) 345.

[36] M. E. Dry. *Appl. Catal. A: Gen*. 138 (1996) 319-344.

[37] J.P. Hindermann, G.J. Hutchings, A. Kiennemann, *Catal. Rev. Sci. Eng*. 35 (1993) 1-127.

[38] E. van Steen, M. Claeys, *Chem. Eng. Technol*. 31 (2008) 655-666.

[39] F. Fischer, H. Tropsch, *Brennstoff-Chem*. 4 (1923) 276-285.

[40] D. Bianchi, L. M. Tau, S. Borcar, C.O. Bennett, *J. Catal*. 84 (1983) 358-374.

[41] P. Biloen, J. N. Helle, W. M. H. Sachtler, *J. Catal*. 58 (1979) 95-107.

[42] P. Biloen, J. N. Helle, F. G. A. van den Berg, W. M. H. Sachtler, *J. Catal*. 81 (1983) 450-463.

[43] Y. Kobori, H. Yamasaki, S. Naito, T. Onishi, K. Tamaru, *J. Chem. Soc*. 78 (1982) 1473-1490.

[44] E. Iglesia, *Appl. Catal. A: Gen*. 161 (1997) 59-78.

[45] R. B. Anderson, P.H. Emmet, *Acad. Press. Inc*. (1956).

[46] H. Pichler, H. Schulz, *Chem. Ing. Tech*. 42 (1970) 1162-1174.

[47] M. G. Nicole Franssen, J. C. Annemarie Walters, N. H. Joost Reek, Bas de Bruin. *Catal. Sci. Technol*. 1 (2011) 153-165.

[48] M. E. Dry, *J. Chem. Technol. Biot*. 77 (2002) 43-50.

[49] P. Biloen, W. M. H. Sachtler, *Adv. Catal*. 30 (1981) 165-216.

[50] S. Shetty, R. A. van Santen, *Catal. Today*, 171 (2011) 168-173.

[51] I. M. Ciobîca, R. A. van Santen, *J. Phys. Chem. B*, 107 (2003) 3808-3812.

[52] S. Shetty, A. P. J. Jansen, R. A. van Santen, *J. A. C. S.* 131 (2009) 12874-12875.

[53] R. A. van Santen, I. M. Ciobîca, E. van Steen, M. M. Ghouri, *Adv. Catal*. 54 (2011) 127-187.

[54] W. J. Mitchell, J. Xie, T. A. Jachimowski, W. H. Weinberg, *J. A. C. S*. 117 (1995) 2606-2617.

[55] O. R. Inderwildi, S. J. Jenkins, D. A. King, *J. Phys. Chem. C*, 112 (2008) 1305-1307.

[56] E. Shincho, C. Egawa, S. Naito, K. Tamaru, *Surf. Sci*. 149 (1985) 1-16.

[57] R. A. van Santen, M. M. Ghouri, S. Shetty, E. M. H. Hensen, *Catal. Sci. Technol*. 1 (2011) 891-911.

[58] G. P. van der Laan, A. A. C. M. Beenackers, *Catal. Rev. Sci. Eng*. 41 (1999) 255-318.

[59] H. Schulz, K. Beck, E. Erich, *Fuel. Process. Technol*. 18 (1988) 293-304.

[60] D. Newsome, *Catal. Rev. Sci. Eng*. 21 (1980) 275-318.

[61] A. A. Adesina, *Appl. Catal. A: Gen*. 138 (1996) 345-367.

[62] E. S. Lox, G.F. Froment, *Ind. Eng. Chem. Res*. 32 (1993) 71-82.

[63] D. G. Rethwisch, J.A. Dumesic, *J. Catal*. 101 (1986) 35-42.

[64] C. K. Rofer-DePoorter, *Chem. Rev*. 81 (1981) 447-474.

[65] B. H. Davis, *Fuel Process. Technol*. 71 (2001) 157.

[66] A.Y. Khodakov, W. Chu, P. Fongarland, *Chem. Rev*. 107 (2007) 1692.

[67] E. I. Mabaso, PhD. Thesis, University of Cape Town, Rondebosch, Cape Town (2005).

[68] M. Claeys, E. Van Steen, A. Steynberg, M. Dry, Eds. Elsevier (2004) pp. 601.

[69] E. F. G. Herrington, *Chem. Indust*, 65 (1946) 346.

[70] R. A. Friedel, R. B. Anderson, *J. A. C. S*. 72 (1950) 1212.

[71] G. V. Z. Schulz, *Phys. Chem*. B30 (1935) 379.

[72] P. Flory, *J. A. C. S*. 58 (1936) 1877.

[73] M. E. Dry, *Catal. Today*, 6 (1990) 183-206.

[74] M. E. Dry, *J. Mol. Catal.* 1982, 17, 133.

[75] R. A. Dictor, A. T. Bell, *J. Catal*. 97 (1986) 121-136.

[76] E. S. Lox, G. F. Froment, *Ind. Eng. Chem. Res.* 32 (1993) 61-70.

[77] T. J. Donnelly, C. N. Satterfield, *Appl. Catal. A*, 52 (1989) 93-114.

[78] R. C. Everson, E. T. Woodburn, A. R. M. Kirk, *J. Catal*. 53 (1978) 186-197.

[79] M. Röper, Fischer-Tropsch synthesis, in W. Keim, Eds. *Catalysis in C*1 *chemistry*, D. Reidel, Dordrecht, The Netherlands (1983) pp. 41-88.

[80] I. Puskas, R. S. Hurlbut, R. E. Pauls, *J. Catal*. 139 (1993) 591–601.

[81] Jr. G. A Huff, C. N. Satterfield, *Ind. Eng. Chem. Process Des. Dev.* 24 (1985) 986-995.

[82] B. W. Wojciechowski, *Catal. Rev. Sci. Eng.* 30 (1988) 629-702.

[83] B. Sarup, B. W. Wojciechowski, *Can. J. Chem. Eng.* 66 (1988) 831-842.

[84] S. Novak, R. J. Madon, H. Suhl, *J. Catal*. 77 (1982) 141-151.

[85] S. Novak, R. J. Madon, H. Suhl, *J. Chem. Phys*. 74 (1981) 6083-6091.

[86] E. W. Kuipers, I. H. Vinkenburg, H. Oosterbeek, *J. Catal*. 152 (1995) 137-146.

[87] E. W. Kuipers, C. Scheper, J. H. Wilson, I. H. Vinkenburg, H. Oosterbeek, *J. Catal*. 158 (1996) 288-300.

[88] T. Komaya, A. T. Bell, *J. Catal*. 146 (1994) 237-248.

[89] D. S. Jordan, A. T. Bell, *J. Phys. Chem*. 90 (1986) 4797-4805.

[90] E. Iglesia, S. C. Reyes, R. J. Madon, *J. Catal*. 129 (1991) 238-256.

[91] S. Novak, R. J. Madon, H. Suhl, *J. Chem. Phys.* 74 (1981) 6083-6091.

[92] S. Novak, R. J. Madon, H. Suhl, *J. Catal.* 77 (1982) 141-151.

[93] E. Iglesia, S. C. Reyes, R. J. Madon, S. L. Soled, *Adv. Catal.* 39 (1993) 221-302.

[94] H. Schulz, E. van Steen, M. Claeys, DGMK, Kassel, Germany (1993).

[95] H. Schulz, K. Beck, E. Erich, *Stud. Surf. Sci. Catal*. 36 (1988) 457-471.

[96] E. W. Kuipers, I. H. Vinkenburg, H. Oosterbeek, *J. Catal*. 152 (1995) 137-146.

[97] R. J. Madon, E. Iglesia, S. C. Reyes, *ACS Symposium Series*, 517 (1993) 383-396.

[98] Jr. G. A. Huff, C. N. Satterfield, *Ind. Eng. Chem. Process Des. Dev.* 23 (1984) 696-705.

[99] N. O. Egiebor, W. C. Cooper, B. W. Wojciechowski, *Can. J. Chem. Eng.* 63 (1985) 826-834.

[100] I. C. Yates, C. N. Satterfield, *Energ. Fuel*, 6 (1992) 308-314.

[101] M. Inoue, T. Miyake, T. Inui, *J. Catal*. 105 (1987) 266.

[102] E. Iglesia, H. Vroman, S. L. Soled, J. E. Baumgartner, R. A. Fiato, *US Patent* 5,036,032 (1991).

[103] R. J. Madon, E. Iglesia, *J. Catal*. 139 (1993) 576-590.

[104] H. Schulz, K. Beck, E. Erich, D. M. Bibby, C. D. Chang, R. F. Howe, S. Yurchak, Eds, *Methane Conversion*, Elsevier Science (1988).

[105] C. L. Bianchi, V. Ragaini, *J. Catal.* 168 (1997) 70-74.

[106] A. P. Steynberg, R. L. Espinoza, B. Jager, A. C. Vosloo, *Appl. Catal. A: Gen.* 186(1-2) (1999) 41-54.

[107] R. L. Espinoza, A. P. Steynberg, B. Jager, A. C. Vosloo, *Appl. Catal. A: Gen.* 186(1-2) (1999) 13-26.

[108] M. E. Dry, *Appl. Catal. A: Gen.* 276(1-2) (2004) 1-3.

[109] E. F. Sousa-Aguiar, L. G. Appel, C. Mota, *Catal. Today*, 101 (2005) 3-7.

[110] S.T. Sie, *Rev. Chem. Eng*. 14 (1998) 109-157.

[111] B. Jager, *Stud. Surf. Sci. Catal*. 107 (1997) 219-224.

[112] B. Jager, M. E. Dry, T. Shingles, A. P. Steynberg, *Catal. Lett*. 7 (1990) 293-302.

[113] R. Guettel, U. Kunz, T. Turek, *Chem. Eng. Technol*. 31 (2008) 746-754.

[114] M. Gharibi, F. T. Zangeneh, F. Yaripour, S. Sahebdelfar, *Appl. Catal. A: Gen*. 443-444 (2012) 8-26.

[115] H. H. Storch, N. Golumbic, R. B. Anderson, *The Fischer-Tropsch and Related Syntheses*, Wiley, New York (1951).

[116] C. D. Frohning, H. Kölbel, M. Ralek, W. Rottig, F. Schnur, H. Schulz, in: J. Falbe (Ed.), Chemierohstoffe aus Kohle, Georg Thieme Verlag, Stuttgart (1977) pp. 219.

[117] H. Schulz, G. Schaub, M. Claeys, T. Riedel, *Appl. Catal. A*, 1999, 186, 215.

[118] J. W. Niemantsverdriet, A. M. van der Kraan, W. L. van Dijk, H. S. van der Baan, *J. Phys. Chem*. 54 (1980) 3363.

[119] C. N. Satterfield, R. T. Hanlon, S. E. Tung, Z. Zou, G. C. Papaefthymiou, *Ind. Eng. Chem. Prod. Res. Dev*. 25 (1986) 401.

[120] O. G. Malan, J. D. Louw, L. C. Ferreira, *Brennstoff-Chem*. 1961, 42, 209.

[121] M. E. Dry; J.R. Anderson, M. Boudart, Eds, *Catal. Sci. Technol*, M. Springer, Berlin (1981) pp. 159-256.

[122] R. Zhao, J. G. Goodwin Jr., K. Jothimurugesan, S. K. Gangwal, J. J. Spivey, *Ind. Eng. Chem. Res*. 40 (2001) 1320-1328.

[123] R. Oukaci, A. H. Singleton, J. G. Goodwin, *Appl. Catal. A: Gen*. 186 (1999) 129.

[124] E. Iglesia, S.L. Soled, R.A. Fiato, G. H. Via, *J. Catal*. 143 (1993) 345.

[125] A.Y. Khodakov, W. Chu, P. Fongarland. *Chem. Rev*. 107 (2007) 1692-1744.

[126] F. Morales, E. de Smit, F. M. F. de Groot, T. Visser, B. M. Weckhuysen, *J. Catal*. 246 (2007) 91-99.

[127] S. Sun, K. Fujimoto, Y. Yoneyama, N. Tsubaki. *Fuel*, 81 (2002) 1583-1591.

[128] M. A. Vannice, *J. Catal*. 37 (1975) 449-461.

[129] J. P. Hindermann, G. J. Hutchings,A. Kiennemann, *Catal. Rev. Sci. Eng*. 35 (1993) 1-127.

[130] M. J. A. Tijmensen, A.P.C. Faaij, C. N. Hamelinck, M. R. M. van Hardeveld. *Biomass Bioenerg*. 23 (2002) 129-152.

[131] C. N. Hamelink, A. P. C. Faaij, H. den Uil, *Energy*, 29 (2004) 1743-1771.

[132] M. Claeys, E. van Steen, *Catal. Today*. 71 (2002) 419-427.

[133] J. Kang, S. Zhang, Q. Zhang, Y. Wang. *Angew. Chem-Int. Edit*. 48 (2009) 2565-2568.

[134] K. R. Krishna, A. T. Bell, *J. Catal*. 130 (1991) 597-610.

[135] http://www.infomine.com/investment/metal-prices/.

[136] M. E. Dry, G. Ertl, H. Knözinger, F. Schüth, J. Weitkamp, Eds, Wiley-VCH, Weinheim, 6 (2008) 2965-2994.

[137] D. A. Simonetti, J. Rass-Hansen, E. L. Kunkes, R. R. Soares, J. A. Dumesic, *Green Chem.* 9 (2007) 1073-1083.

[138] Q. Zhang, J. Kang, Y. Wang, *ChemCatChem*. 2 (2010) 1030-1058.

[139] K. Okabe, K. Murata, M. Nakanishi, T. Ogi, M. Nurunnabi, Y. Liu. *Catal. Lett*. 128 (2009) 171-176.

[140] M. Che, O. Clause, C. Marcilly, G. Ertl, H. Knözinger, J. Weitkamp, Eds, *Preparation of solid catalysts*, Wiley-VCH, pp. 315-540.

[141] A.Y. Khodakov, *Catal. Today*, 144 (2009) 251-257.

[142] S. L. Soled, E. Iglesia, R. A. Fiato, J. E. Baumgartner, H. Vroman, S. Miseo, *Top. Catal.* 26 (2003) 101-109.

[143] S. Storsæter, B. Tøtdal, J. C. Walmsley, B. S. Tanem, A. Holmen, *J. Catal.* 236 (2005) 139-152.

[144] J. L. Zhang, J. G. Chen, J. Ren, Y. W. Li, Y. H. Sun, *Fuel*, 82 (2003) 581.

[145] H. F. Xiong, Y. H. Zhang, S. G. Wang, J. L. Li, *Catal. Commun*. 6 (2005) 512.

[146] D. C. Song, J. L. Li, J. *Mol. Catal. A*, 247 (2006) 206.

[147] H. F. Xiong, Y. H. Zhang, K. Y. Liew, J. L. Li, *J. Mol. Catal. A*, 295 (2008) 68-76.

[148] J. L. Li, G. Jacobs, Y. Q. Zhang, T. Das, B. H. Davis, *Appl. Catal. A*, 223 (2002) 195.

[149] J. L. Eslava, A. Iglesias-Juez, G. Agostini, M. Fernández-García, A. Guerrero-Ruiz, I. Rodríguez-Ramos, *ACS Catal*. 6 (2016) 1437.

[150] G. L. Bezemer, J. H. Bitter, P. C. E. Kuipers, H. Oosterbeek, J. E. Holewijn, X. Xu, F. Kapteijn, A. J. van Dillen, K. P. de Jong, *J. Am. Chem. Soc*. 128 (2006) 3956.

[151] W. P. Ma, Y. J. Ding, L. W. Lin, *Ind. Eng. Chem*. Res. 43 (2004) 2391.

[152] K. Xiong, J. L. Li, K. Y. Liew, X. D. Zhan, *Appl. Catal. A*. 389 (2010) 173-178.

[153] L. Gonzalo-Chacón, M. Almohalla, E. Gallegos-Suarez, A. Guerrero-Ruiz, I. Rodríguez-Ramos, *Appl. Catal. A*. 480 (2014) 86.

[154] S. J. Tauster. *Accounts Chem. Res*. 20 (1987) 389-394.

[155] S. J. Tauster, S. C. Fung, R. L. Garten, *J. A. C. S*. 100 (1978) 170-175.

[156] R. A. van Santen, *Acc. Chem. Res*. 42 (2009) 57.

[157] D. Barkhuizen, E.I. Mabaso, E. Viljoen, C. Welker, M. Claeys, E. van Steen, J.C.Q. Fletcher. *Pure Appl. Chem*. 78 (2006) 1759.

[158] G. Prieto, A. Martínez, P. Concepción, R. Moreno-Tost, *J. Catal*. 266 (2009) 129.

[159] J. P. den Breejen, P. B. Radstake, G. L. Bezemer, J. H. Bitter, V. Frøseth, A. Holmen, K. P. de Jong. *J. A. C. S*. 131 (2009) 7197.

[160] A. Barbier, A. Tuel, I. Arcon, A. Kodre, G. A. Martin, *J. Catal*. 200 (2001) 106.

[161] R. C. Reuel, C. H. Bartholomew, *J. Catal*. 85 (1984) 78.

[162] A. S. Lisitsyn, A. V. Golovin, V. L. Kuzketsov, Y. I. Yermakov. *J. Catal*. 95 (1985) 527.

[163] T. E. Hoost, J. G. Goodwin Jr. *J. Catal*. 137 (1992) 22.

[164] J. Y. Park, Y. J. Lee, P. K. Khanna, K. W. Jun, J. W. Bae, Y. H. Kim, *J. Mol. Catal. A*, 323 (2010) 84.

[165] H. M. Torres-Galvis, J. H. Bitter, T. Davidian, M. Ruitenbeek, A. I. Dugulan, K. P.de Jong. *J. A. C. S*. 134 (2012) 16207.

[166] C. S. Kellner, A. T. Bell, *J. Catal*. 75 (1982) 251.

[167] K. J. Smith, R. C. Everson, *J. Catal*. 99 (1986) 349.

[168] E. Iglesia, S. L. Soled, R. A. Fiato, *J. Catal*. 137 (1992) 212.

[169] J. Kang, W. Deng, Q. Zhang, Y. Wang. *J. Energy Chem*. 22 (2013) 321.

[170] J. M. G. Carballo, J. Yang, A. Holmen, S. García-Rodríguez, S. Rojas, M. Ojeda, J. L. G. Fierro, *J. Catal*. 284 (2011) 102.

[171] N. Lohitharn, J.G. Goodwin Jr. *J. Catal*. 260 (2008) 7.

[172] M. C. Ribeiro, G. Jacobs, B. H. Davis, D. C. Cronauer, A. J. Kropf, C. L. Marshall, *J. Phys. Chem*. 114 (2010) 7895.

[173] M. Guraya, S. Sprenger, W. Rarog-Pilecka, D. Szmigiel, Z. Kowalczyk, M. Muhler. *Appl. Surf. Sci*. 238 (2004) 77.

[174] K. Aika, K. Shimazaki, Y. Hattori, A. Ohya, S. Ohshima, K. Shirota, A. Ozaki. *J. Catal*. 92 (1985) 296.

[175] Z. Kowalczyk, M. Krukowski, W. Raróg-Pilecka, D. Szmigiel, J. Zielinski. *Appl. Catal. A*, 248 (2003) 67.

[176] Guczi, Eds, *New trends in CO activation, Studies on Surface Science Catalysis*, vol. 64, Elsevier, Amsterdam (1991) pp. 494.

[177] *Progress in C1 Chemistry*, Kodansha, Tokyo (1989) pp. 394.

[178] M. K. Niemelä, A. O. I. Krause, T. Vaara, J. J. Kiviaho, M. Reinikainen. *Appl. Catal. A*, 147 (1996) 325-345.

[179] H. C. Foley, A. J. Hong, *Appl. Catal*. 61 (1990) 351-375.

[180] A. Guerrero-Ruiz, A. Sepúlveda-Escribano, I. Rodríguez-Ramos, *Appl. Catal. A: Gen*. 120 (1994) 71-83.

[181] R. Burch, A. R. Flambard, *J. Catal*. 86 (1982) 384.

[182] W. M. H. Sachtler, M. J. Ichikawa, *J. Phys. Chem*. 90 (1986) 4752-4758.

[183] W. M. H. Sachtler, D. F. Shriver, W. B. Hollenberg, A. F. Lang, *J. Catal*. 92 (1985) 429.

[184] A. Miyamoto, N. Takahashi, M. Fukagaya, T. Hattori, Y. Murakami, *J. Phys. Chem*. 90 (1986) 5197-5201.

[185] A. Griboval-Constant, J-M. Giraudon, G. Leclercq, L. Leclercq, *Appl. Catal. A: Gen*. 260 (2004) 35-45.

[186] C. E. Scott, T. Romero, E. Lepore, M. Arruebarrena, P. Betancourt, C. Bolfvar, M. J. Pérez-Zurita, P. Marcano, J. Goldwasser, *Appl. Catal. A: Gen*. 125 (1995) 71-79.

[187] M. Inoue, T. Miyake, Y. Takegami, T. Inui, *Appl. Catal*. 29 (1987) 285-294.

[188] M. Inoue, T. Miyake, Y. Takegami, T. Inui, *Appl. Catal*. 11 (1984) 103-116.

[189] N. Takahashi, T. Mori, A. Miyamoto, T. Hattori, Y. Murakami, *Appl. Catal*. 22 (1986) 137-146.

[190] A. Juan, D. E. Damiani, *Catal. Today*, 15 (1992) 469-480.

[191] C. E. Scott, P. Betancourt, M. J. P. Zurita, C. Bolívar, J. Goldwasser, *Appl. Catal. A: Gen*. 197 (2000) 23-29.

[192] H. Chen, A. A. Adesina, *Appl. Catal. A: Gen*. 112 (1994) 87-103.

[193] M. J. P. Zurita, I. S. Henriquez, M. R. Goldwasser, M. L. Cubeiro, G. C. Bond, *J. Mol. Catal*. 88 (1994) 213-222.

[194] M. Inoue, T. Miyake, S. Yonezawa, D. Medhanavyn, Y. Takegami, I. Inui, *J. Mol. Catal*. 45 (1988) 111.

Chapter 2

Objectives

As explained in the Introduction Chapter, there is currently a growing interest in the production of clean liquid fuels for transport and chemicals feedstock such as, ethylene and propylene, from synthesis gas through the Fischer-Tropsch process. In this scenario, Ru catalysts are highly attractive and effective mainly due to their activity for the CO hydrogenation producing high molecular weight hydrocarbons working at high pressure and low temperature. Ru-based catalysts have the advantage that can operate under conditions of high partial pressure of H_2O and other atmospheres of oxygenated compounds (i.e. CO_2), which is vital when working with synthesis gas proceeding from biomass.

In addition, Ru catalysts are suitable for fundamental research to gain insights into the catalyst functioning and/or reaction mechanisms. In this line, it has been chosen an inert support in order to avoid the metal-support interaction effects. The major drawback of this metal for industrial application is its high cost and its limited availability. Therefore it is necessary to maximize its efficiency towards the desired fractions with the goal of making this route more competitive industrially with regard to Fe or Co processes. As with the Fe and Co-based catalysts, the catalytic performance of the Ru catalysts is modified with the addition of different elements which improves the catalytic activity, the selectivity and thermal stability.

To develop specific targets, the Thesis is structured in several chapters:

Chapter 4 focuses on the study of the local chemical environment and the electronic structure of the active metal (Ru) and the promoter (Cs) in situ when a Fischer-Tropsch atmosphere is applied. For this purpose X-ray absorption spectroscopy will be employed.

Due to the fact that the Fischer-Tropsch synthesis is a highly structure-sensitive reaction, Chapter 5 sheds light on the effect of ruthenium particle size in terms of activity and products selectivity. In addition, the effect of promotion with Cs will be evaluated pretending to increase the C_{5+} selectivity and the olefin to paraffin ratio in the C_2-C_4 hydrocarbons range.

The effect of the Cs and Ru precursor on the Fischer-Tropsch synthesis will be studied in chapter 6. For that, the incorporation of ruthenium will be carried out using two different precursors: $Ru(NO)(NO_3)_3$ and $RuCl_3$ xH_2O. Cesium will be employed as promoter and two precursors will also be used: $Cs(NO_3)$ and CsCl. The intention is to observe and try to explain modifications in the selectivity values.

Finally, our approach in Chapter 7 consists in evaluating a transition metal oxide as promoter to attain the optimal catalytic performance in FT processes. Transition metal oxides might be expected to have inherently interesting properties since early metals tend to be quite oxophilic forming strong bonds with oxygen. The influence of Mo promotion on the activity and selectivity of a Ru supported catalyst will be examined.

Chapter 3

Experimental

Volumetric equipment coupled to microcalorimeter.

In this Chapter the materials, methods and equipment used in the preparation, characterization and evaluation of the catalytic activity of different catalysts used in the development of this Doctoral Thesis are described. The Chapter is divided into three sections: materials and methods for catalyst preparation, techniques used in the characterization of catalyst structures, and description of the equipment used in the evaluation of the catalytic activity.

3.1. Materials and methodology in the catalysts preparation

The catalysts used in the development of this Doctoral Thesis were prepared by two different methods such as, incipient wetness impregnation (IWI) and wetness impregnation (WI). In the IWI method the metal-containing solution is added to the catalyst support with the same pore volume as the volume of the solution that is added. While in the WI method a metal-containing solution volume in excess to the support pore volume is added and further desiccated in a rotary evaporator. In chapter 4, a high surface area graphite TIMCAL (G, $S_{BET=}$ 399 $m^2 \cdot g^{-1}$) was used as catalyst support. The monometallic ruthenium catalyst was prepared by incipient wetness impregnation method, using ruthenium chloride hydrate in H_2O:Ethanol (1:1) solution as metal precursor, in the adequate concentration to incorporate 4 wt% Ru to the support (4Ru/G catalyst). After impregnation, the catalyst was kept at room temperature over the night and later heated at 120 ºC during 24 h. The addition of the cesium promoter was carried out by successive incipient wetness impregnation of an aliquot of the 4Ru/G catalyst with a H_2O:Ethanol (1:1) solution of cesium chloride to introduce a 4 wt% Cs in the sample (4Ru4Cs/G catalyst). Subsequently the catalyst was dried at 120ºC for 24h. Cs promoted blank sample (4 wt%) was also prepared. In chapter 5, two

different high surface area graphites from TIMCAL (G100, S_{BET} = 100 $m^2 \cdot g^{-1}$ and G400, S_{BET} = 400 $m^2 \cdot g^{-1}$) were used as catalyst supports. The monometallic ruthenium catalysts were prepared by incipient wetness impregnation using water:ethanol (1:1) solutions of ruthenium chloride hydrate ($RuCl_3 \cdot xH_2O$ from Aldrich) in the adequate concentration to incorporate 20, 10 and 5 wt% Ru to the support. After impregnation, the catalysts were kept at room temperature overnight and later heated at 393 K during 24 h. The ruthenium and cesium bimetallic catalysts were prepared by incipient wetness co-impregnation with water:ethanol (1:1) solutions of ruthenium chloride and cesium choride with adequate concentrations to obtain a Ru/Cs ratio of 20. In chapter 6, the selected catalyst support was a high surface area graphite TIMCAL (S_{BET} = 399 $m^2 \cdot g^{-1}$). The incorporation of ruthenium was carried out using two different precursors: $Ru(NO)(NO_3)_3$ from Alfa-Aesar and $RuCl_3$ xH_2O from Aldrich. Cesium was employed as promoter and two precursors were also used: $Cs(NO_3)$ and CsCl, both obtained from Aldrich. All the catalysts were prepared by the incipient wetness impregnation method using a solution of ethanol-water (1:1) with the adequate concentration of the salts to incorporate 4 wt% Ru and/or 4 wt% of Cs to the support. After impregnation, the catalysts were kept at room temperature overnight and later heated at 393 K during 24h. The following abbreviations are used for precursors in conjunction with the catalyst: N for nitrates and Cl for chlorides compounds. Finally in chapter 7, a high surface area graphite TIMCAL (G, $S_{BET=}$ 100 $m^2 \cdot g^{-1}$) was used as catalyst support. First, the support was impregnated with molybdenum by incipient wetness impregnation method, using ammonium molybdate tetrahydrate ($H_{24}Mo_7N_6O_{24}$ $.4H_2O$, Aldrich) in H_2O solution as metal precursor, in the adequate concentration to incorporate wt% Mo

to the support. After the impregnation, the catalyst was kept at room temperature over the night and later heated at 393 K during 24 h. Triruthenium dodecarbonyl ($Ru_3(CO)_{12}$, Aldrich) was employed as ruthenium precursor. It was dissolved in 50 cm^3 of acetone and introduced in a rotavapor at 50 rpm during 30 min together with the previous impregnated support. After that, acetone was evaporated at 323 K. Table 3.1 summarizes the supports, metal precursors and wt % utilized to prepare the catalysts in each chapter.

Table 3.1. Catalysts composition, supports and metal precursors used in the development of the Doctoral Thesis.

Chapter	Catalyst	Support	Metal precursor	Wt (%)
4	Ru, RuCs	G (399 $m^2 g^{-1}$)	$RuCl_3 \cdot xH_2O$, Aldrich CsCl, Aldrich	4 4
5	Ru, RuCs	G (399 $m^2 g^{-1}$) G (100 $m^2 g^{-1}$)	$RuCl_3 \cdot xH_2O$, Aldrich CsCl, Aldrich	(20, 10, 5) Cs = Ru/20
6	Ru, RuCs	G (399 $m^2 g^{-1}$)	$RuCl_3 \cdot xH_2O$, Aldrich CsCl, Aldrich $Ru(NO)(NO_3)_3$, Alpha-Aesar $CsNO_3$, Aldrich	4 4 4 4
7	Ru, RuMo	G (100 $m^2 g^{-1}$)	$Ru_3(CO)_{12}$, Aldrich $H_{24}Mo_7N_6O_{24}.4H_2O$, Aldrich	2 (5, 1, 0.5, 0.1, 0.05)

3.2. Characterization techniques

This section briefly describes the fundamentals of experimental procedures and characterization techniques employed along the development of this study. The results obtained from these techniques allow us to relate the catalytic behavior of the catalysts with their physical and chemical properties. All these techniques were employed in this study and the type of information provided by each of them are summarized in Table 3.2.

Table 3.2. Characterization techniques employed

Analytical technique	**Information**
Total reflection X-ray fluorescence (TRXF)	Composition
Nitrogen adsorption-desorption isotherms	Surface area
Powder X-ray diffraction (XRD)	Crystalline species
Termogravimetric analysis (TGA)	Weight change
H_2-Temperature-programmed reduction (H_2-TPR)	Reducibility
Temperature-programmed desorption (DTP)	Surface species
CO chemisorption microcalorimetry	Heats of CO adsorption and metal dispersion
High-resolution transmission electron microscopy (HRTEM)	Distribution and morphology of phases
X-ray photoelectron spectroscopy (XPS)	Chemical state and composition of surface atoms
In situ X-ray absorption spectroscopy (XAS)	Local geometric and electronic structure

3.2.1. Total reflection X-ray fluorescence (TRXF)

Total-reflection X-ray fluorescence (TRXF) is a well-known technique [1] more and more applied in very diverse scientific fields. Many applications have been developed up to now, i.e. catalytic processes studies [2, 3], biochemistry or cellular toxicity studies [4, 5, 6], materials physics [7, 8, 9], and archaeometry [10, 11, 12]. TRXF is used primarily for micro (0.01 – 1 %), trace (0.1 – 100 ppm) and ultratrace (below 100 ppb, μg/Kg) analyses. To date, TRXF has begun to implement successfully to solve the problematic matrix effects in many scientific fields such as medicine, environmental sciences, biology, nanotechnology etc. TRXF can analyze all elements with Z > 13 if it is used the appropriate excitation sources. The technique is based on:

1) An X-ray quantum hits an inner shell electron in a (sample) atom. The electron is removed leaving the atom in an excited state.
2) The missing inner shell electron is replaced by an electron from an outer Shell.
3) The energy difference between the inner and outer shell is balanced by the emission of a photon (X-ray fluorescence radiation). This phenomenon is shown in the figure 3.1.

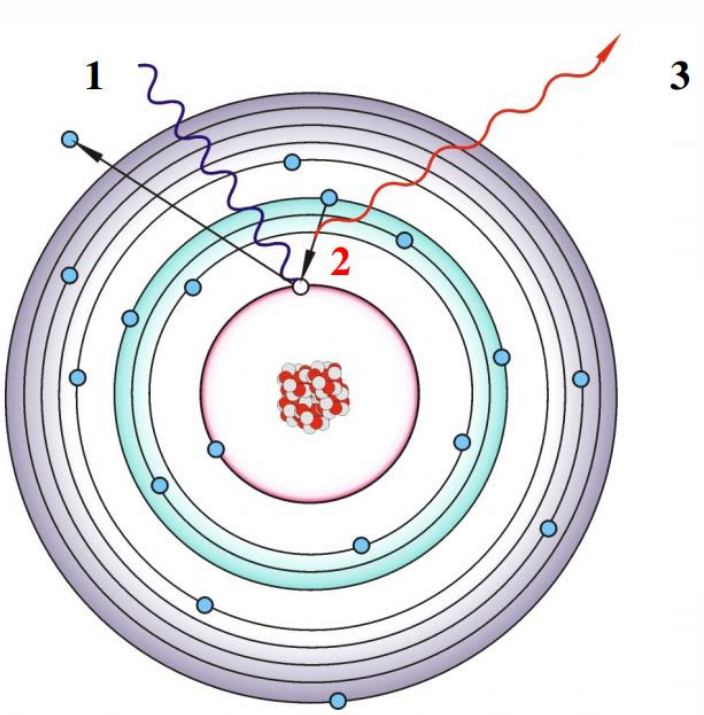

Figure 3.1. Principle of Total-reflection X-ray fluorescence (TRXF).

The energy, and therefore the wavelength, of the X-ray fluorescence radiation is characteristic for the different chemical elements (Qualitative Analysis) while the intensity of the X-ray fluorescence radiation is, in first approximation, proportional to the element concentration (Quantitative analysis).

Each element shows a specific line pattern in a spectrum depending on the orbitals involved:

- L → K transition = Kα line
- M → K transition = Kβ line
- M → L transition = Lα line
- N → L transition = Lβ line

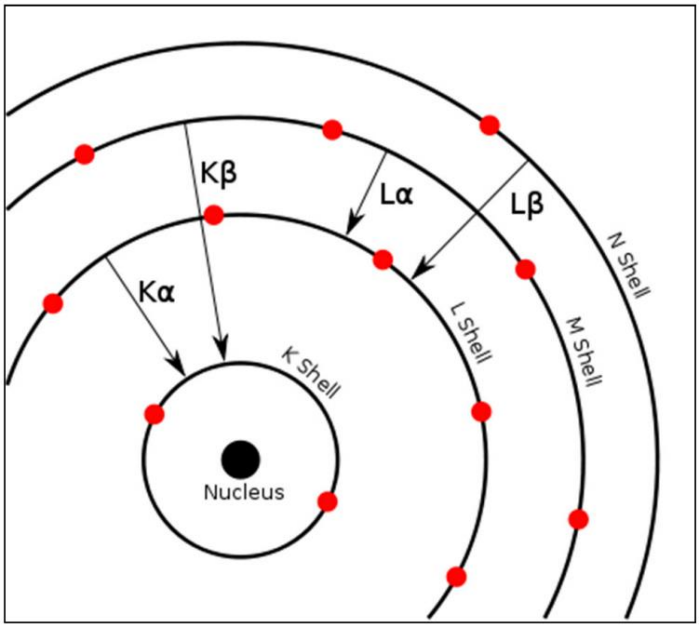

Figure 3.2. Specific line pattern in a spectrum depending on the orbitals involved.

The electron relaxation times are very short, on the order of 10^{-8} - 10^{-9} s, so this technique is an extraordinarily rapid analytical method. Figure 3.3 shows a basic design of a TRXF instrument.

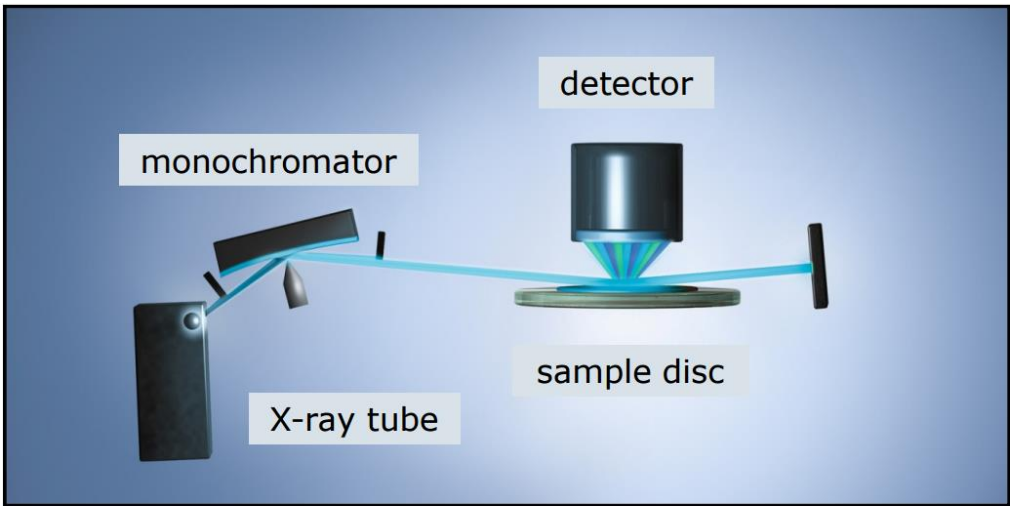

Figure 3.3. Design of a TRXF instrument.

The analyses were carried out at the Interdepartmental Research Service of the Autonomous University of Madrid (UAM SIDI) following the protocol developed by Fernandez-Ruiz et al. [13].

3.2.2. Nitrogen adsorption-desorption isotherms

Frequently gas adsorption, and particularly physical adsorption at low temperatures, is used for the determination of the specific area and pore distribution of solid materials. The most extensively used method is based in the determination of nitrogen adsorption-desorption isotherms at the liquid nitrogen temperature (-196 °C). This method consists in representing the volume of adsorbed nitrogen per gram of the solid material, versus the equilibrium pressure, normally expressed as the relative pressure (P/P_0), where P_0 is the pressure of vapour saturation of nitrogen at -196 °C. The amount of adsorbed gas at the equilibrium pressure is given by the difference between the amount of gas introduced and the amount required to fill the space around the adsorbing solid, i.e. the dead volume at the equilibrium pressure. Before determining the adsorption isotherm, the samples are degassed to remove all physisorbed species from their surface.

One of the most common method of measuring surface area, and widely used in most catalysis characterizations, is that developed by Brunauer, Emmett, and Teller (BET) in the late 1930's [14]. The pore distribution information determines by the analysis the shape of the isotherm (adsorption-desorption branches). The BET method consists in calculating the monolayer volume (V_m) of the adsorbed species. With this value, the specific BET surface area can be calculated using the equation 3.1:

$$S_{BET} = \left(\frac{V_m}{M \cdot g}\right) \cdot N_A \cdot \sigma \qquad \text{(Equation 3.1)}$$

Where V_m is the monolayer volume, M is the molar volume, g is the weight of adsorbent employed, N_A is the Avogadro number ($6.022 \cdot 10^{23}$ atoms/mol), and σ is the cross-sectional area covered by one nitrogen molecule. According to IUPAC, the value of σ in the case of liquid nitrogen is 0.162 nm^2 [15].The value of V_m is obtained by adjusting the adsorption experimental data to the BET isotherm:

$$\frac{P}{V_{ads}(P_0 - P)} = \frac{1}{V_m \cdot C} + \frac{(C-1)P}{V_m C P_0} \qquad \text{(Equation 3.2)}$$

Where P is the equilibrium pressure, P_0 is the normal vapour saturation pressure for liquid nitrogen at the experimental temperature (-196 °C), C is a constant related with the condensation heat and adsorption of the adsorbate, V_{ads} is the volume of gas adsorbed at pressure P expressed in cm^3. If only the section where the monolayer is formed is considered, representing the experimental data of $P/V_{ads}(P_0-P)$ versus P/P_0, should give a straight line according to the above BET equation; the slope is $(C-1)/V_mC$ and the intercept is $1/V_mC$. These values can be used to determine V_m and C.

The BET model is an extension of the Langmuir theory which considers multilayer adsorption. The application of this method is limited to a reduced range of pressures where the equation adjusts well to the experimental data. Practically, the linearity is maintained for $0.05 < P/P_0 < 0.3$ approximately, and it is in this interval that the BET model can be applied. Below this limit, the micropores are filled and adsorption on the more reactive sites is favoured, while above this limit capillary condensation takes place.

The nitrogen adsorption-desorption isotherms presented in this report were carried out using an automatic Micromeritics Asap 2020. Prior to analysis, samples were degassed at 413 K for 16 h in a vacuum system for removing gaseous and / or liquid contaminants retained in the pores and the external surface.

3.2.3. Powder X-ray diffraction (XRD)

X-ray diffraction is based on the reflection of the electromagnetic waves that are irradiated by the successive planes of the crystal atoms. When an X-ray beam reaches a crystal surface under any θ angel (Figure 3.4), a part of the radiation is reflected, while another part penetrates further. This situation repeats itself in the successive layers. It is necessary that the difference between the routes of two diffracted waves is an integer number of wavelengths (nλ). In this way, for two waves that are reflected in a point P, the difference in the routes in the two first planes is δ = AB + BC. From the summary of the system, AB = BC and δ = 2 * AB and therefore δ = 2 sin (θ). The reflection condition elaborated by Bragg and Bragg indicates that the difference in the routes followed must be an integer number of the wavelength [16]. The wavelength is given by the following equation:

$$n\lambda = 2d \sin(\theta) \qquad \text{(Equation 3.3)}$$

Where n is the order of reflection (integer), λ is the incident wavelength, d is the distance between two consecutive planes and θ is the angle between the incident beam and the sample.

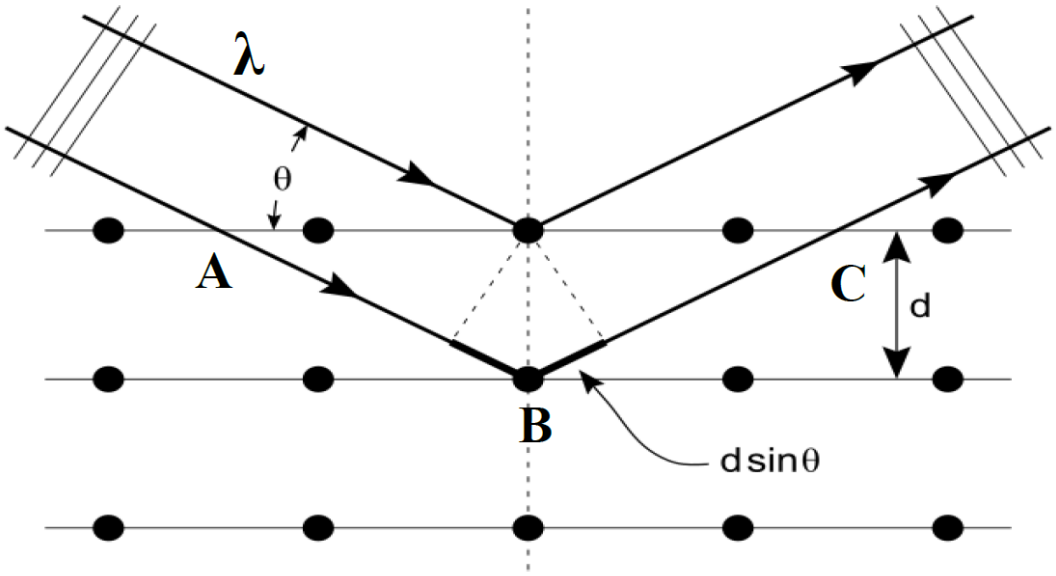

Figure 3.4. Derivation of Bragg's law.

The distance between the different planes of the crystal lattice determines the value of the Bragg angle, which is considered as a fingerprint of the crystalline solid. According to this way, the diffraction patterns provide unmistakable information about the crystalline structure. The angular position of the maximum points of the diffraction patterns are related with the parameters of the unit cell (repeated cell in the crystal), while their intensities reflect the symmetry of the lattice and the electronic density in the unit cell. Almost every crystalline substance has a unique powder X-ray diffraction pattern in terms of the location of the observed peaks and its intensities. If there is a mixture of different components, each phase produces its own diffraction pattern independently of the other phases; therefore this technique can be used to identify phases in such mixtures by comparison with patterns stored in the Joint Committee on Powder Diffraction Standards (JCPDS) databases. There is a formula that relates the size of sub-micrometre particles, or crystallites, in a solid to the broadening of a peak in a diffraction pattern. It is named after Paul Scherrer [17, 18]. It is used in the

determination of size of particles of crystals in the form of powder. The Scherrer equation can be written as:

$$\tau = \frac{K\,\lambda}{\beta \cos\theta} \qquad \text{(equation 3.4)}$$

Where τ is the mean size of the ordered (crystalline) domains, which may be smaller or equal to the grain size; K is a dimensionless shape factor, with a value close to unity. The shape factor has a typical value of about 0.9, but varies with the actual shape of the crystallite; λ is the X-ray wavelength; β is the line broadening after subtracting the instrumental line broadening by the equation $\beta = \sqrt{B^2 - b^2}$ where B is the line broadening at half the maximum intensity and b the instrumental line broadening in radians. The applicability of this equation in supported metal catalysts is conditioned by the detection limit. A minimum wt % is required (1-5 %). Furthermore, this method is applicable only for particles sizes between 4.5 and 50 nm, because below that range the line is very wide and diffuse, and above the method is very insensitive.

The equipment used in the analysis is a X Policristal X´Pert Pro PANalytical X-ray diffractometer with a configuration θ - 2θ. The equipment allows qualitative, quantitative and low angle analysis, using CuKα radiation (λ = 1.5406 Å, 45 kV, 40 mA). The apparatus has a fast X'Celerator detector and an autosampler of 15 positions that allows the analysis of large numbers of samples at relatively short times with regard to conventional detectors.

3.2.4. Termogravimetric analysis (TGA)

This technique studies the percentage change in the weight of the sample as a function of temperature using a controlled atmosphere. When this technique is

applied to carbon in an inert atmosphere gives an idea of the thermally unstable functional groups that are present in the sample. The measurement system used was an electronic balance, CI Electronics microbalance MK2–MC5, with two arms. When weight loss occurs, one of the arms is deviated and it is compensated by an electric current applied. Amplification of the electrical signal, previously calibrated, gives us information about weight loss [19].

In some cases, ruthenium loading in the catalysts (Ru/G) was measured by thermogravimetric analysis, burning 150 mg of sample in flowing pure air (50 mL min^{-1}) at 1073 K and weighing then the residual product which was identified as RuO_2 by XRD.

3.2.5. H_2-Temperature-programmed reduction (H_2-TPR)

Temperature programmed reduction (TPR) has been proved as a powerful technique to analyze the kinetic reduction process of metal oxide precursors. Since hydrogen consumption is proportional to the amount of reducible material, TPR is a valid technique to determine the amount of reducible species in a catalyst sample. This technique can be also used to study the effect of the support and promoters on the extent of reduction.

In the TPR technique a reducing gas mixture is flowed over an oxidized catalyst, while it is subjected to a programmed linear temperature ramp. Usually hydrogen diluted in an inert gas such as helium or argon. The sample temperature is increased at a constant ramping rate and hydrogen is consumed from the gas mixture as the reduction takes place [20]. Outlet gas stream is continuously analyzed by a gas chromatograph which allows to observe the change in the concentration of H_2 and to observe the appearance of other compounds, such as the precursor decomposition or unstable groups from the support.

200-300 mg of sample was introduced inside a quartz reactor inserted in a programmable oven (temperature controller RKC Rex-P90 and a thermocouple type K). The temperature was increased from room temperature to 750 K at 5 K/min. The gas flows (60 cm^3/min, 5 % H_2/Ar) were controlled by mass flow controllers (Brooks 5850 TR). Finally, the gas outlet stream was analyzed using a gas chromatograph (Varian 3400) equipped with a thermal conductivity detector and employing the Chromosorb 102 and Porapack Q columns for the separation of H_2, CO, CO_2 and CH_4 principally.

3.2.6. Temperature-programmed desorption (TPD)

This technique is complementary to thermogravimetry analysis allowing us to complete the surface characterization of materials [21, 22]. The aim of the technique is to follow species desorption present on a surface. For that, the sample is subjected to a temperature program in inert atmosphere or vacuum while the gas phase produced is analyzed by a mass spectrometer (see figure 3.5).

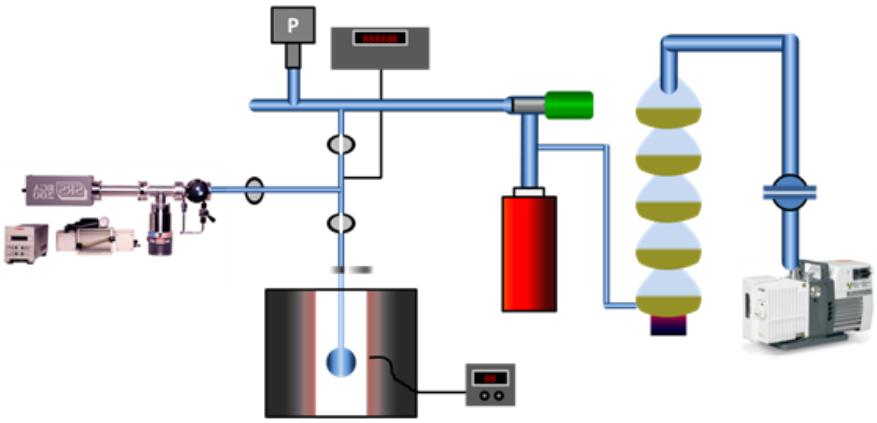

Figure 3.5. Temperature-programmed desorption equipment.

To perform the experiment it is used approximately 50 mg of sample which is place inside a quart reactor. Then, the sample is connected to the vacuum pump

for 30 min in order to remove the physisorbed water. Later, it is proceeded to heat the sample at a constant rate of 5 K min^{-1} from room temperature to 1123 K while the desorbed compounds are analyzed by a mass spectrometer (SRS RGA200).

3.2.7. CO chemisorption microcalorimetry

CO uptake and the evolution of CO adsorption heat were recorded in a Tian Calvet heat-flow microcalorimeter (Setaram C-80 II) isothermally operated at 331 K and connected to a glass vacuum-dosing apparatus (See figure 3.7). For each CO adsorbed amount, the equilibrium pressure was measured by means of Baratron capacitance manometers (MKS Instruments). First, the samples (portions of 150 mg) were introduced inside a glass reactor (as it is shown in Figure 3.6) in order to be activated by reduction in H_2 (60 cm^3/min) at 673 K for 2 h and, after outgassing at this temperature for 16 h, were cooled to 331 K. Then, successive doses of CO were sent onto the sample until a surface ruthenium coverage of one was obtained. The calorimetric and volumetric data were stored and analyzed by microcomputer processing.

Metal dispersion (D_{CO}) was estimated assuming the chemisorption of one CO molecule per surface ruthenium atom. The dispersion is defined as:

$$D_{CO} = \frac{M_s}{M_t} \qquad \text{(equation 3.5)}$$

Where M_s is the metal atoms number on the surface and M_t is the total metal atoms number. Knowing the value of dispersion (D_{CO}), and assuming that the metal particles are spherical it is possible to calculate the average particle size:

$$D = \frac{N_s}{N_v} \cdot \frac{6}{\bar{d}} = \frac{16.3}{74.19} \cdot \frac{6}{\bar{d}} \qquad \text{(equation 3.6)}$$

Where N_s is the number of atoms per unit area of metal on the surface and N_v is the concentration of atoms per unit volume [23].

The total CO uptake at the monolayer was considered to be attained when the evolved heat falls below the physisorption threshold (40 kJ/mol) [24]. Representing the adsorption differential heat (e.g. joule per mole of adsorbed gas) versus the amount (moles) adsorbed per gram of catalyst it is obtained the adsorption microcalorimetry profile. The experimental system in represented in Figure 3.8.

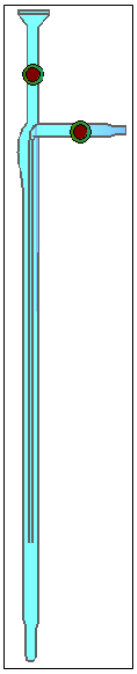

Figure 3. 6 Glass reactor for adsorption microcalorimetry experiments.

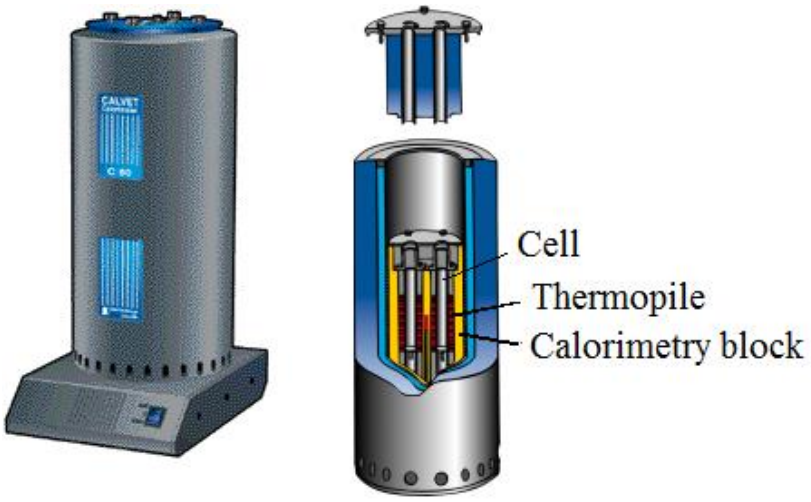

Figure 3.7. Tian Calvet microcalorimeter (Setaram C-80 II).

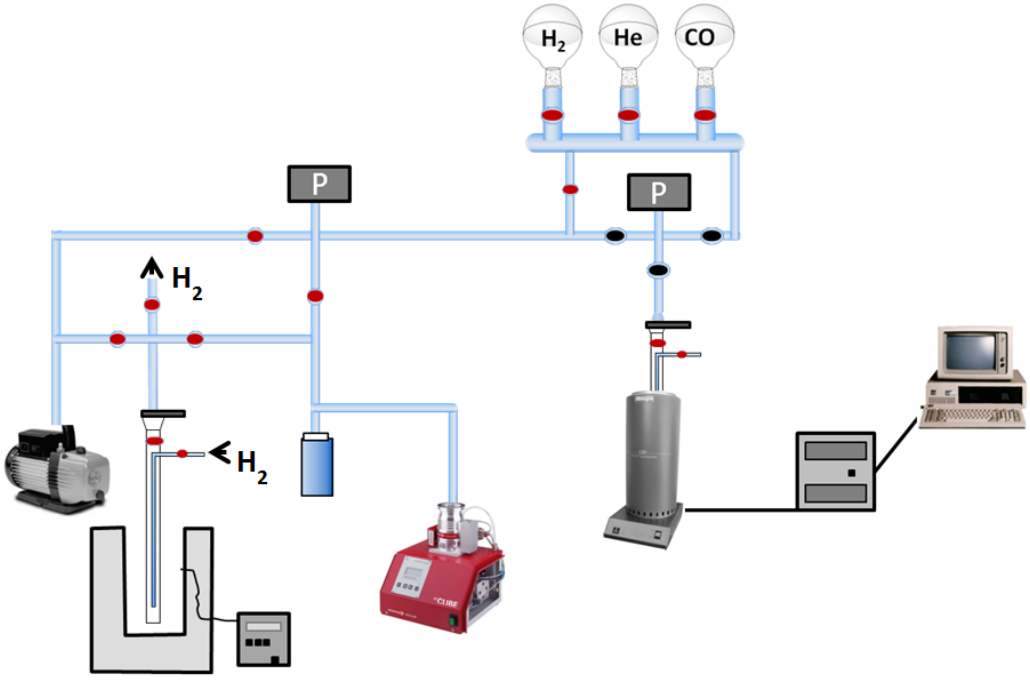

Figure 3.8. Volumetric equipment coupled to microcalorimeter.

The volumetric equipment consists of two pumps (one rotary and another turbomolecular), a liquid nitrogen trap to improve the vacuum, a set of automatic keys in order to introduce the gas doses and two pressure gauges: one Alcatel

CF2P (to measure the residual pressure 10^{-2}-10^{-7} Torr) and another Baratron MKS 270B (with a working range between: 1 - 10 Torr).

3.2.8. High-resolution transmission electron microscopy (HRTEM)

Transmission electron microscopy is a technique commonly used for chemical and structural characterization of materials. This technique provides information about morphology, particle size distribution, chemical composition, degree of crystallinity and identification of crystal phases [25]. The technique is based on the interaction of the material with an electron beam accelerated under a differential electric potential of several hundred kilovolts, which is collimated, focused and guided by several electromagnetic lenses. Depending on how the beam is modulated it is possible to obtain transmission electron microscopy (TEM) which occurs when a parallel beam is projected to the sample or scanning transmission electron microscopy (STEM) when the beam converges on a point of order of 1 nm and with this a swept of the sample is maked. In TEM mode the electrons used to generate the image are the transmitted electrons (they do not suffer interaction with the matter), while in STEM mode electrons that are used to generate the image are those which are dispersed during the collision with the sample atoms.

Besides, the microscope may be equipped with an energy dispersive X-ray spectrometer (EDX). This allows knowing the elemental composition of a studied sample area and it can even make a composition maps "mapping" (when the STEM mode and EDX are coupled).

To carry out the analysis, first the catalysts must be reduced. The experimental procedure consists of a first grinding step to convert the sample into a fine powder which is then suspended in a volatile solvent (ethanol). After that, a

couple of drops are added to the copper grid (Lacey coal, 200 mesh, Aname) and this is placed on the sample carrier. Before the analysis, the sample should be degassed. The microscope used in these studies was a JEOL 2100F electron-gun microscope operating at 200 kV with a maximum resolution of 0.17 nm and a minimum size of beam convergence of 0.2 nm in STEM mode, and equiped with an energy-dispersive X-ray detector EDX INCAX-Sight system from Oxford Instruments.

To calculate the distribution and the average particle size more than 350 particles have been counted using the following equation [26]:

$$d_{TEM} = \frac{\sum_i n_i d_i^3}{\sum_i n_i d_i^2} \qquad \text{(equation 3.7)}$$

Where n_i is the number of particles with diameter d_i.

This equation is used when there are particles of similar shapes, but different sizes. The average value obtained d_{TEM}, can be used to compare with other techniques which estimate the average particle size from the metal surface area, such as the chemisorption [27].

3.2.9. X-ray photoelectron spectroscopy (XPS)

The X-ray photoelectron spectroscopy is a technique of electron spectroscopy for chemical analysis that is used to determine the surface composition of the sample, the oxidation state of the atoms and their chemical environment in the sample. This technique is based on the photoelectric effect represented in figure 3.9. When a sample is irradiated with a beam of high energy X-rays (hυ), an emission of electrons, from the internal levels of the atoms of the samples, takes place. A hemispherical detector detects the electrons emitted and records their energy to obtain the X-ray photoelectron emission spectrum. The

electrons that possess a binding energy lower than the energy of the exciting X-rays, are emitted with a certain kinetic energy that must fulfill the equation of the photoelectric effect:

$$E_C = h\upsilon - E_b - \Phi \qquad \text{(equation 3.8)}$$

Where E_C is the kinetic energy of the emitted electron, hυ is the exciting energy, E_b is the binding energy of the excited electron, and Φ is the work function of the spectrometer.

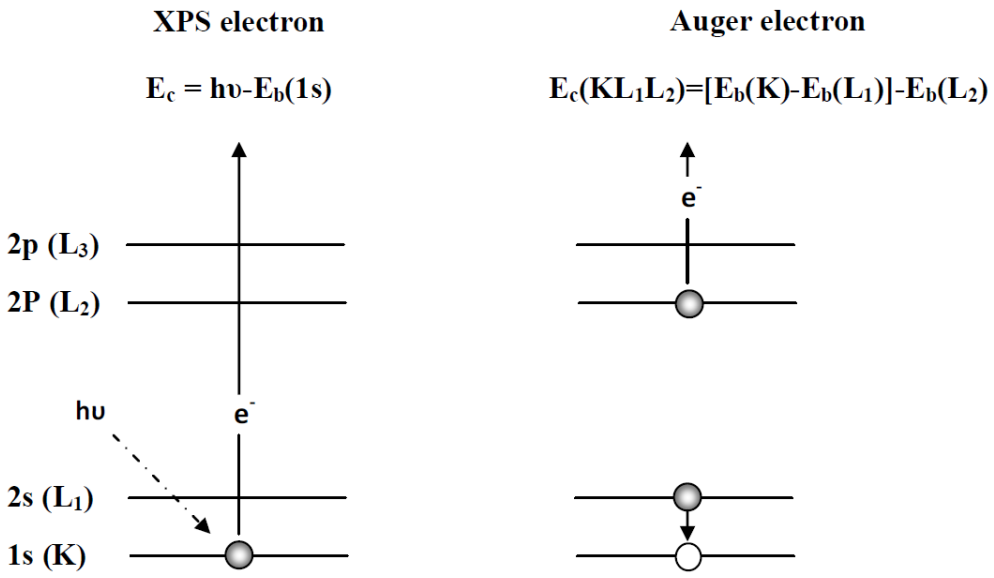

Figure 3.9. Photoelectric effect and Auger processes.

In an XPS spectrum, the intensity of the flow of emitted electrons by the sample is represented as a function of their kinetic energy or more frequently as a function of their binding energy. The kinetic energy of the emitted electrons is related to their binding energy (BE), which is characteristic of the elements present in the sample and the electronic interactions between them [28].

X-ray photoelectron spectra of the catalysts were recorded with an electron spectroscopy system SPECS GmbH with UHV system, energy analyzer

PHOIBOS 150 9MCD using a monochromatic X-ray source (with double anode Al/Ag), source of electrons for charge compensation, ultraviolet photon source, ion source and sample pretreatment chamber (HPC). Each sample was pressed into a small pellet of 10 mm diameter, placed in the sample holder and degassed in the chamber for 24 h to achieve a dynamic vacuum below 10^{-10} mbar before analysis. The catalysts were first activated by reduction in H_2 flow (70 ml/min) at 673 K during 1 h in the sample pretreatment chamber. The spectral data for each sample were analyzed using CASA XPS software. The C*1s* peak at 284.6 eV was used as an internal standard. The equipment error in the energy determinations is less than 0.01 eV. The relative concentrations and atomic ratios were determined from the integrated intensities of photoelectron lines corrected for the corresponding atomic sensitivity factor.

3.2.10. *In situ* X-ray absorption spectroscopy (XAS)

X-ray absorption spectroscopy (XAS) is a widely used technique for determining the local geometric and/or electronic structure of matter. The experiment is usually performed at synchrotron radiation sources, which provide intense and tunable X-ray beams. Samples can be in the gas-phase, solution, or condensed matter (i.e. solids).

XAS data is obtained by tuning the photon energy using two crystal monochromators to a range where core electrons can be excited (0.1-100 keV photon energy). The edge nomenclature depends upon which core electron is excited: the principal quantum numbers n = 1, 2, and 3, correspond to the K-, L-, and M-edges, respectively (see figure 3.10).

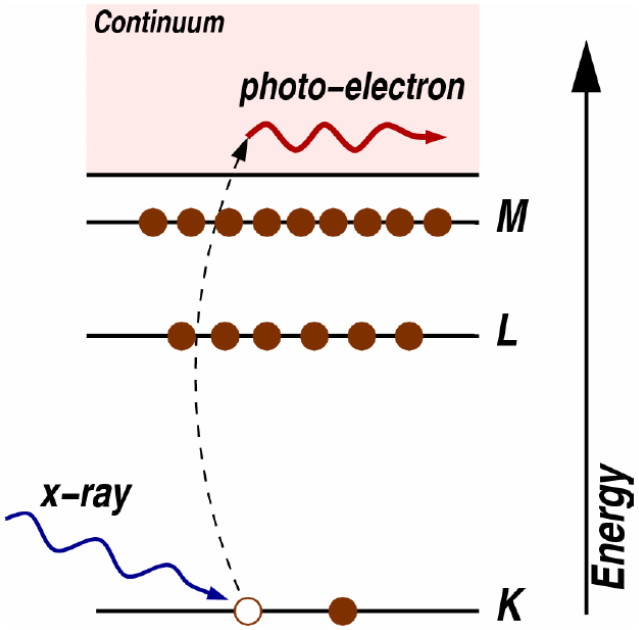

Figure 3.10. X-ray absorption phenomenon.

The x-ray absorption spectrum is typically divided into two regions: x-ray absorption near-edge spectroscopy (XANES) and extended x-ray absorption fine-structure spectroscopy (EXAFS) as it is shown in Figure 3.11. Though the two have the same physical origin, this distinction is convenient for the interpretation. XANES is strongly sensitive to formal oxidation state and coordination chemistry (e.g., octahedral, tetrahedral coordination) of the absorbing atom, while the EXAFS is used to determine the distances, coordination number, and species of the neighbors of the absorbing atom.

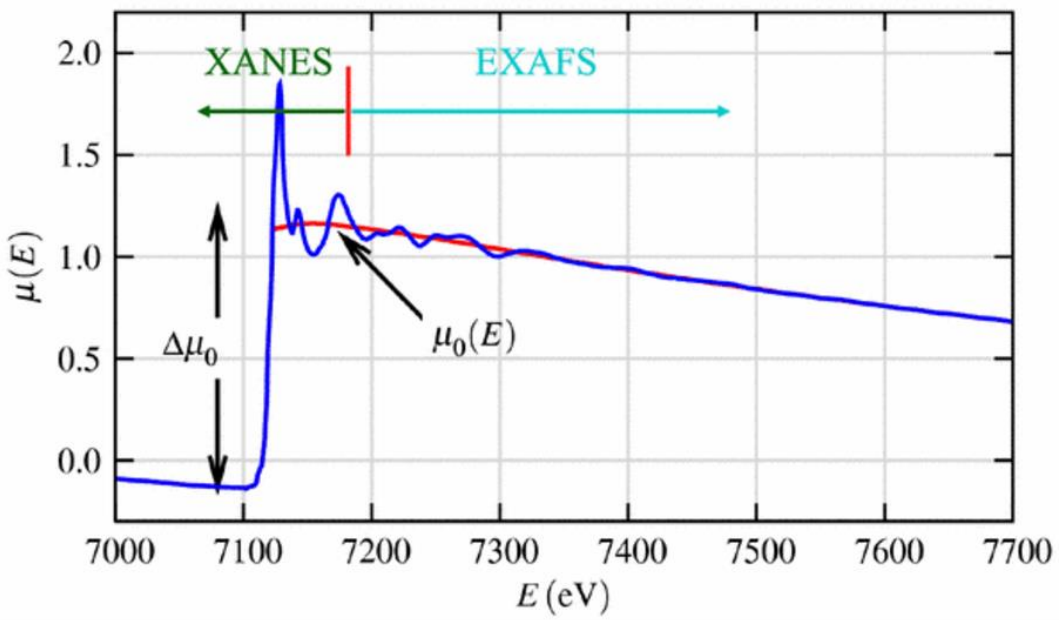

Figure 3.11. Regions in a spectrum of X-ray absorption.

XANES: region within ~ 50 eV of the absorption edge.

EXAFS: region well above the absorption edge, up to 1 keV.

To carry out the experiments, Ru K edge (22.117 eV) X-ray absorption measurements were recorded in dispersive mode at the EDXAS_L branch of the ID24 beamline at the European Synchrotron Radiation Facility (ESRF, Grenoble, France). The X-ray source consisted of two undulators whose gaps were adjusted to tune the first harmonic at energies covering the Ru K edge. The beam was focused horizontally by a curved polychromator (Si(111)) crystal in a Laue configuration and utilized a FReLoN CCD camera as a detector for time-resolved studies. The catalysts were pressed into pellets and sieved to a size between 0.160 and 0.180 mm. Then, the samples (ca. 15 mg) were loaded in a fixed bed of a plug-flow microreactor system for operando X-ray studies developed at ID24 which ensured a temperature control of ±1 °C. A flow of 11 mL min^{-1} of 10 % hydrogen in helium was fed to the reactor during temperature-programmed reduction experiments. The temperature was raised by 5 °C min^{-1} up to 400 °C.

XANES spectra were collected every 10 °C or 2 min during the heating. After the system was cooled to the reaction temperature (250 °C), time-resolved experiments with 10 cycles of 120 s switching the FT reactants at 1 bar total pressure (from 10 % H_2 in He to 5 % CO in He, constant flow of 11 mL min^{-1}) were performed. Time-resolved EXAFS spectra were recorded every 1.5 s.

Cs L_1 edge XANES spectra were recorded in transmission mode at beamline BL22-CLAESS of the ALBA Synchrotron (Barcelona, Spain) using a double monocromator (Si (111)). In situ temperature-programmed reduction was carried out in a reaction cell designed for XAS measurements under controlled conditions of solid-gas reactions. The sample as a 13 mm pressed pellet was loaded into the cell and continuously fed with 100 mL min^{-1} of 20 % H_2 in He. The temperature was increased at 5 °C min^{-1} from room temperature up to 400 °C. XANES spectra were collected every 15 °C or 3 min.

XAS Analysis procedures and results. XANES spectra in Ru K-edge were analyzed using the principal component analysis (PCA) method. PCA analysis assumes that a variable, in this case the absorbance in a set of spectra, can be mathematically modeled as a linear sum of individual (uncorrelated) components known as factors. An important property of this method is that each factor makes a maximum contribution to the sum of the variances of the variables; consequently, to determine the number of individual components, an F-test based on the variance associated with factor k and the summed variance associated with the pool of noise factors (n-k factors; being n the total number of spectra) was performed. A factor was accepted as a "pure" chemical species (i.e. a factor associated with signal and not noise) when the percentage of significance level of the F-test, %SL, was lower than a test level set in previous studies at 5%. The

latter means that the null hypothesis of the F test, e.g. that factor k is associated with noise, is rejected for %SL values below such limiting value. The ratio between the reduced eigenvalues, REV, which describes the ratio between the mathematical norm of factors, was also used in determining the number of chemical species present in the sample. This ratio should approach one (e.g. equal statistical "weight") for noise-only factors. These tests are fully described in the following reference [29].

After identifying the number of principal components, it is necessary to transform the obtained abstract solution into the real components, that is, the solution with spectroscopic meaning. This can be done from two different initial situations. The first occurs when the principal components can be chemically identified by a target test (using external references corresponding to pure components). Suitable standard compounds are obviously necessary within this option. The acute size/shape sensitivity of the XANES spectroscopy limits the viability of this option while working with nanoparticulate materials. A solution can still be found, even when the principal components have not been previously identified, by using iterative transformation factor analysis (ITFA), also known as selfmodeling curve resolution [30, 31]. In all procedures, the remaining problem is then to find the best transformation matrix, which rotates (through a nonorthogonal rotation) the abstract absorbance and concentration matrixes to an estimate of their real, physically meaningful forms. In the case of ITFA, a varimax rotation is previously performed in the abstract concentration matrix; this orthogonal rotation should align the abstract factors, as close as possible, along the unknown concentration profiles, revealing the reaction coordinate values (in our case, temperature under H_2 atmosphere) where the maximum concentration of

each of the pure components would be observed. Uniqueness concentration vectors (TEST vectors having a unity value at a single reaction coordinate point) associated with these times are then subjected to testing and refinement by iteration. Each individual concentration profile is refined by setting to zero any emerging negative value. The iteration is stopped when the error in the test vector (RET) is lower than the real error (average statistical error obtained from PCA). The transformation matrix is then obtained for the concentration profiles, and a similar procedure is performed with the abstract spectrum matrix. The abstract solution is thus rotated, and XANES spectra and corresponding concentration profiles of the pure chemical components are obtained. Results in the main part of chapter 4 are obtained through this second procedure.

EXAFS analysis of Ru K-edge results. Data reduction and analysis of the EXAFS (extended X-ray absorption fine structure) data was made using the VIPER (Visual Processing in EXAFS Researches) program [32]. The amplitude and phase-shift functions used for EXAFS analysis were obtained by FEFF-9 code [33]. Goodness of fitting was measured through the R value: $R(\%) = (R\,[\chi T - \chi E]k3\,dk/[\chi E]k3\,dk) \times 100\%$: χT being the theoretically calculated EXAFS and χE being the EXAFS obtained via experiment.

Ru K-edge EXAFS Fourier transforms for 4Ru/G catalyst after H_2 or CO exposure during the cyclic experiments and the EXAFS fitting data are presented in Fig. 4.9 and Table 4.4. As reference, EXAFS data of Ru foil normalized to the sample are shown in green. The Fourier transform shows week features. The first peak (ca. 2.6 Å) includes contributions from the first shell of the Ru metal phase. Above ca. 3 Å Ru-Ru interactions pertaining to Ru can be observed but only the

first shell coordination was fitted as the more distant shells could not be resolved for this sample.

3.3. Measurements of catalytic activity

3.3.1. Description of the reaction equipment

The catalytic activity measurements at 3.5 bar were conducted in a fixed bed reactor. This equipment has a gas supplier system and an analysis of products system by means of gas chromatography. The fixed bed reactor is a tube of stainless steel 316 L (47 cm long, 0.049" wall diameter and 3/8" outer diameter). The setup diagram is displayed in Figure 3.11. The gas flow rates were controlled using Bronkhorst High-Tech Series mass flow controllers. The reactor was held within a furnace equipped with a temperature controller. The reaction temperature was measured with a K-type thermocouple inserted directly in the catalytic bed as it is shown in Figure 3.12. The catalytic activity measurements at 15 bar were carried out in a six-flow fixed-bed microreactor setup (see Figure 3.13) which permitted running six reactions in parallel under identical feed composition, temperature, and conditions of separation/analysis following the experimental procedure described in detail elsewhere [34].

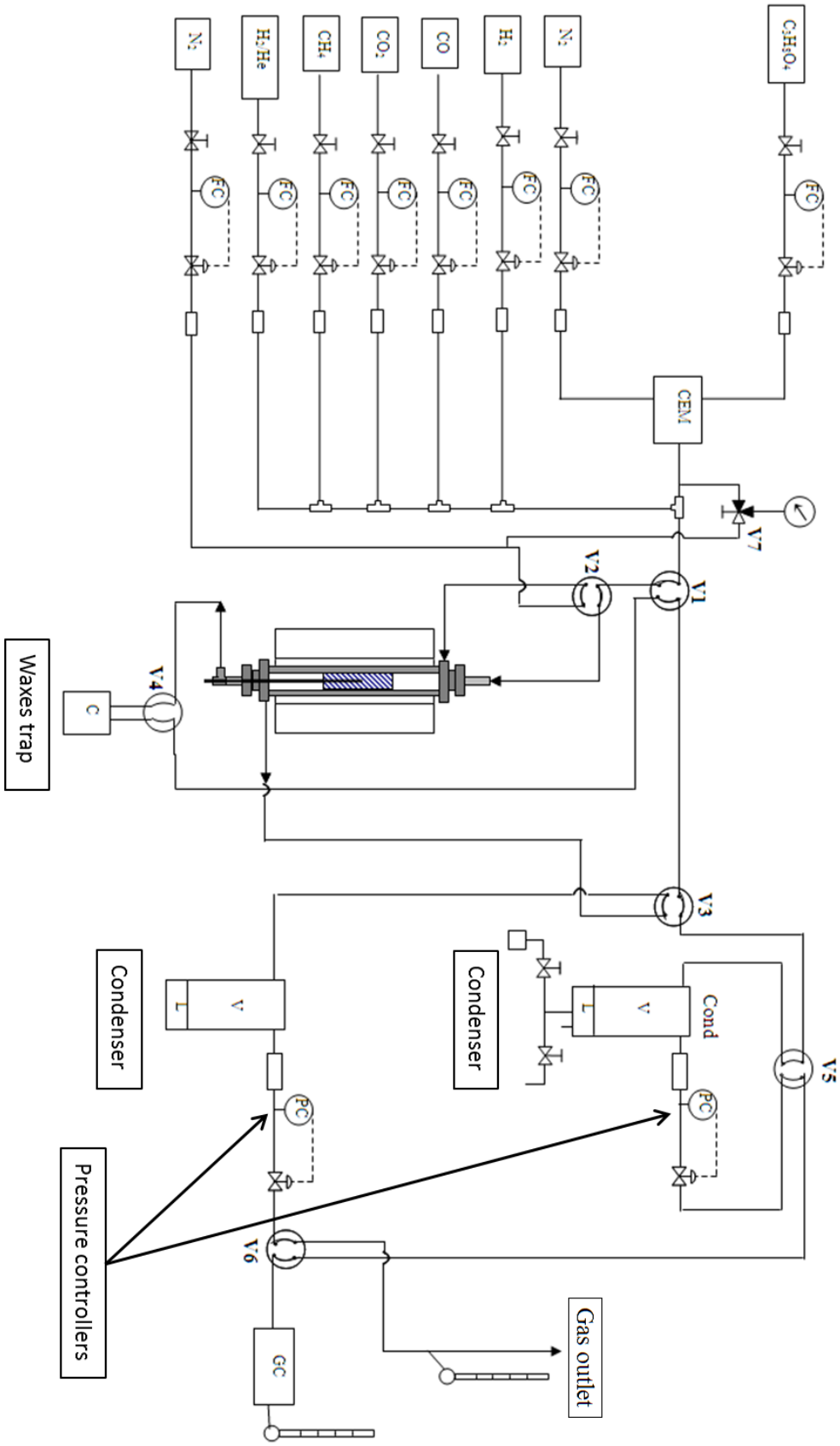

Figure 3.12. Detailed process flow scheme of the FTS setup (3.5 bar).

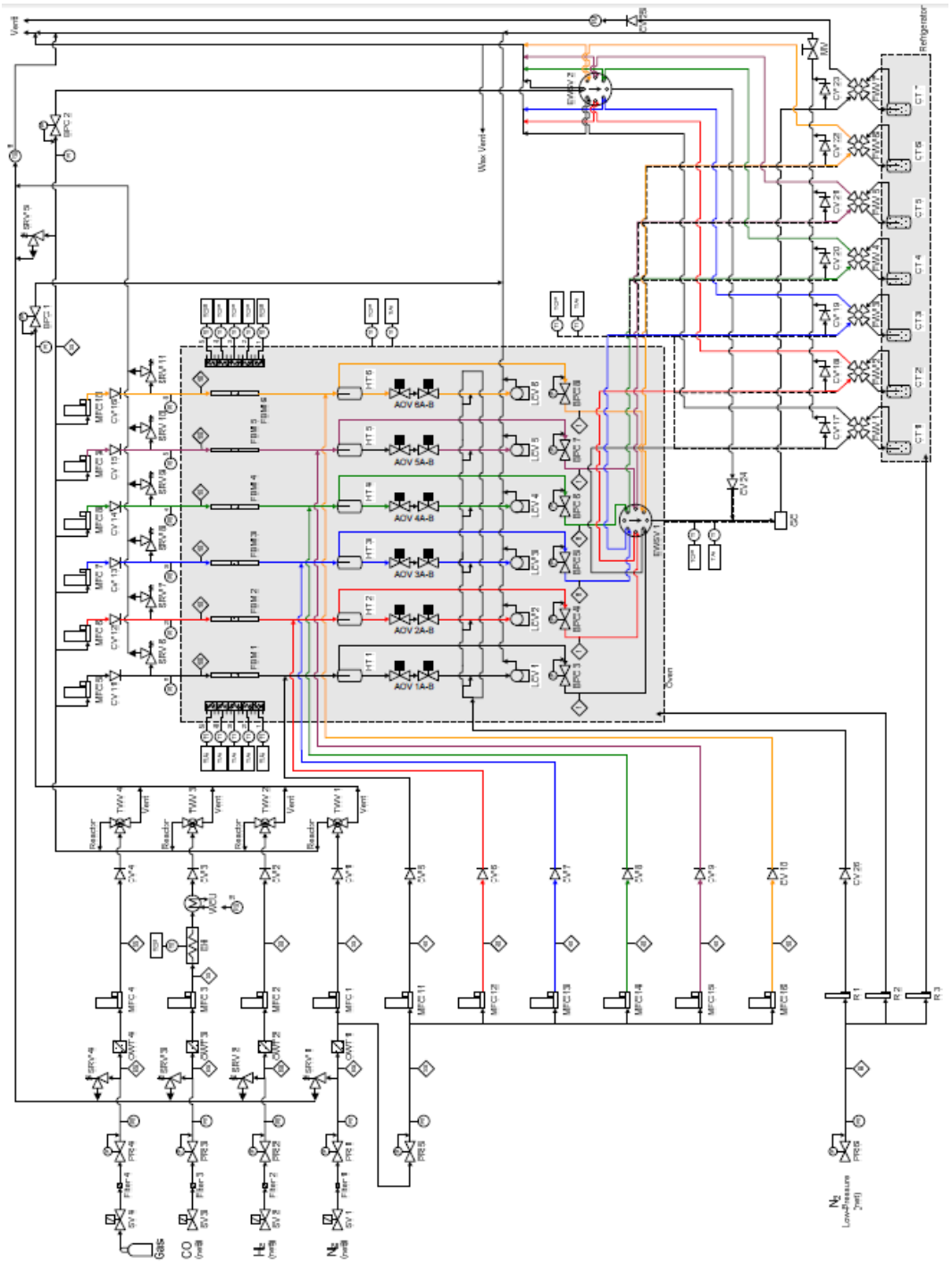

Figure 3.13. Detailed process flow scheme of the six-flow fixed-bed microreactor FTS setup (15 bar).

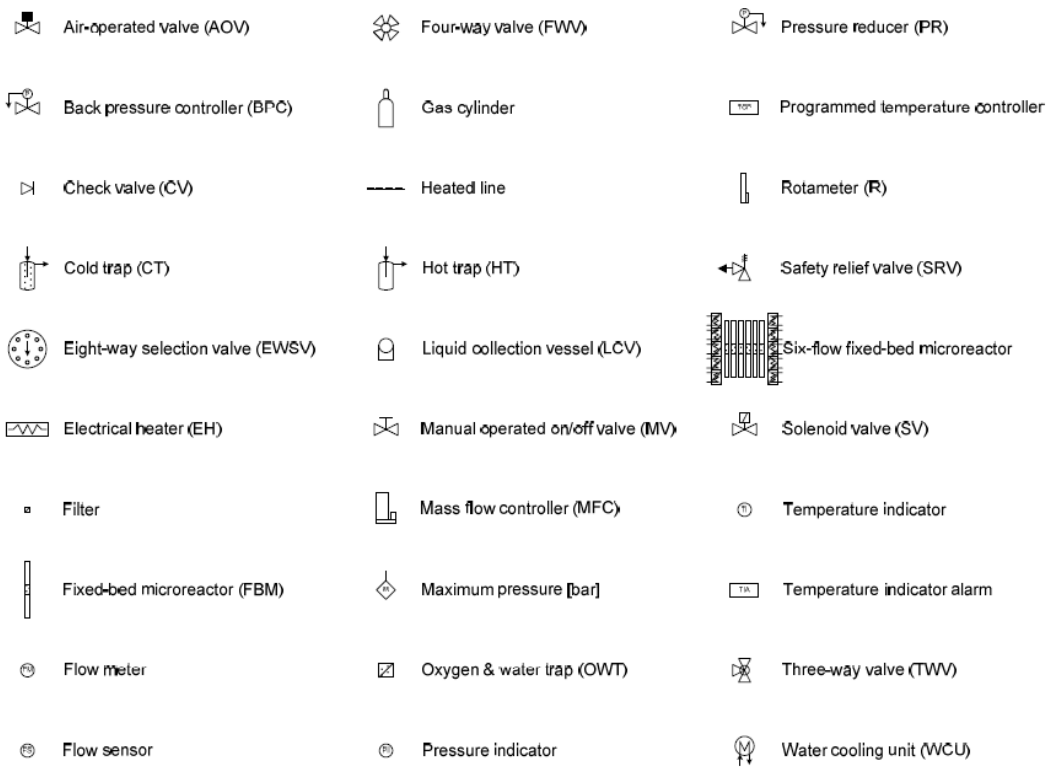

Figure 3.14. Description of the symbols and acronyms used in Figure 3.13.

3.3.2. Experimental methodology

3.3.2.1. Method of activity measurement in the fixed bed reactor

The reactor was filled with 500 mg of catalyst, and SiC was added to obtain 4 cm length. Prior to the catalytic test, the catalyst was reduced over 2 h with an H_2 flow at 400 °C, increasing the temperature at a rate of 5 °C / min. After reduction, the catalyst was cooled to the reaction temperature (240-250 °C). The Fischer-Tropsch reaction was performed at 15 bar with a H_2/CO mixture (2/1, flow rate of 50 mL/min) and at 3.5 bar with a CO/H_2/He mixture (1/2/6, flow rate of 45 mL/min). The outlet gas was analyzed online with a Bruker GC-450 gas chromatograph equipped with two thermal conductivity detectors for the analysis of permanent gases (H_2 and CO, CH_4, CO_2, respectively) and one flame ionization detector for C_1−C_9 hydrocarbon analysis (see figure 3.13). The reaction was run under differential conditions (CO conversions below 15%) to prevent the

occurrence of secondary reactions. The selectivity was calculated on a carbon basis.

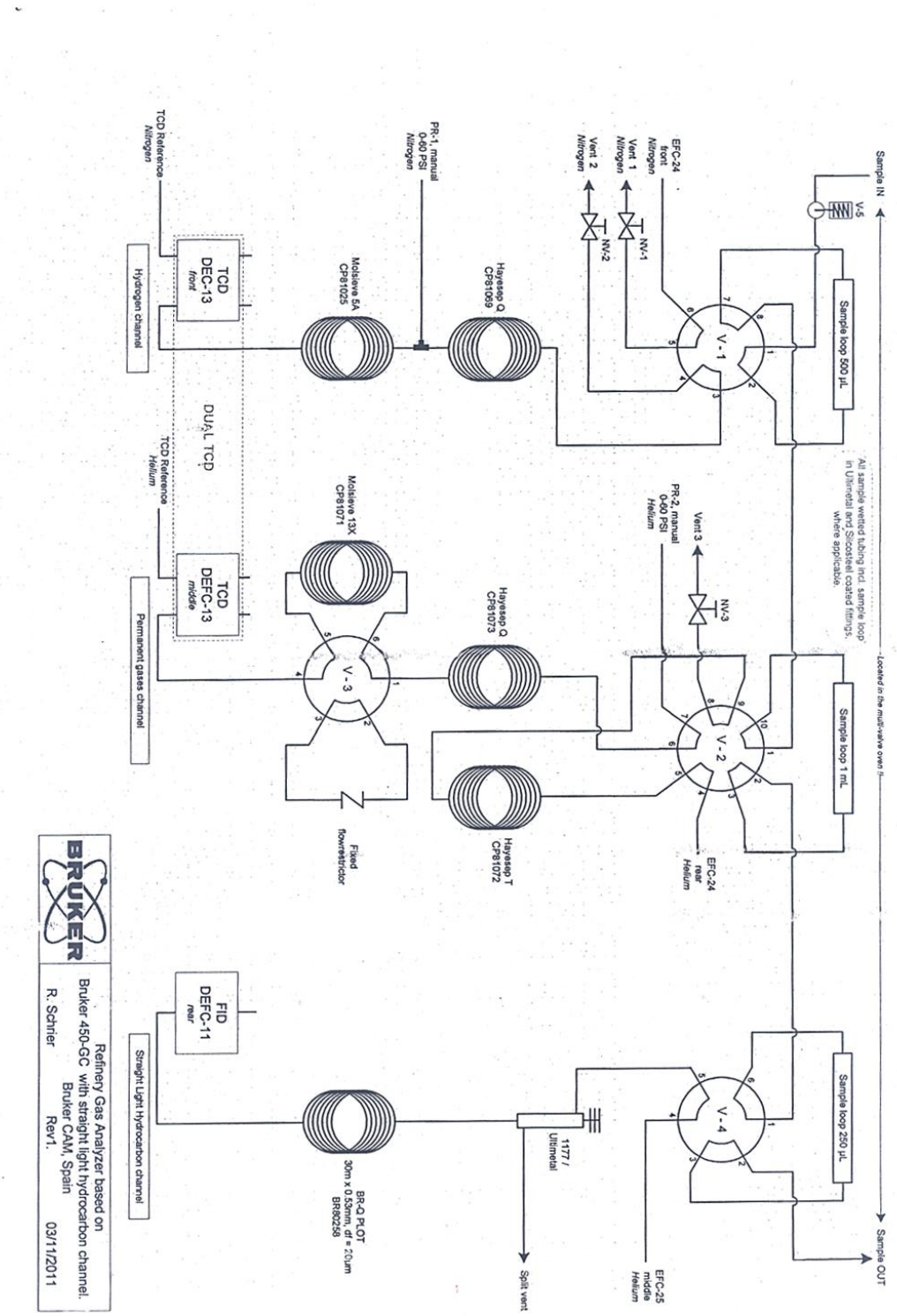

Figure 3.15. Scheme of Bruker GC-450 gas chromatograph.

3.3.2.2. Data analysis

The results obtained from the integration of the areas of the recorded peaks in the chromatogram are introduced in an Excel worksheet that was designed with the aim to obtain the kinetic parameters (conversion and selectivity) in a quick and easy way. CO conversion, carbon selectivity, molar fraction of each product were defined by Eqs. (3.9)-(3.11), where X_{CO} stands for CO conversion, F indicates the molar flow, S is the carbon selectivity towards a product with n carbon atoms and Y is the molar fraction of a hydrocarbon Cn.

$$X_{CO} = \frac{F_{in,CO} - F_{out,CO}}{F_{in,CO}} \cdot 100 \qquad \text{(equation 3.9)}$$

$$S_{Cn} = \frac{nF_{Cn}}{F_{CO_2} + \sum_{n=1}^{N} nF_{Cn}} \cdot 100 \qquad \text{(equation 3.10)}$$

$$Y_{Cn} = \frac{F_{Cn}}{\sum_{n=1}^{N} F_{Cn}} \cdot 100 \qquad \text{(equation 3.11)}$$

3.3.2.3. Other experimental considerations.

As has been mentioned in paragraph 3.3.2.1 of this Chapter, the catalyst bed is formed by the catalyst and a diluent material (inert). In a fixed bed reactor, local flows around the catalyst grains and along the walls of the reactor can cause a deviation from ideal piston flow. An accepted criterion [35] to neglect the effect of axial dispersion is given by the expression:

$$\frac{L_{CB}}{d_g} > 50 \qquad \text{(equation 3.12)}$$

Where L_{CB} is the catalyst bed length (40 mm) and d_g is the grain diameter (0.35-0.5 mm). In the experimental conditions employed, the result of this

coefficient varies approximately between 80 and 114, so the above criterion is achieved.

Furthermore, the reactor walls may also be the cause of a deviation from piston flow. The minimum diameter of the reactor is given by [35]:

$$\frac{d_r}{d_g} > 10 \qquad \text{(equation 3.13)}$$

Where d_r is the reactor diameter and d_g is the grain diameter. In this case, d_r/d_g varies between 14 and 20, so it can also rule out any reactor effect.

CO hydrogenation reaction is highly exothermic. The possibility of temperature gradients in the catalyst bed is minimized by both the use of inert materials such as graphite, quartz or glass wool and silicon carbide (SiC) and a diluted CO:H_2:He (1:2:6) mixture.

3.4. References

[1] R. Klockenkämper, *Total reflection X Ray Fluorescence Analysis*, Wiley, New York (1997).

[2] R. Fernández-Ruiz, M. Furio, F. Cabello Galisteo, C. Larese, M. L. Granados, R. Mariscal, J. L. G. Fierro, *Anal. Chem*. 74 (2002) 5463-5469.

[3] R. Fernández-Ruiz, F. C. Galisteo, C. Larese, M. L. Granados, R. Mariscal, J. L. G. Fierro, *Analyst*, 131 (2006) 590-594.

[4] T. Magalhães, A. von Bohlen, M. L. Carvalho, M. Becker, *Spectrochim. Acta, Part B*, 61 (2006) 1185-1193.

[5] R. Fernández-Ruiz, J. D. Tornero, V. M. González, C. Alonso, *Analyst*, 124 (1999) 583-585.

[6] M. González, L. Tapia, M. Alvarado, J. D. Tornero, R. Fernández-Ruiz, *J. Anal. At. Spectrom*. 14 (1999) 885-888.

[7] R. Fernández-Ruiz, J. Capmany, *J. Anal. At. Spectrom*. 16 (2001) 867–869.

[8] M. Krämer, A. von Bohlen, C. Sternemann, M. Paulus, R. Hergenröder, *Appl. Surf. Sci.* 253 (2007) 3533–3542.

[9] R. Fernández-Ruiz, J. P. Cabañero, E. Hernández, M. León, *Analyst*, 124 (2001) 583-585.

[10] F. Cariati, P. Fermo, S. Gilardoni, A. Galli and M. Milazzo, *Spectrochim. Acta, Part B*, 58 (2003) 177-184.

[11] R. Fernández-Ruiz, M. Garcia-Heras, *Spectrochim. Acta, Part B*, 63 (2008) 975-979.

[12] M. García-Heras, M. J. Blackman, R. Fernandez-Ruiz, R. L. Bishop, *Archaeometry*, 43(3) (2001) 325-347.

[13] R. Fernández-Ruíz, P. Ocon, M. Montiel, *J. Anal. Atom. Spectrom.* 24 (2009) 785-791.

[14] S. Brunauer, P. H. Emmett, E. Teller, *J. Am. Chem. Soc*. 60 (1938) 309-319.

[15] K. S. W. Sing, D. H. Everett, R. A. W. Haul, L. Moscou, R. A. Pierotti, J. Rouquerol,T. Siemieniewska, *Pure Appl.* Chem. 57 (1985) 603-619.

[16] R. Jenkins, R. L. Snyder, *Diffraction Theory* (1996) pp. 47-95.

[17] P. Scherrer, *Göttinger Nachrichten Gesell*, 2 (1918) 98.

[18] A. Patterson, *Phys. Rev*. 56(10) (1939) 978-982

[19] Y. Otake, R. G. Jenkins, *Carbon*, 31 (1993) 109.

[20] P. Arnoldy, J. A. Moulijn, *J. Catal.* 93 (1985) 38.

[21] J. B. Donnet. *Carbon*, 6 (1968) 161.

[22] D. M. Nevskaia, A. Santianes, V. Muñoz, A. Guerrero-Ruíz, *Carbon*, 37 (1999) 1065.

[23] J. R. Anderson, In *Structure of Metallic Catalysts*; Academic Press: London (1975) pp 289-394.

[24] A. Maroto-Valiente, I. Rodríguez-Ramos, A. Guerrero-Ruiz, *Thermochim. Acta*, 379 (2001) 195.

[25] D. B. Williams, C. B. Carter, Transmission Electron Microscopy I, Basics, New York (1996).

[26] P. Gallezot, C. Leclercq, In *Physical Techniques for Solid Materials. Fundamental and Applied Catalysis*, B. Imelik, J. C. Vedrine, Eds, Plenum Press: New York (1994) pp. 509.

[27] A. Borodziński, M. Bonarowska, *Langmuir*, 13 (1997) 5613.

[28] C. D. Wagner, L. E. Davis, M. V. Zeller, J. A. Taylor, R. H. Raymond, L. H. Gale, *Surf. Interface Anal*. 3 (1981) 211-225.

[29] M. Fernández-García, C. Márquez, G. L. Haller, J. Phys. Chem. 99 (1995) 12565.

[30] E. R. Malinoswky, Factor Analysis in Chemistry; Wiley: New York (2002).

[31] M. Fernández-García, Catal. Rev.-Sci. Eng. 44 (2002) 59-121.

[32] K. V. Klementiev, *J. Phys. D: Appl. Phys.* 34 (2001) 209-17.

[33] J. J. Rehr, J. J. Kas, F. D. Vila, M. P. Prange, K. Jorissen, *Phys. Chem. Chem. Phys.* 12 (2010) 5503-5513.

[34] S. Sartipi, K. Parashar, M.J. Valero-Romero, V.P. Santos, B. van der Linden, M. Makkee, F. Kapteijn, J. Gascon, J. Catal. 305 (2013) 179.

[35] J. Pérez-Ramírez, R.J. Berger, G. Mul, F. Kapteijn, J.A. Moulijn, *Catal. Today*, 60 (2000) 93-109.

Chapter 4

Time-Resolved XAS Investigation of the Local Environment and Evolution of Oxidation States of a Fischer-Tropsch Ru-Cs/C Catalyst

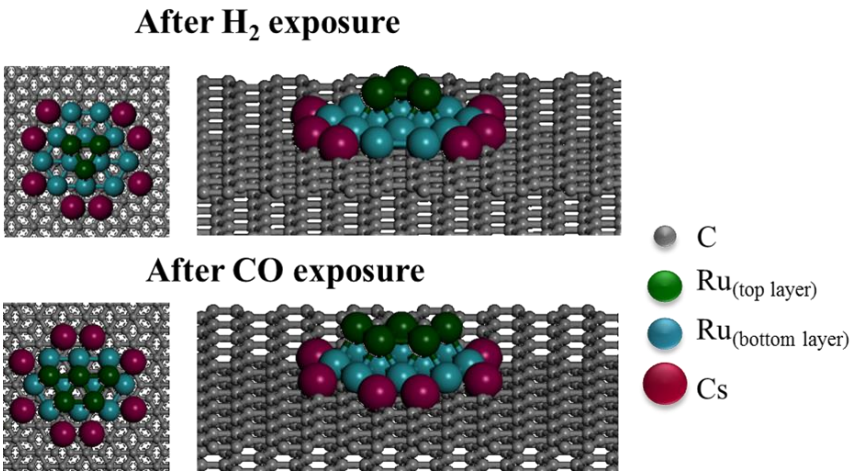

This Chapter is based on the following publication:

J. L. Eslava et al. *ACS Catal*, 2016, 6, 1437.

Here we present a time-resolved in situ X-ray absorption spectroscopy investigation of the local chemical environment and the electronic structure of the active metal (Ru) and the promoter (Cs) present in catalysts supported over high-surface-area graphite. These catalysts were submitted to a reduction treatment under hydrogen gas and then to alternate atmospheres of Fischer-Tropsch reactants, CO/He, and H_2/He atmospheres, respectively. This study reveals that Ru reduction is a complex process taking place through a two-step mechanism via an intermediate oxidation state and occurs in parallel to the Cs partial reduction. It also demonstrates a close association between Cs and Ru atoms as first neighbors. The evidence that the Ru-Cs particle morphology reverses (from flat 2D to a 3D shape with low coordination numbers) when the H_2 atmosphere is changed with CO proves the strong interaction of CO with the surface of the Ru-Cs nanoparticles, a point confirmed by microcalorimetry of CO adsorption. To our knowledge, this is the first time that this reversible particle reconstruction upon syngas reactant switching has been demonstrated.

4.1 Results and Discussion

Main Characteristics of Catalysts. Table 4.1 summarizes the chemical composition, CO uptake, and average metal particle sized as calculated from CO chemisorption (d_{CO}) and TEM (d_{TEM}) of the catalysts after reduction in hydrogen at 400 ºC for 2 h.

Table 4.1. Main characteristics of the ruthenium catalysts reduced in hydrogen at 400 ºC for 2 h.

Catalyst	Ru (wt%)	Cs (wt%)	CO uptake ($\mu mol/g_{Ru}$)	d_{CO} (nm)	d_{TEM} (nm)
4Ru/G	3.63	-	98	4.5	1.7
4Ru4Cs/G	3.57	3.38	98	4.8	2.3
4Cs/G	-	3.67	-	-	-

Figure 4.1 shows the TPR profiles of the ruthenium samples. The 4Ru/G catalyst shows one peak of hydrogen consumption centered at 180 ºC that can be assigned to the reduction of Ru (III) to Ru(0) species [1]. For the promoted catalyst (RuCs/G sample) the temperature of ruthenium reduction shifts to higher temperatures and the peak seems to be wider. This fact indicates a close interaction between the metal and promoter salts. The lower interaction of the precursor salts with the surface of the carbon support favors the interaction between themselves [2].

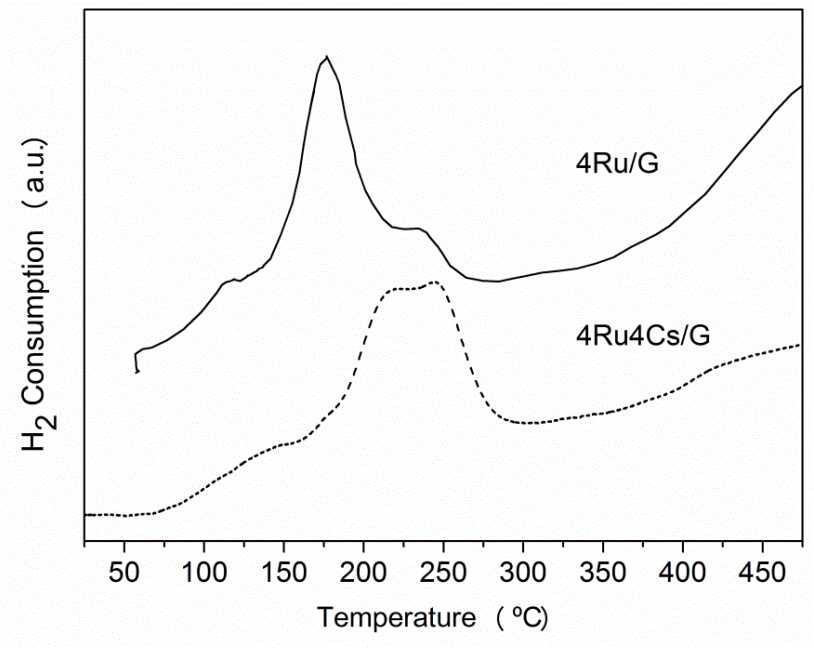

Figure 4.1. Hydrogen consumption profiles during temperature-programmed reduction for the ruthenium catalysts: (solid line) 4Ru/G; (dotted line) 4Ru4Cs/G.

The microcalorimetric determinations of the CO adsorption on the samples reduced at 400 ºC evidenced an increase in the heat of CO adsorption when the promoter was added. Figure 4.2 shows the differential enthalpies of CO adsorption (Q_{diff}) as a function of coverage degree for the 4Ru/G and 4Ru4Cs/G catalysts. The profile for 4Ru/G catalyst exhibits a high initial adsorption heat of 140 kJ/mol. This high value is typical of highly energetic active sites usually associated with small ruthenium nanoparticles, which preferentially populate edges, corners and other metallic (Ru) low-coordinated sites. This initial adsorption heat quickly decreases to reach a constant value of 105 kJ/mol for surface coverage from 0.1-0.2 to 0.8 and finally drops down to 40 kJ/mol (physisorption values). In contrast, for the Cs-promoted sample the absence of surface Ru sites is observed with adsorption heats higher than 120 kJ/mol. This fact suggests that these highly reactive Ru atoms are likely interacting with the Cs ions, which modifies their adsorption properties. Thus, the Cs-promoted catalyst

has a rather more homogeneous energetic surface site distribution in comparison to the nonpromoted Ru catalyst. In addition, for nearly the whole range of surface coverage, from 0.1 to 0.8, the heats of CO adsorption are higher than those for the nonpromoted Ru catalyst, revealing the presence of stronger surface sites for CO adsorption on the Cs-promoted Ru catalyst. This can be interpreted by considering an increase in the electron density of the surface ruthenium atoms. As introduced above, in accord with certain authors [3, 4, 5], cesium would act as an electronic promoter, donating part of its electron density to Ru. This electron donation may take place with oxidized cesium (cesium hydroxide, oxide, or superoxide), although charge transfer to Ru would be more effective if cesium were full or partially reduced. In this way, the contribution of the Ru-C π bond would be greater (via larger π back-donation from the metal atoms to antibonding molecular orbitals of the CO molecule) and thus higher heats of CO adsorption would be attained.

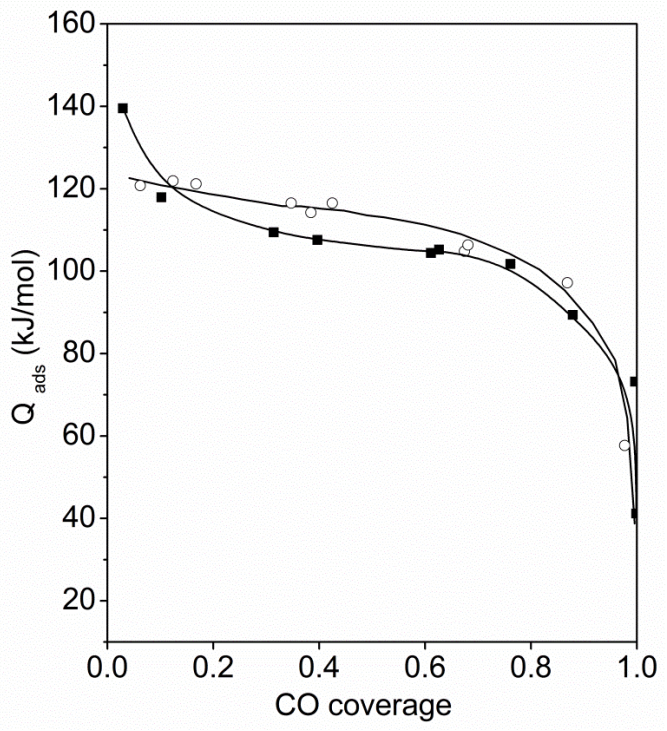

Figure 4.2. Differential heats of CO adsorption at 58 ºC as a function of surface coverage for (■) 4Ru/G and (○) 4Ru4Cs/G catalysts.

Table 4.1 summarizes the CO uptakes and the average metal particle sizes calculated from both CO chemisorption and TEM determinations for the nonpromoted and Cs-promoted ruthenium catalysts. The particle sizes determined by TEM are smaller than particle sizes obtained by CO chemisorption, whatever the catalyst composition. These discrepancies between the d_{CO} and the d_{TEM} values can be interpreted as being due to an adsorption stoichiometry of CO over Ru involving more than one Ru surface atom per chemisorbed CO molecule. In addition, the presence of chloride species in the catalyst (likely adsorbed on the metal particles) has been reported to impede the CO chemisorption on the surface metal sites. Residual chloride species can still persist in the surface of the catalysts after reduction under hydrogen at 400 °C [6, 7]. In our case, the presence of

residual chlorine was tested using XPS and was not detected. A surface content below the XPS detection limit, ca. 0.5 atom %, can be thus envisaged.

A comparison of catalysts shows that the Cs added to the ruthenium catalyst slightly increases the ruthenium particle size with respect to that of the nonpromoted 4Ru/G catalyst. From TEM images, similar particle size distributions (histograms in 4.3) are observed independently of the presence or absence of cesium, with the majority of ruthenium nanoparticles having sizes between 0.5 and 1.5 nm.

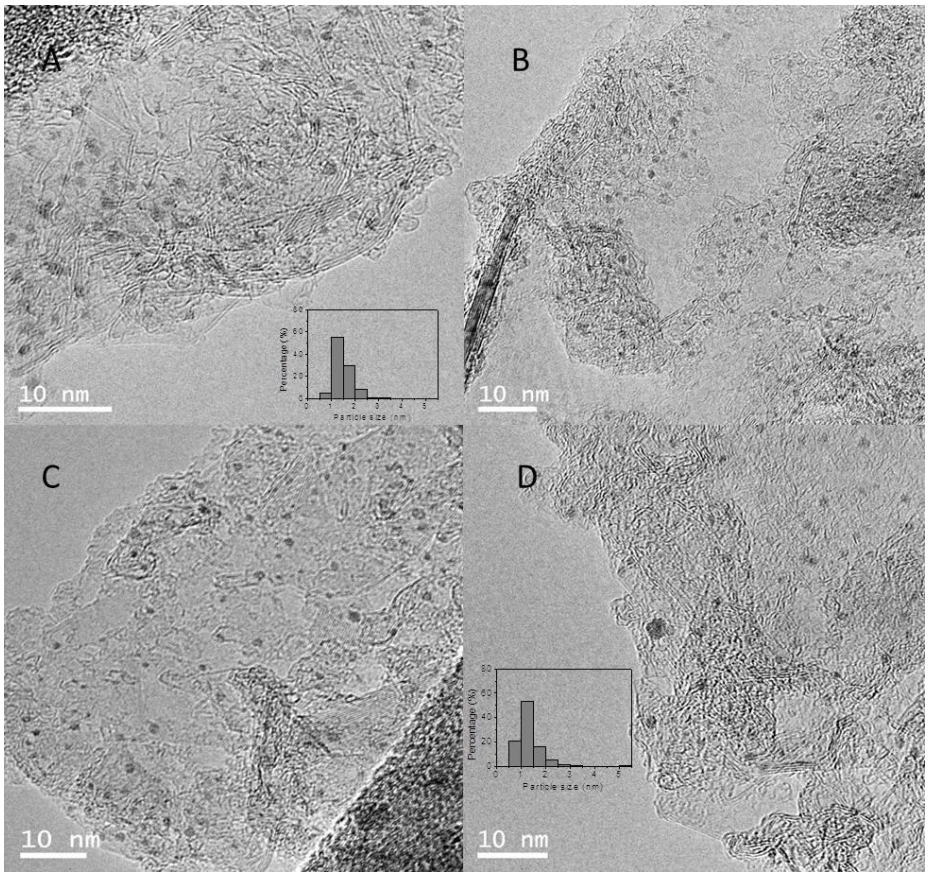

Figure 4.3. HRTEM micrographs for (A and B) 4Ru/G and (C and D) 4Ru4Cs/G catalysts reduced at 400 ºC. Insets show the histograms with the particle size distribution.

XANES. The evolution of the Ru and Cs species during the temperature-programmed reduction on the catalysts was investigated by XANES. Figure 4.4 presents the set of Ru K edge XANES spectra recorded as a function of temperature for the two catalysts.

The Ru K-edge XANES spectra evolve gradually with temperature in the two samples. Particularly above 120-150 °C, the absorption edge shifts toward lower energies and the wide and prominent first resonance (white line) becomes depleted, leading to a spectrum similar to that of Ru^0. The sets of XANES were examined by principal component analysis (PCA) to interpret the reduction process [8, 9]. PCA enables determination of the number of Ru chemical species that are involved in the H_2 treatment and quantification of their corresponding evolutions throughout the temperature.

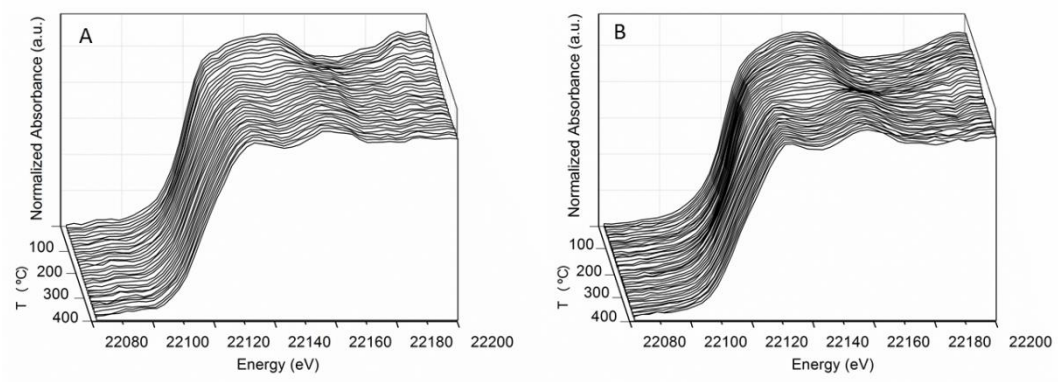

Figure 4.4. Ru K-edge XANES spectra collected at different temperatures during reduction. (A) 4Ru/G; (B) 4Ru4Cs/G.

The statistical analysis is described in the experimental section (3.2.10) and was applied to Tables 4.2 and 4.3 for the set of XANES spectra obtained for the 4Ru/G and 4Ru4Cs/G samples, respectively. A sharp increase of %SL level between the second (4Ru/G; Table 4.2) and third (4Ru4Cs/G; Table 4.3) eigenvalues and the subsequent value was observed.

Table 4.2. Principal Component Analysis for the 4Ru/G sample

n	eigenvalue	REV	IND	variance	%SL
1	.91675D+03	.166E+04	.404E-04	99.940	.00
2	.52203D+00	.733E+02	.960E-05	99.997	.00
3	.66947D-02	157E+01	.928E-05	99.998	8.42
4	.40055D-02	133E+01	.932E-05	99.999	13.49
5	.28143D-02	.117E+01	.957E-05	99.999	16.91
6	.22347D-02	.126E+01	.106E-04	99.999	18.08
7	.13980D-02	.126E+01	.106E-04	99.999	25.81
8	.10273D-02	.102E+01	.117E-04	99.999	30.90
9	.92898D-03	.118E+01	.129E-04	99.999	31.10
10	.72136D-03	.105E+01	.146E-04	100.000	35.33
11	.62273D-03	.919E+00	.168E-04	100.000	37.23
12	.61222D-03	.100E+01	.195E-04	100.000	35.79

Table 4.3. Principal Component Analysis for the 4Ru4Cs/G sample

n	eigenvalue	REV	IND	variance	%SL
1	.92721D+03	.949E+03	.491E-04	99.981	.00
2	.92297D+00	.149E+02	.161E-04	99.991	.00
3	.58226D-01	.583E+01	.102E-04	99.997	0.3
4	.93965D-02	.174E+01	.938E-05	99.998	5.50
5	.50608D-02	.154E+01	.907E-05	99.999	8.56
6	.30818D-02	179E+01	.909E-05	99.999	13.02
7	.16039D-02	.118E+01	.964E-05	99.999	23.91
8	.12611D-02	.110E+01	.104E-04	99.999	26.91
9	.10580D-02	.116E+01	.113E-04	99.999	28.58
10	.83605D-03	.101E+01	.126E-04	99.999	32.04
11	.75482D-03	.128E+01	.141E-04	100.000	32.30
12	.53813D-03	.913E+00	.163E-04	100.000	38.86

Thus, this indicates two and three Ru chemical species in the samples 4Ru/G and 4Ru4Cs/G, respectively, during the H_2 treatment. Figure 4.5 presents the XANES spectra and the concentration profiles of the pure chemical species of Ru observed along the H_2-TPR experiments.

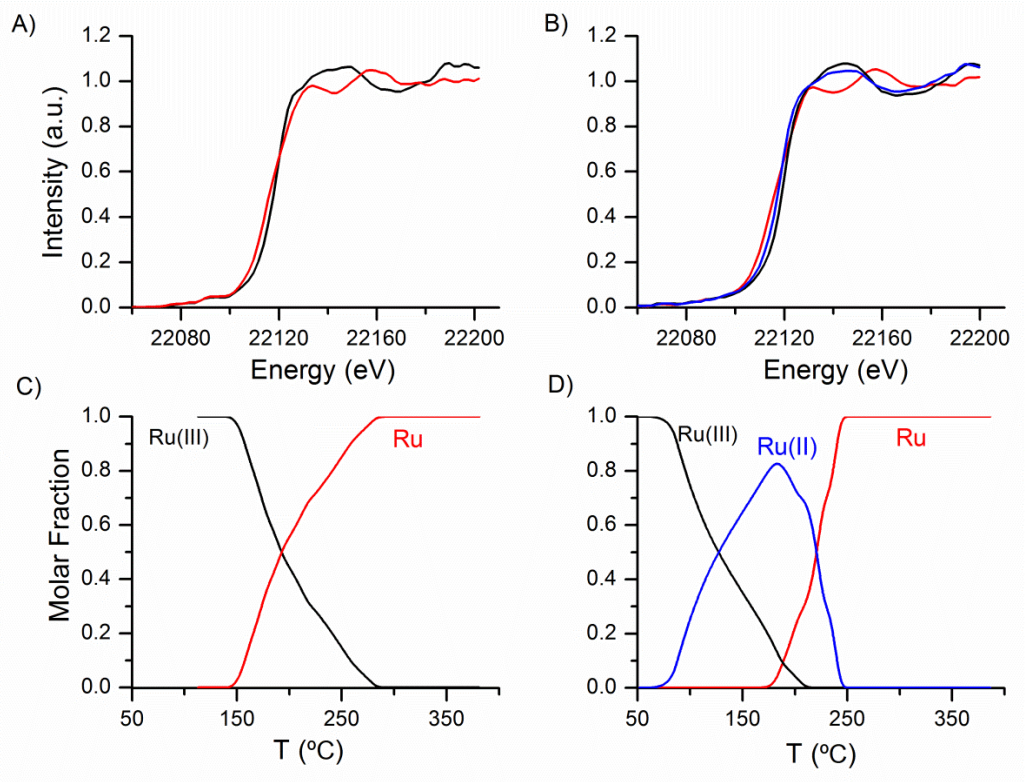

Figure 4.5. Ru K-edge XANES spectra and concentration evolution of the pure chemical species present along H_2-TPR until 400 ºC for 4Ru/G (A, C) and 4Ru4Cs/G (B, D) catalysts. Results were obtained by PCA.

In the case of the 4Ru/G catalyst, the reduction starts at approximately 150 °C and occurs progressively in one step up to 250 °C. Conversely, the reduction of the 4Ru4Cs/G catalyst is a more complex process, occurring in two stages with the detection of an intermediate component.

As the line shape of the derivative function is less sensitive to size/shape than is the corresponding XANES function, it was used (see Figure 4.6) to verify that two of the pure species show features (raising edges as well as shapes) very similar to those corresponding to reference compounds: hcc Ru(0) foil and the Ru(III) precursor (having P3c1 space group symmetry), respectively. The existence of the metallic phase is also shown by the EXAFS signal analysis,

which corroborates a Ru-Ru contribution at characteristic bonding distances of the metallic Ru(0) (ca. 2.6 Å; see EXAFS analysis below). The assignment of the intermediate species is more complex (in blue in Figure 4.5.b,d), as there was no suitable XANES reference. However, it can be seen that the edge derivative is close to but is shifted to lower energies than that of the trivalent reference (Figure 4.6.).

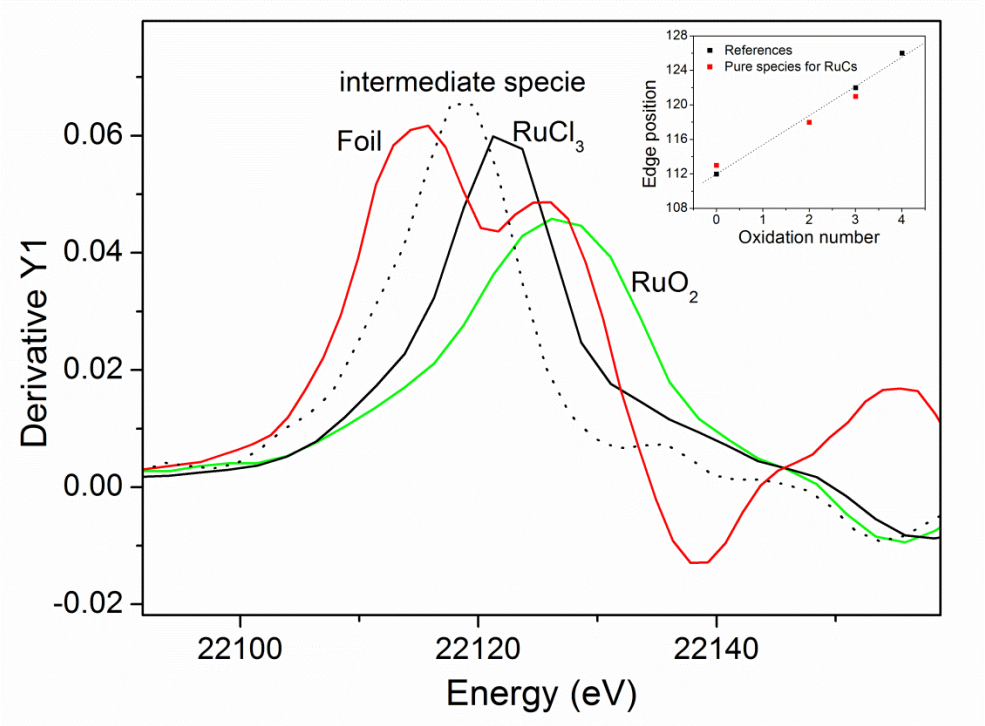

Figure 4.6. XANES derivative spectra of RuO_2, $RuCl_3$ and Ru foil reference materials (solid lines) and second Ru pure chemical species from FA for 4Ru4Cs/G (dotted lines). The derivative maximum position versus oxidation state is presented in the inset.

The analysis of the maximum of the first derivative (inset in Figure 4.6) suggests an oxidic chemical species typical of Ru(II). No suitable XANES spectra of known Ru(II) oxide type reference are available. Nevertheless, we can conclude

that the new species has a XANES spectrum that is clearly different from that attributed to Ru metallic or Ru(IV) and Ru(I) oxidic species.

Thus, for the 4Rh4Cs/G catalyst, the Ru(III) species of the salt precursor is reduced to Ru(II) between 75 and 175 °C. The full reduction to Ru metallic starts around 175 °C, before the Ru(III) has been completely extinct, and takes place up to 250 °C. It is clear that the presence of the Cs promoter modifies the reduction process of Ru. Although the full reduction to Ru metal is achieved approximately at the same temperature for promoted and nonpromoted catalysts, the formation of an intermediate Ru oxidized species at low temperatures for the sample 4Ru4Cs/G suggests a modification of the electronic properties of Ru entities via interaction with the Cs atoms.

The Cs L_1 edge XANES spectra recorded during the temperature-programmed reduction for the promoted catalyst (4Ru4Cs/G) are reported in Figure 4.7. It can be noticed that the nonreduced 4Ru4Cs/G sample gives rise to a sharp feature at approximately 5712 eV. During the reduction treatment in hydrogen a decreasing intensity of the white line and a shift of the absorption edge toward lower energies are observed. The net shift after reduction at 400 °C is around 0.68 eV. Such a shift is significant, because at these energies the intrinsic monochromator resolution is ca. $(\Delta E/E)_{intr} = 1.35 \times 10^{-4}$. In addition, the inset in Figure 4.7 shows that the severe decrease in the white line intensity, attributed to an increase of the d state electron density involved in the 2s-3d resonance transition, occurs at around 175 °C. This latter value, as discussed above, is the temperature at which the Ru metal starts to be formed (Figure 4.5). In contrast, for the Ru-free Cs blank sample, XANES spectra with equal edge shape and with

identical absorption edge energy values were observed during temperature-programmed reduction treatment in hydrogen (see Figure 4.8.).

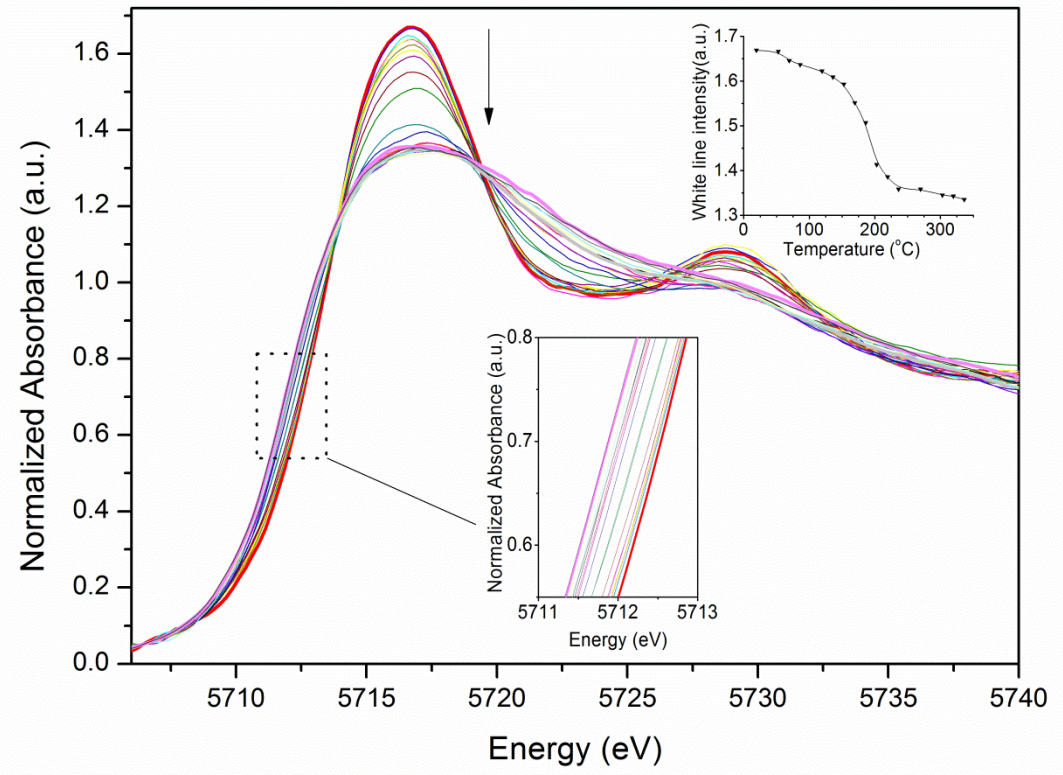

Figure 4.7. Cs L_1-edge XANES spectra collected during temperature-programmed reduction in hydrogen and inset showing an enlargement of their absorption edges at the inflection point for the 4Ru4Cs/G catalyst. The other inset shows the variation of the white line intensity with the temperature.

We can conclude that while in the absence of Ru (Cs/G sample) no variation in the oxidation state can be inferred, in the presence of Ru (4Ru4Cs/G catalyst) at least partial Cs reduction can be deduced after H_2 treatment at 400 °C. It is likely that the partial reduction of Cs can be brought about by H species coming from the dissociative chemisorption of H_2 on Ru. These results support the recent in situ XAS study of Rossetti et al. [5] concerning the electronic state of Cs in carbon-supported Cs-Ru catalysts, where partial reduction of Cs was observed.

However, our XANES study goes further because we have studied the Ru K edge in parallel, being able to directly relate the appearance of metallic Ru to the partial reduction of Cs.

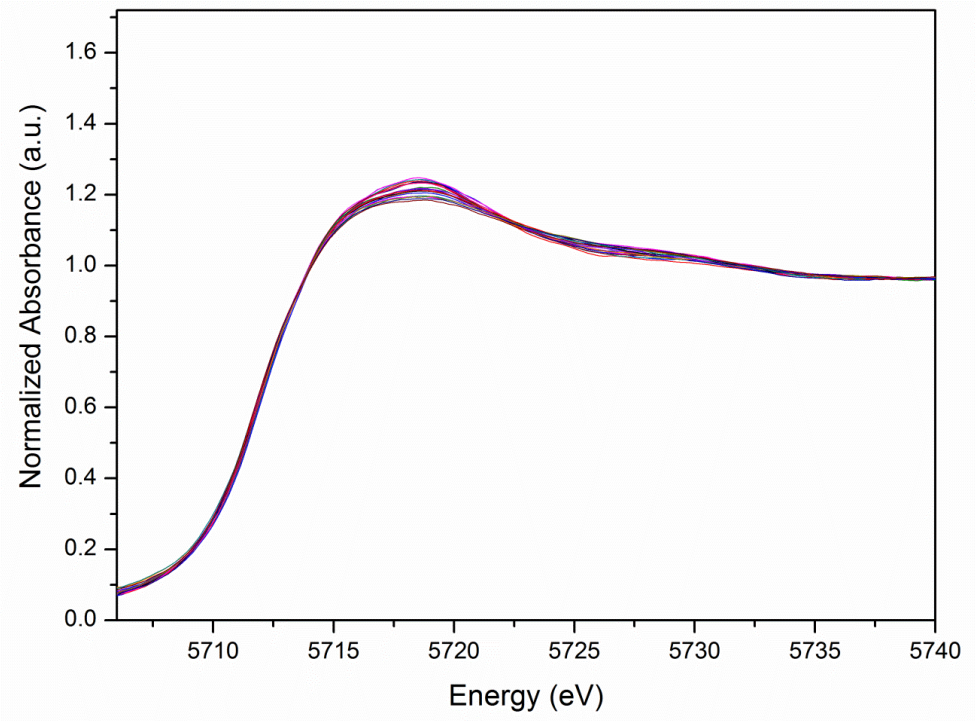

Figure 4.8. XANES spectra at Cs L_1-edge collected during temperature programmed reduction in hydrogen for blank 4Cs/G sample.

EXAFS. After completion of the reduction treatment at 400 °C, the temperature was decreased to the reaction temperature, 250 °C. Subsequently, cyclic experiments switching from H_2 to CO with a 60 s exposure to each gas were carried out in order to examine the interaction of Ru active centers with both Fischer-Tropsch reactants. Therefore, time-resolved EXAFS spectra at the Ru K edge were recorded during the switching of gases. The 4Ru/G catalyst gives a low-intensity EXAFS signal which Fourier transform shows to be only the peak corresponding to the nearest neighbors in the first coordination shell. Comparison with the Ru foil reference (Figure 4.9) suggests the presence of very small

nanoparticles of metallic Ru. Only the first-shell coordination was fitted, as the more distant shells could not be resolved. Fitting data confirm a Ru-Ru distance close to the foil (2.63-2.64 Å) and coordination number of around 2.4 (Table 4.4).

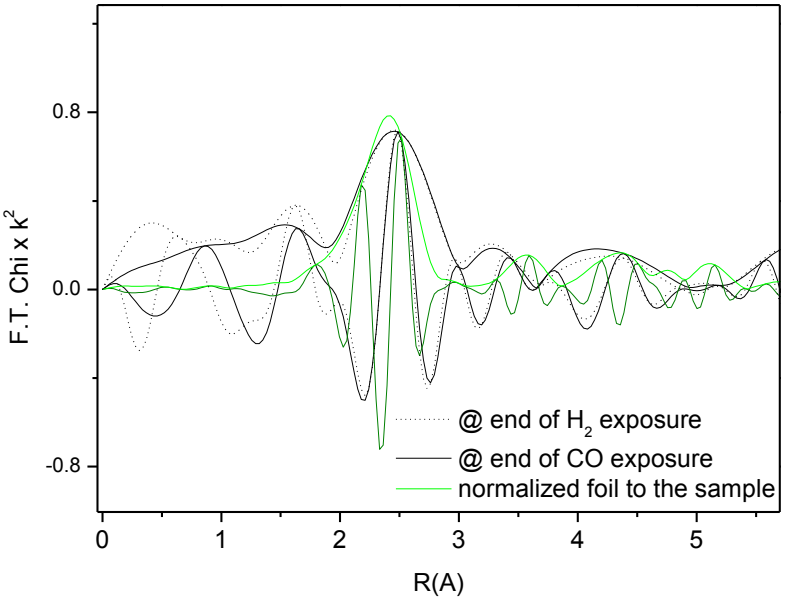

Figure 4.9. Ru K-edge EXAFS k^2-weighted Fourier transforms for reduced 4Ru/G catalyst during H_2-CO cycling experiments in: hydrogen (dotted lines) and CO (solid lines) atmospheres. EXAFS data of Ru foil normalized to the sample are shown in green as reference.

Table 4.4. Structural parameters derived from analysis of the EXAFS data in Fig. 4.9 for 4Ru/G catalyst.

		1st Ru-Ru
H_2	*R*	2.63
	N	2.38
CO	*R*	2.64
	N	2.47

These results indicate the presence of small Ru(0) nanoparticles with average particle sizes of around 1 nm in which the number of surface undercoordinated atoms is highly significant. The observed differences from the TEM average particle size (see Table 4.1) can be attributed to microscopy limitations for measuring metal particle sizes below 1 nm [10]. Moreover, in contrast to XAS studies of carbon-supported cobalt catalysts where cobalt particle reconstruction under FT reaction conditions was reported [11], for the 4Ru/G catalyst neither structural nor electronic changes are observed upon alternation in the gas atmosphere during cyclic experiments.

EXAFS data analysis of the 4Ru4Cs/G catalyst (Figure 4.10. and Table 4.5) shows a quite different situation. Comparison of the catalyst in both gas atmospheres (H_2 or CO) with the Ru foil clearly reveals the presence of a Ru(0) phase in both cases. However, a new feature around 3 Å corresponding to a coordination shell absent in the reference is observed. The manifest interaction between both elements, promoter and Ru (shown by the XANES analysis discussed above), points out that this additional peak in the radial distribution is due to the presence of heavy atoms (Cs) in the close vicinity of Ru entities. Another noteworthy detail is the fact that no feature stemming from Ru neighbors in the second coordination shell is observed (around 3.5 Å) with H_2 exposure.

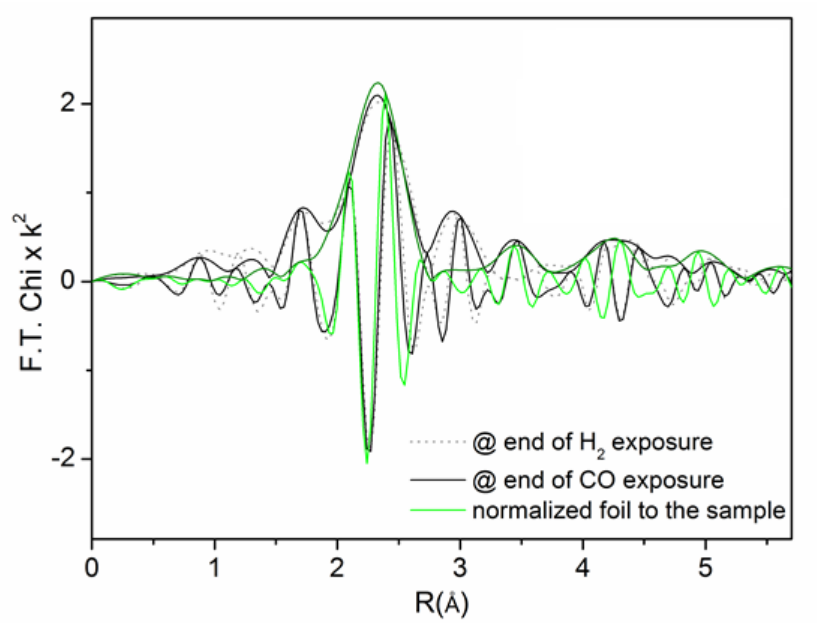

Figure 4.10. K^2-weighted modulus and imaginary part of the Fourier transform of Ru K-edge EXAFS spectra corresponding to the reduced 4Ru4Cs/G catalyst during H_2-CO cycling experiments: (dotted lines) hydrogen atmosphere; (solid lines) CO atmosphere. The (normalized to the sample) Fourier transform of the Ru foil is shown in green as a reference.

Coordination numbers obtained from the EXAFS analysis provide an indication of the Ru particle size, and Table 4.5 summarizes the coordination numbers. The value near 5 for the first Ru-Ru shell indicates Ru nanoparticles with an average size of around 1 nm. It is necessary to introduce another coordination shell, namely RuCs, at close distances from the Ru-Ru first shell (R = 3 Å) to obtain a good fit to the data. Moreover, the near-absence of the second Ru-Ru coordination shell (coordination number <0.6) in H_2 suggests a particle morphology resembling a single-layer, (111)-oriented, flatlike structure. However, when the H_2 atmosphere is switched to CO, the appearance of Ru neighbors in the second shell implies some restructuring of the nanoparticles. Figure 4.11 shows

the time evolution of the radial distribution for all EXAFS spectra during a whole H_2-CO cycle. The appearance and gradual increase of the Ru-Ru second shell with the time of CO exposure are evident. This phenomenon is entirely reversible, as it has been observed during cycles of alternate H_2/CO exposure.

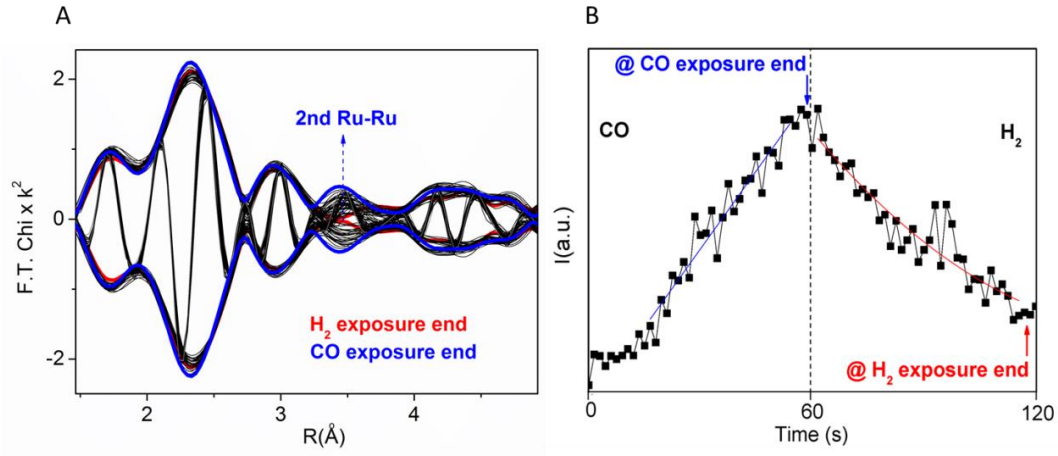

Figure 4.11. A) Modulus and imaginary part of the Fourier transform of EXAFS spectra obtained during a H_2 to CO switch. B) Second Ru-Ru coordination shell time evolution during one CO-H_2 cycle for the 4Ru4Cs/G catalyst.

Table 4.5. Structural Parameters Derived from Analysis of the EXAFS Data in Figure 4.10 for 4Ru4Cs/G Catalyst under H_2 and CO Exposure.

		first Ru-Ru	second Ru-Ru	Ru-Cs
H_2	R (Å)	2.64	3.52	3.04
	N[a]	4.74 (4.3)	0.60 (0.6)	1.13
CO	R (Å)	2.63	3.58	3.1
	N[a]	5.02 (5.5)	1.66 (1.5)	1.44

[a] Theoretical coordination numbers for a cluster of 15 Ru atoms with simulated morphologies under H_2 and CO atmospheres are given in parentheses.

In order to determine the distribution of Ru and Cs in the 4Ru4Cs/G catalyst for the different reactant exposures, H_2 and CO, a series of models was created where the influence of the Cs promoter on the coordination number and the variation of the first two Ru-Ru coordination shells were examined. These simulations helped us to propose two possible particle morphologies on the basis of the EXAFS results. They are summarized in Figure 4.12, and the corresponding theoretical CN values presented are included in parentheses in Table 4.5 for comparison with experimental values.

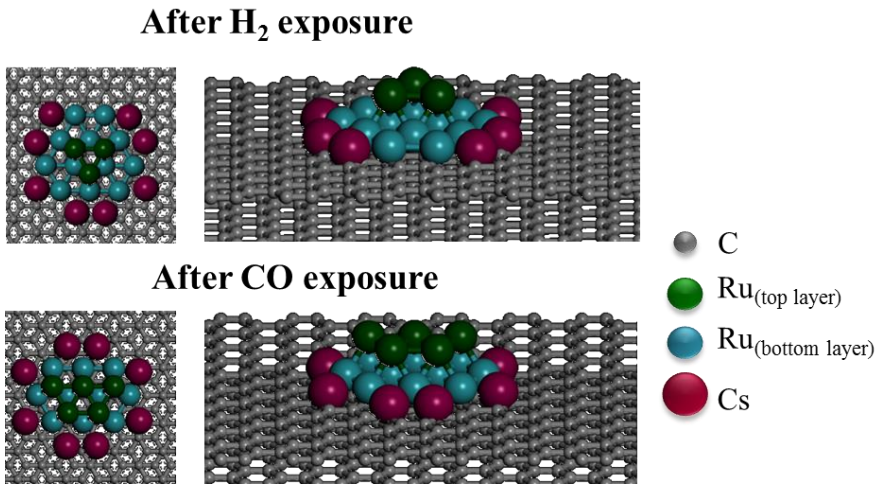

Figure 4.12. Calculated morphologies for the Ru nanoparticles in the 4Ru4Cs/G catalyst after H_2 or CO exposures, respectively.

The EXAFS results suggest the formation of 15-atom particles with flatlike morphology resembling an almost single layer, (111) nanoparticle for the 4Ru4Cs/G catalyst after the reduction treatment and on exposure to H_2 in the cyclic experiment. The Cs atoms are located at the surface of these Ru nanoparticle entities or, more specifically, around the metal in an outer layer. After the CO exposure part of the cycle, the energetic interaction with this reactant molecule (observed in the microcalorimetry experiments) drives the atom

rearrangement in the particle to become more 3D compact, which results in a growth of the second layer, as estimated from the change in the coordination number for the second Ru-Ru shell. Although a morphologic change is observed, no modification of either the Ru nanoparticle size or the Cs content in the outer layer of these bimetallic entities is detected (the coordination numbers of the Ru first shell and Cs neighbors remain unchanged within experimental error from those in the absence of CO). The promoter presence surrounding the Ru clusters prevents possible agglomeration of the metal particles [12]. These observations are the same after successive H_2-CO cycles. The bordering location of Cs promoter atoms also correlates well with our previous investigations on carbon-supported Ru catalysts promoted by Na, where it was demonstrated that the Na atoms act as a barrier between the Ru particles and the carbon support, preventing the H diffusion from the metal to the support [13, 14].

It is worth noting that our XAS results disclose the interaction between the active Ru centers and the alkali-metal promoter on the basis of the interpretation of (i) electronic property modification of both Cs and Ru detected by XANES and (ii) the changes in the particle shape of Ru by interaction with the reactants, as deduced from EXAFS analysis. In other words, the results allow us to interpret the electronic nature of the Cs promotion in the 4Ru4Cs/G catalyst. Thus, the present data suggest that the proximity between Ru and Cs allows that H_2 is activated (during reduction pretreatment) in the Ru centers and subsequently H atoms could diffuse to Cs, leading to a partial reduction of the promoter. In turn, these Cs centers with a higher charge density allow the electronic enrichment of Ru, favoring under a CO reactant atmosphere a stronger π back-bonding with CO and leading to the reconstruction of the Ru-Cs nanoparticle morphology. Recently

Rossetti et al. [5] also detected in a XAS study the partial reduction of Cs in Cs-Ru/C catalysts, but no evidence of Ru atoms in the neighborhood of Cs was observed. Therefore, they explained the Ru-Cs electronic interaction as being mediated by the support through the formation of Cs intercalation compounds in a highly graphitized support.

Catalytic Properties. Catalytic activity and product selectivity are given in Table 4.6. The tests were carried out at 15 bar and 240 °C to observe the performance of catalysts under industrially relevant conditions but also were performed at 3.5 bar (near atmospheric pressure) to parallel the experimental conditions of the in situ XAS experiments. The role of the Cs promoter in the high-surface-area-graphite-supported Ru catalysts under relevant Fischer-Tropsch reaction conditions is evidenced by the lower activity for CO conversion, enhanced light olefin selectivity, lower methane production, and increased chain growth probability (α) in comparison with the nonpromoted catalyst. The disparity between the product selectivity of the nonpromoted and Cs-promoted catalysts decreased with decreasing reaction pressure but still is clearly evident.

Table 4.6. Catalytic Performance of Ru Catalysts Reduced at 400 ºC in the Fischer-Tropsch Reaction.

	3.5 bar [a]		15 bar [b]	
	4Ru/G	4Ru4Cs/G	4Ru/G	4Ru4Cs/G
Activity ($\mu mol/g_{Ru}$ s)	8.5	2.0	106	58
CO Conversion (%)	4.3	1.0	15.5	8.2
CO_2 Selectivity (%)	2	7	0	5
Product distribution:				
CH_4	82	63	49	11
C_2-C_6	18	37	34	33
C_{7+}	-	-	17	56
α^c	0.57	0.68	0.76	1.0
O/(O + P)[d]	0.07	2.75	0.97	3.15

[a] Reaction conditions: CO/H_2/He (5/10/30, flow rate = 45 mL/min), pressure of 3.5 bar, temperature 250 ºC, catalyst (0.5 g), 9 h. [b] Reaction conditions: CO/H_2 (1/2, flow rate 50 mL/min), pressure 15 bar, temperature 240 ºC, catalyst (0.5 g), 50 h. [c] The α value was calculated using the Anderson-Schulz-Flory (ASF) distribution in the hydrocarbon range of C_2-C_6. [d] The O/(O + P) value was calculated from the ratio of olefin divided by total hydrocarbons (olefin + paraffin) in the range of C_2–C_4 hydrocarbons.

The formation of long-chain hydrocarbons in the Fischer-Tropsch reaction has been proposed to occur through the carbide mechanism, which involves polymerization of CH_x building blocks generated from syngas by CO dissociation followed by C hydrogenation [15]. The product composition is described by the Anderson-Schulz-Flory distribution [16]. According to this mechanism, the F-T reaction comprises three main surface reaction steps: (i) CO dissociation (H assisted [17] or direct [18]) and formation of CH_x intermediates, (ii) chain growth by CH_x insertion and subsequent hydrogen transfer, and (iii) termination to form the hydrocarbon. Two different termination steps are possible, namely H addition and β-H elimination, giving rise respectively to paraffins and olefins. Hence, from

a kinetic point of view, an efficient balance between these reactions is necessary for a high selectivity toward the formation of long-chain hydrocarbons and olefins. To have a high rate of chain growth, the rate of chain termination has to be slow and that of C-C coupling fast. The latter implies that the rates of CO dissociation and CH_x formation have to be fast, as these two reactions provide the building blocks for chain propagation. In contrast, when CO dissociation is slow, the surface concentration of CH_x species to be inserted into the growing hydrocarbon chain is low, which leads to a decreased rate of chain growth and higher methane selectivity.

XAS data revealed for the Cs-promoted Ru catalyst that there is a direct Ru-Cs bond, and this is reflected in the partial reduction of the Cs promoter and in reversible changes in the Ru-Cs nanoparticle shape when hydrogen is switched to CO and vice versa (Figure 4.12.). From this, a strong interaction of the CO molecule with the surface of the Ru-Cs nanoparticles can be inferred. Moreover, the microcalorimetry of CO adsorption has straightforwardly shown (Figure 4.2) that the presence of the alkali metal increases the adsorption heat of CO on the promoted Ru catalyst with respect to the nonpromoted Ru catalyst. According to the Blyholder model [19], it can be argued that at the same time the C-O strength decreases its dissociation is favored. This is consistent with a lower barrier for CO dissociation leading to a higher surface coverage of adsorbed dissociative CO. The higher CO dissociation activity results in a higher concentration of CH_x species at the surface, which helps to increase the rate of the C-C coupling reaction [20]. The high population of C_1 adsorbed species, as already reported [21], self-blocks the active sites for further CO dissociation; as a consequence, the overall rate of the reaction becomes slower. At the same time the adsorption of H_2

is hindered on the blocked surface active sites. The decrease in the surface hydrogen pool disfavors chain termination by hydrogenation reaction, which brings about an increase of olefin formation, a lower production of methane, and more long-chain hydrocarbon production.

4.2. References

[1] M. Cerro-Alarcón, A. Maroto-Valiente, I. Rodríguez-Ramos, A. Guerrero-Ruiz, *Carbon*, 43 (2005) 2711-2722.

[2] L. Gonzalo-Chacón, M. Almohalla, E. Gallegos-Suarez, A. Guerrero-Ruiz, I. Rodríguez-Ramos, *Appl. Catal. A* 480 (2014) 86-92.

[3] M. Guraya, S. Sprenger, W. Rarog-Pilecka, D. Szmigiel, Z. Kowalczyk, M. Muhler, *Appl. Surf. Sci.* 238 (2004) 77-81.

[4] K. Aika, K. Shimazaki, Y. Hattori, A. Ohya, S. Ohshima, K. Shirota, A. Ozaki, *J. Catal.* 92 (1985) 296-304.

[5] I. Rossetti, L. Sordelli, P. Ghigna, S. Pin, M. Scavini, L. Forni, *Inorg. Chem.* 50 (2011) 3757-3765.

[6] K. Lu, B. J. Tatarchuk, *J. Catal.* 106 (1987) 166-175.

[7] A. Guerrero-Ruiz, E. Gallegos-Suarez, L. Gonzalo-Chacón, I. Rodríguez-Ramos, *Thermochim. Acta* 567 (2013) 112-117.

[8] M. Fernández-García, C. Márquez, G. L. Haller, *J. Phys. Chem*. 99 (1995) 12565-12569.

[9] C. Márquez-Alvarez, I. Rodríguez-Ramos, A. Guerrero-Ruiz, G. L. Haller, M. Fernández-García, *J. Am. Chem. Soc*. 119 (1997) 2905-2914.

[10] G. Agostini, A. Piovano, L. Bertinetti, R. Pellegrini, G. Leofanti, E. Groppo, C. Lamberti, J. *Phys. Chem. C* 118 (2014) 4085-4094.

[11] G. L. Bezemer, J. H. Bitter, P. C. E. Kuipers, H. Oosterbeek, J. E. Holewijn, X. Xu, F. Kapteijn, A. J. van Dillen, K. P. de Jong, *J. Am. Chem. Soc.* 128 (2006) 3956-3964.

[12] F. R. García-García, A. Guerrero-Ruiz, I. Rodríguez-Ramos, *Top. Catal.* 52 (2009) 758-764.

[13] F. R. García-García, A. Guerrero-Ruiz, I. Rodríguez-Ramos, A. Goguet, S. O. Shekhtman, C. Hardacre, *Phys. Chem. Chem. Phys.* 13 (2011) 12892-12899.

[14] F. R. García-García, N. Bion, D. Duprez, I. Rodríguez-Ramos, A. Guerrero-Ruiz, *Catal. Today* 259 (2015) 9-18.

[15] R. A. van Santen, I. M. Ciobica, E. van Steen, M. M. Ghouri, *Adv. Catal.* 54 (2011) 127-187.

[16] H. Schulz, *Appl. Catal. A: Gen.* 186 (1999) 3-12.

[17] B. T. Loveless, C. Buda, M. Neurock, E. Iglesia, *J. Am. Chem. Soc.* 135 (2013) 6107-6121.

[18] S. Shetty, A. P. J. Jansen, R. A. van Santen, *J. Am. Chem. Soc.* 131 (2009) 12874-12875.

[19] G. Blyholder, *J. Phys. Chem.* 68 (1964) 2772-2777.

[20] J. Chen, Z.-P. Liu, *J. Am. Chem. Soc.* 130 (2008) 7929-7937.

[21] S. B. Vendelbo, M. Johansson, D. J. Mowbray, M. P. Andersson, F. Abild-Pedersen, J. H. Nielsen, J. K. Nørskov, I. Chorkendorff, *Top. Catal.* 53 (2010) 357-364.

Chapter 5

Ruthenium particle size and cesium promotion effects in Fischer-Tropsch synthesis over high-surface-area graphite supported catalysts

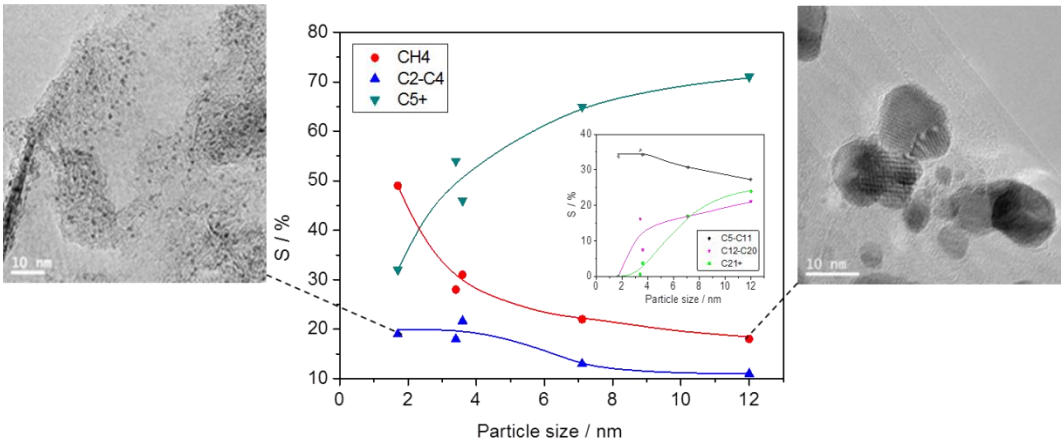

The effect of ruthenium particle size on Fischer-Tropsch synthesis (FTS) has been studied at 513 K, H_2/CO = 2 and 15 bar. Supported Ru catalysts with particle sizes ranging from 1.7 to 12 nm were prepared by using different Ru loadings and two different high surface area graphite (HSAG) supports to minimize the metal-support interaction. In addition, the effect of promotion with Cs is also evaluated. Microcalorimetric characterization during CO adsorption and XPS reveal a clear interaction between Ru and Cs. The FTS with Ru-based catalysts is, independent of the presence of promoter, highly structure-sensitive when the Ru particle size is under 7 nm. In this range the turnover frequency (TOF) for CO conversion increases with particle size, reaching a near constant value for Ru particles larger than 7 nm. Cs promoted catalysts display lower TOF values than the corresponding unpromoted samples. This somewhat reduced activity is attributed to the stronger CO adsorption on Cs promoted catalysts, as demonstrated by CO adsorption microcalorimetry. Product selectivity depends also on Ru particle size. Selectivity to C_{5+} hydrocarbons increases with increasing Ru particle size. For Cs-promoted catalysts, the olefin to paraffin ratio in the C_2-C_4 hydrocarbons range is independent of the Ru particle size, whereas it decreases for the unpromoted catalysts, showing the prevailing influence of the promoter.

5.1 Results and Discussion

Catalysts Characterization. Table 5.1 summarizes the chemical composition of the prepared catalysts determined by total reflection X-ray fluorescence (TRXF).

Table 5.1. Ruthenium and cesium loading for all catalysts.

Catalyst	Ru (wt%)	Cs (wt%)
20Ru/G100	17.3	-
20Ru1Cs/G100	16.6	1.00
10Ru/G100	9.3	-
10Ru0.5Cs/G100	9.4	0.50
5Ru/G100	5.1	-
5Ru0.25Cs/G100	4.9	0.25
20Ru/G400	16.6	-
20Ru1Cs/G400	16.8	1.00
4Ru/G400	3.6	-

Figure 5.1 shows the TPR profiles of the non-promoted and Cs-promoted ruthenium samples. All catalysts show two overlapping peaks of hydrogen consumption at around 400 K, the envelope being centered in the second peak, that can be assigned to the reduction of Ru (III) to Ru(0) species [1, 2]. At temperatures above 700 K hydrogen is also consumed for all catalysts due to the partial gasification of the carbon support around metallic particles to give CH_4, as previously reported for other carbon supported Ru catalysts [3]. 20Ru and 20Ru1Cs/G400 catalysts show the Ru reduction peak with a maximum at around 427 K whereas catalysts of Ru, Ru-Cs/G100 series exhibit the main peak at temperatures that range from 412 up to 450 K. The variation in reduction temperature is related with the different particle size of Ru in the catalyst as will be later discussed. Larger Ru particles are reduced at higher temperature than small Ru particles due to the absence of interaction of the metal with the graphite support. From the TPR characterization, it can be assured that all the catalysts are completely reduced during the treatment in hydrogen at 673 K.

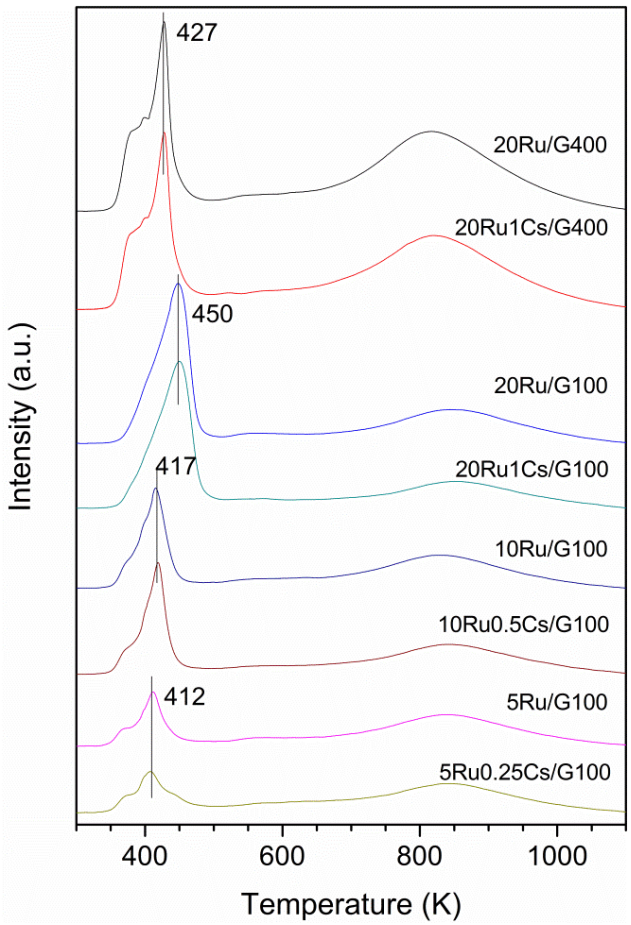

Figure 5.1. Hydrogen consumption profiles during temperature programmed reduction for the Ru and Ru-Cs catalysts (5 K/min).

Diffraction patterns of the Ru catalysts reduced at 673 K are displayed in Figure 5.2. The sharp reflections at 30.6^{o} and 65^{o} are characteristic of the graphite structure and become sharper when the graphitic character of the support increases. Reflections at 2θ = 45^{o}, 49^{o}, 51^{o}, 70^{o} and 85^{o} (grey triangles in Figure 5.2) characteristic for metallic ruthenium are also observed in the Ru/G and Ru-Cs/G catalysts. These reflections have low intensities and are quite wide, indicating a high dispersion of the ruthenium in the catalysts. The average particle sizes of ruthenium crystallites, calculated from the most intense reflection at 2θ = 51° using the Scherrer equation, are shown in Table 5.2. 20Ru1Cs/G100 and 20Ru/G100 catalysts have the largest particle size followed by 10Ru0.5Cs/G100

and 10Ru/G100 catalysts. For the other catalysts no reflections of metallic ruthenium were observed indicating that the particle size values are below to the experimental detection limit for the XRD technique (4.5 nm).

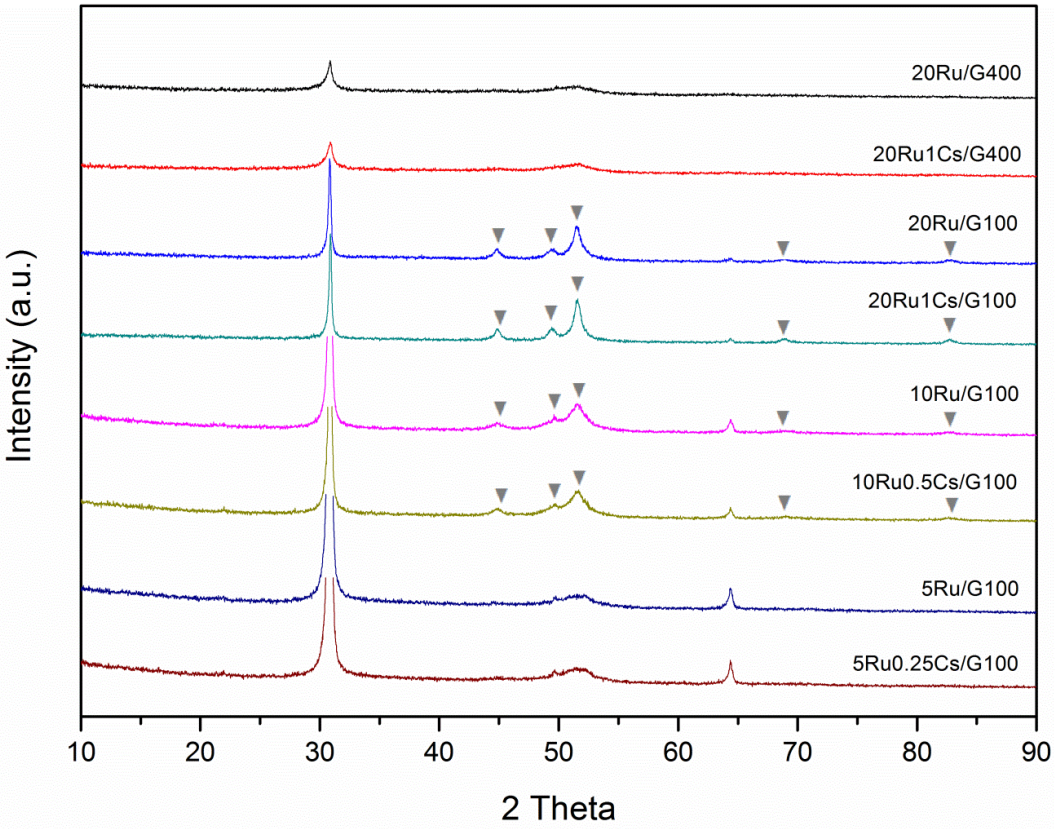

Figure 5.2. XRD pattern after reduction in H_2 at 673 K for Ru and Ru-Cs catalysts. (▼) Reflections from Ru(0) phase.

Table 5.2 also summarizes the CO uptakes and the average metal particle sizes obtained from both CO chemisorption and TEM measurements for the non-promoted and Cs-promoted ruthenium catalysts. Particle sizes determined by TEM are smaller than those obtained by CO chemisorption independently of the catalyst composition. However, the TEM-values are very similar to those determined from XRD (when data are available). Residual chloride species anchored on Ru metal particles or close to them may block adsorption sites for CO molecules. It is considered that some chloride species may remain on the

catalyst surfaces even upon the reduction treatment applied at 673 K [4, 5]. Moreover, a Ru-CO stoichiometry 1:1 is assumed for metal dispersion calculation. But the presence of adsorbed CO in bridging configuration on two Ru atoms is possible and this would be reflected in larger average particle sizes of ruthenium.

Table 5.2. Textural properties of the ruthenium and cesium promoted catalysts reduced in hydrogen at 400 ºC for 2 h.

Catalyst	CO uptake ($\mu mol/g_{Ru}$)	d_{CO} (nm)	d_{TEM} (nm)	d_{XRD} (nm)
20Ru/G100	65	33.2	12.0	17.2
20Ru1Cs/G100	83	26.4	12.7	18.4
10Ru/G100	67	18.1	7.1	8.4
10Ru0.5Cs/G100	78	15.6	7.5	9.0
5Ru/G100	58	11.5	3.4	*
5Ru0.25Cs/G100	61	10.5	4.2	*
20Ru/G400	150	14.6	3.6	*
20Ru1Cs/G400	202	10.8	4.2	*
4Ru/G400	98	4.5	1.7	*

* Below technique detection limit (< 4.5 nm)

TEM analysis suggests that addition of Cs to the ruthenium catalyst slightly increases the ruthenium metal particle size compared to the unpromoted catalyst. By contrast, CO chemisorption shows the opposite effect, attributed to the presence of the promoter which increases the amount of CO molecules adsorbed on the catalyst surface. This suggests that the CO adsorption mode is changed on Ru atoms adjacent to Cs ions from bridged toward linear adsorption.

Representative TEM images of the catalysts and histograms with particle size distributions are shown in Figures 3 and 4. Comparison of catalysts with the same metal loading but with increasing surface area of support reveals that the average particle size of ruthenium decreases by a factor of four, in line with the increase in available surface area (see Table 5.2 and also compare the histograms

in Figures 5.3a and 5.3d). Furthermore, the catalyst supported on graphite with lower surface area, 20Ru/G100, presents a Ru particle size distribution wider than that on the graphite with higher surface area, 20Ru/G400. Similar features are observed for catalysts with the same support when ruthenium metal loading is decreased: the average particle size of ruthenium decreases from 12 to 3.4 nm and the particle size distribution becomes narrower (see Table 5.2 and Figures 5.3a, 5.3b and 5.3c). Next to a slight increase, the particle size distribution broadens for all catalysts after Cs addition, especially for 20Ru1Cs/G100 and 10Ru0.5Cs/G100 catalysts where the frequency of particles larger than 16 or 7 nanometers, respectively, is significantly incremented (Figure 5.4).

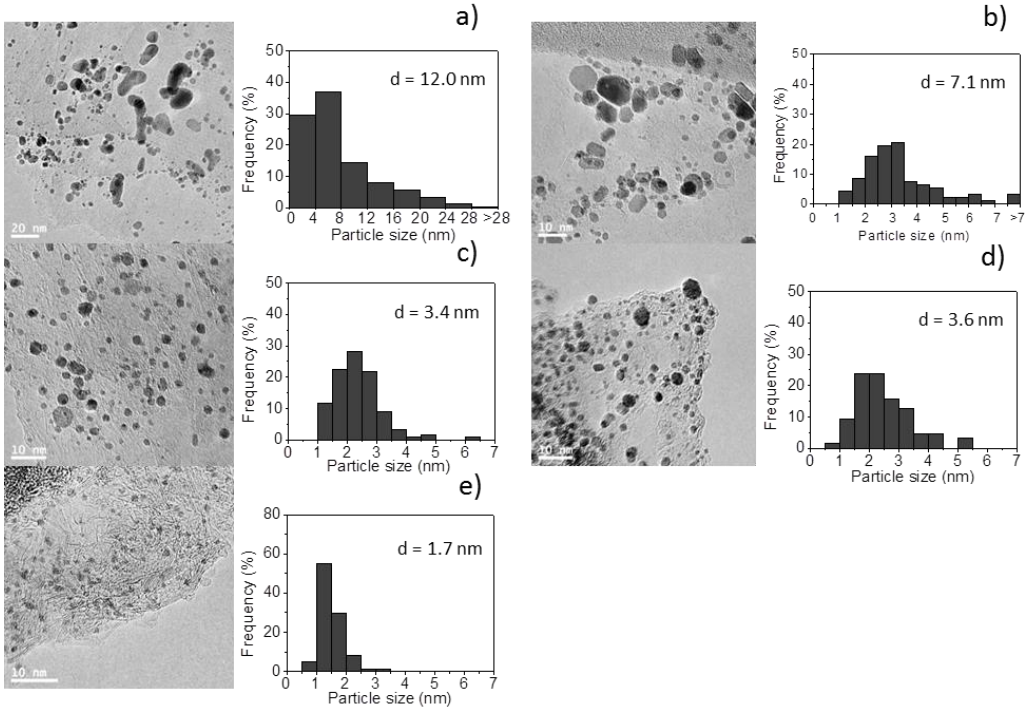

Figure 5.3. Particle size distribution and TEM images of reduced Ru catalysts. (a) 20Ru/G100, (b) 10Ru/G100, (c) 5Ru/G100 (d) 20Ru/G400, (e), 4Ru/G400.

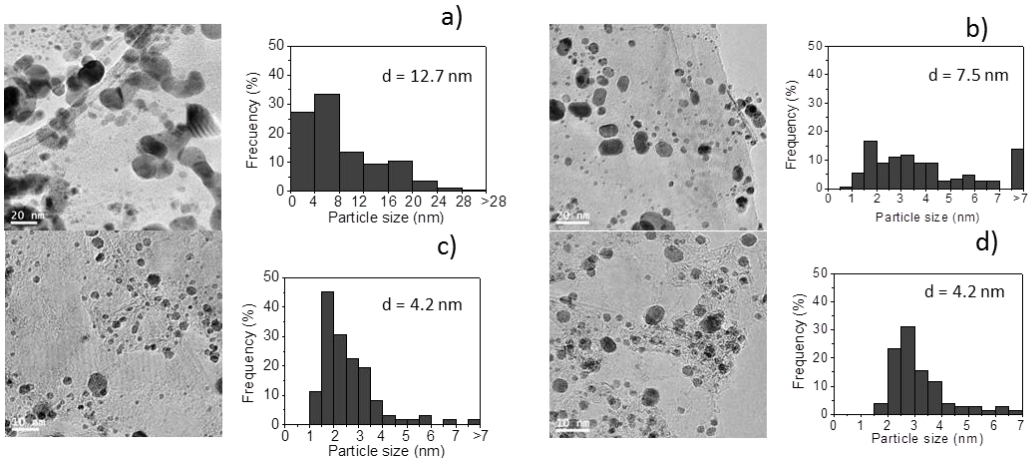

Figure 5.4. Particle size distribution and TEM images of reduced Ru-Cs catalysts (a) 20Ru1Cs/G100, (b) 10Ru0.5Cs/G100, (c) 5Ru0.25Cs/G100, (d) 20Ru1Cs/G400.

Information about the strength and energetic distribution of the surface adsorption sites on the catalysts was obtained from the microcalorimetric profiles of CO adsorption. Figure 5.5 shows the differential enthalpies of CO adsorption (Q_{diff}) as a function of surface coverage for the 10Ru/G100, 10Ru0.5Cs/G100, 5Ru/G100 and 5Ru0.25Cs/G100 catalysts reduced at 673 K in hydrogen for 2 h. Adsorption heat values and shapes of microcalorimetric profiles are different, depending on the metal content and presence of promoter. The profiles for 5Ru/G100 and 5Ru0.25Cs/G100 catalysts (Figure 5.5b) exhibit a high initial adsorption heat of 128 kJ/mol. This high value is typical of highly energetic active sites usually associated with small ruthenium nanoparticles, with preferentially populated edges, corners and other metallic low coordinated Ru-sites. This initial adsorption heat quickly decreases to reach a constant value of 95 and 105 kJ/mol (5Ru/G100 and 5Ru0.25Cs/G100, respectively) for surface coverages from 0.1-0.2 to 0.8 and finally drops down to 40 kJ/mol (physisorption values). Beyond coverage ranges of 0.8 the intensity of the dipole-dipole interactions among CO

molecules adsorbed on Ru faces increases weakening the metal-CO bond. It is important to note that the CO adsorption heats on Cs promoted ruthenium catalyst are higher than those of the unpromoted Ru catalyst, for the surface coverage range from 0.1 to 0.8 (Figure 5.5b). According to certain authors [6, 7, 8], cesium is believed to act as electronic promoter donating part of its electron density to Ru even in its oxidized form. A partial reduction would promote more efficient charge transfer to Ru, as was shown in previous works [9]. Such electronic transfer would produce a strengthening in the π component of the Ru-CO bond (by larger π back-donation from the metal atoms to antibonding molecular orbitals of the CO molecule). Due to the synergetic character of the two contributions (σ and π) to the metal-CO molecule bond the overall metal-CO bond is strengthened and higher CO adsorption heats would be obtained [10].

This electronic effect is also observed comparing the 10Ru/G100 and 10Ru0.5Cs/G100 catalysts (Figure 5.5a). Similarly, CO adsorption heats on Cs promoted ruthenium catalyst are higher than those of the non-promoted Ru catalyst due to the cesium promoter effect. In this case, a plateau with constant adsorption heat values from 0.05 to 0.3 coverage, without highly strong surface sites at very low coverage (lower than 0.2), and further a slow decrease up to a fractional coverage of 0.8 is observed. This finding reveals the absence of highly energetic active sites such as, edges, corners or other metallic (Ru) low coordinated sites because in these samples ruthenium particles sizes are greater, as discussed above.

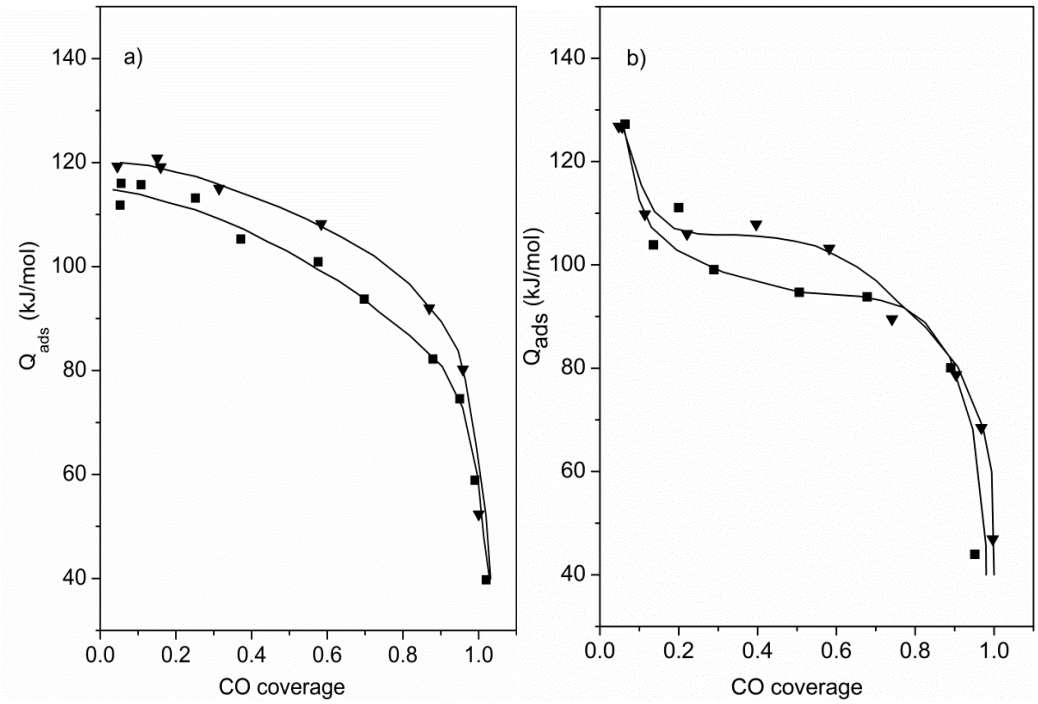

Figure 5.5. Differential heats of CO adsorption at 331 K as a function of surface coverage for: (a) (■) 10Ru/G100, (▼) 10Ru0.5Cs/G100 catalysts and (b) (■) 5Ru/G100 and (▼) 5Ru0.25Cs/G100 catalysts.

Comparison of 10Ru/G100 and 5Ru/G100 also reveals that the increase in Ru loading results in higher heats of CO adsorption over the coverage range from 0.1 to 0.7. If the two Cs promoted catalysts are compared between each other, a similar trend is observed. The large proportion of surface sites with higher adsorption heats shown by catalysts with 10 wt% Ru loading may be attributed to an increase of the electron density of the Ru sites due to the presence in these samples of larger metal particles (see Table 5.2).

Surface composition and electronic state of Ru in 10Ru and 10Ru0.5Cs/G100 catalysts was investigated by XPS. The XPS spectra in the region of Ru $3d_{5/2}$ peak are shown in figure 5.6. The binding energy of Ru $3d_{5/2}$ was of 280.45 and 280.24 eV for 10Ru and 10Ru0.5Cs/G10, respectively, which is assigned in the literature to reduced forms of ruthenium [11]. The binding

energy of Ru $3d_{5/2}$ on the Cs promoted catalyst shifts 0.21 eV towards lower energy values. This shift to lower binding energy suggests an electron enrichment of the surface Ru atoms. The increase in electron density of ruthenium atoms may be attributed in a first stage to the slight increase in Ru particle size observed in the promoted catalyst with respect to the non-promoted (see TEM and XRD data in Table 5.2) since electron density of metal particles increases with the growing particles size [12, 13, 14]. But the existence of an electronic interaction between Ru and Cs with electron transfer from Cs to Ru can definitively lead to an enhanced electron density of Ru atoms as already postulated from the CO chemisorption measurements.

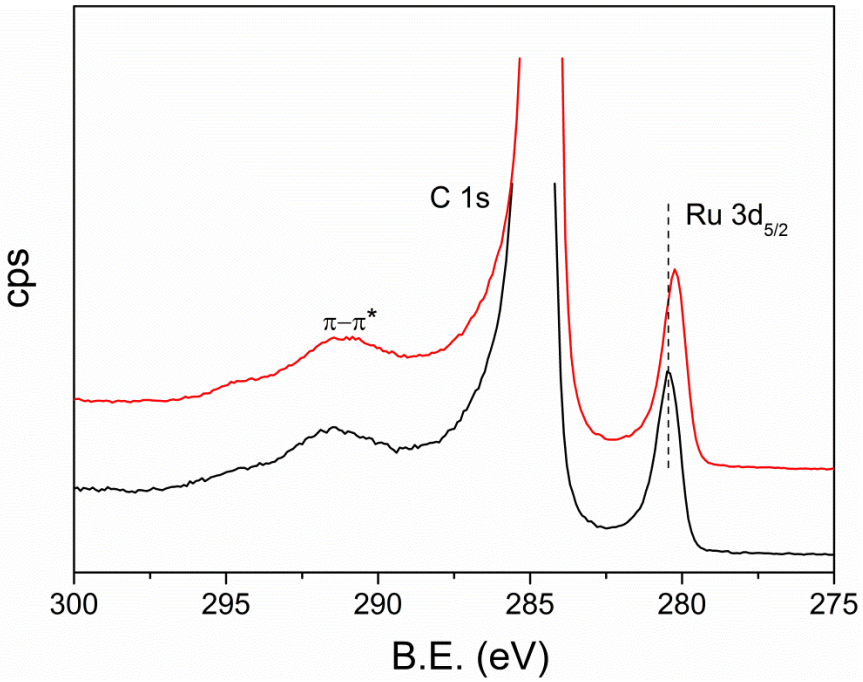

Figure 5.6. XPS spectra in the Ru $3d_{5/2}$ region for 10Ru/G100 (black line) and 10Ru0.5Cs/G100 (red line) catalysts after in-situ reduction treatment at 673 K. The C 1s peak of graphite masks the $3d_{3/2}$ component of the Ru 3d doublet.

Table 5.3. XPS analysis

Sample	B.E. Ru $3d_{5/2}$ (eV)	XPS ratios	
		Ru/C	Cs/C
10Ru/G100	280.45	0.011	-
10Ru0.5Cs/G100	280.24	0.011	0.001

Fischer-Tropsch Synthesis. Promoted and unpromoted Ru catalysts were tested under FTS conditions at 15 bar to assess the effect of ruthenium particle size on catalytic performance. Equal amount of catalyst was used in all the experiments. Figure 7 shows the evolution of CO conversion during 80 h on stream and reveals that after 30 h the reaction reaches steady state conditions. Conversions decrease as foreseen for decreasing Ru loadings, but also on the same loading for lower Ru particle sizes.

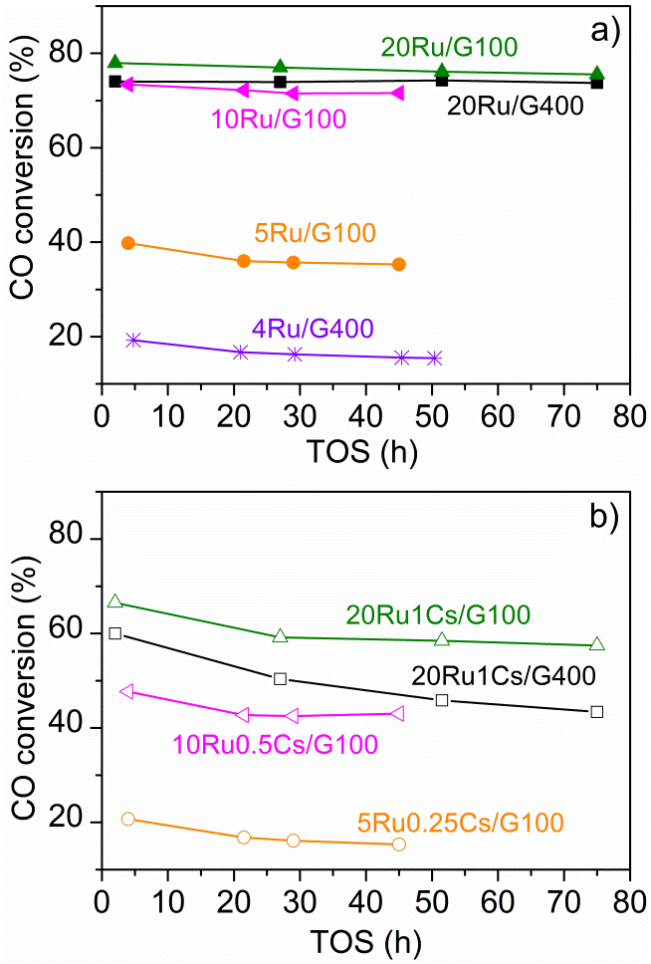

Figure 5.7. Time-on-stream (TOS) evolution of CO conversion during FTS at 513 K, 15 bar, $H_2/CO = 2$ and GHSV = 6.1 $m^3_{STP}\,kg^{-1}\,h^{-1}$. (a) non-promoted and (b) Cs promoted catalysts.

Table 5.4 lists catalytic activity and product selectivity under steady state conditions for all the catalysts. The O/P values calculated from the ratio of olefin to paraffin in the range of C_2-C_4 hydrocarbons and hydrocarbon chain-growth probabilities (α) from Anderson-Schulz-Flory (ASF) plots using a linear regression over carbon numbers three to twenty are also included in Table 5.4.

Table 5.4. Catalytic performance in the Fischer–Tropsch synthesis of Ru and Ru-Cs catalysts reduced at 673 K[a].

Catalyst	*Activity* ($\mu mol/g_{Ru}\ s$)	*CO Conv. (%)*	*CO_2 Select. (%)*	*Product distribution*			α^d	*O/P*[e]
				CH_4	*C_2-C_4*	*C_{5+}*		
20Ru/G100[b]	115.8	76	0.2	18	11	71	0.85	0.48
20Ru1Cs/G100[b]	86.5	57	0.8	4	5	91	0.88	2.17
10Ru/G100[c]	191.4	72	0.1	22	13	65	0.84	0.79
10Ru0.5Cs/G100[c]	113.7	43	0.2	7	7	86	0.86	2.18
5Ru/G100[c]	170.5	35	0.3	28	18	54	0.78	0.98
5Ru0.25Cs/G100[c]	77.1	15	0.0	21	15	64	0.80	2.24
20Ru/G400[b]	112.1	74	0.4	31	23	46	0.73	1.09
20Ru1Cs/G400[b]	64.0	43	0.0	21	11	68	0.81	2.10
4Ru/G400	106.6	15	0.0	49	19	32	0.70	1.13

[a] Reaction conditions: CO/H_2 (1/2, flow rate = 50 ml/min), pressure of 15 bar, temperature of 513 K, catalyst (0.5 g). [b] 75 h time on stream. [c] 45 h time on stream. [d] The α value was calculated using Anderson–Schulz–Flory (ASF) distribution in the hydrocarbon range of C_3-C_{20}. [e] The O/P value was calculated from the ratio of olefin to paraffin in the range of C_2-C_4 hydrocarbons.

Independently of the support, loading and ruthenium particle size, the addition of the promoter implies a decrease in the catalytic activity, an enhancement of light olefin production (higher O/P ratio) and higher selectivity toward C_5^+ hydrocarbons (increased α) compared to its non-promoted counterparts. These results agree with previous X-ray absorption spectroscopy results [9] where we demonstrate the close interaction between Ru and Cs supported on high surface area graphite under FT reaction atmosphere and its effects in the catalytic performance. Similarly, the above XPS experiments revealed the electronic interaction between Ru and Cs, which is further supported by the stronger CO adsorption measured by microcalorimetry. According to the FT mechanism, long-chain-hydrocarbon formation involves the polymerization of CH_x species, formed from CO dissociation and subsequent C hydrogenation [15],

following the Anderson-Schulz-Flory distribution [16].The termination of the chain can occur by H addition or by β-elimination resulting in paraffins or olefins, respectively. So on the promoted catalysts, the higher population of adsorbed dissociative CO and formation of CH_x species on the surface likely hinder the hydrogen adsorption favoring the chain growth by C-C coupling and the olefin formation. Concurrently, the higher population of C_1 adsorbed species, as already reported [17], self-blocks the active sites for further CO dissociation as a consequence the overall rate of the reaction becomes slower.

To gain further information about the effect of Ru particle size on catalytic activity, the turnover frequency (*TOF*) for CO conversion over the unpromoted and promoted Ru catalysts with different sizes of Ru particles is compared in Figure 5.8. The TOF values were calculated based on the Ru dispersion from TEM measurements.

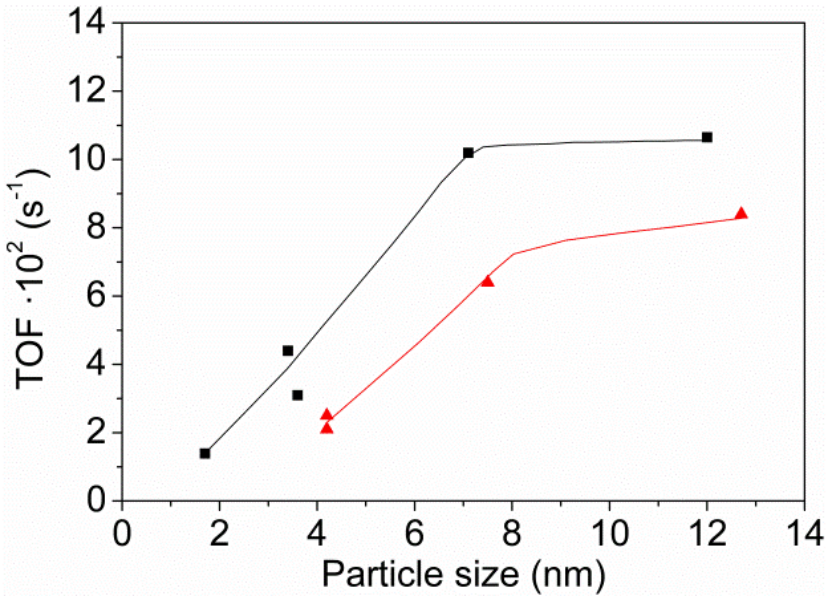

Figure 5.8. The influence of ruthenium particle size on the *TOF* for (■) non-promoted and (▲) Cs-promoted catalysts.

The *TOF* is rather constant with a value of around 10^{-1} s^{-1} for non-promoted ruthenium particles above 7 nm and up to 12 nm. For smaller particle sizes, the *TOF* decreases down to a value of 10^{-2} s^{-1} for the 4Ru/G400 catalyst. In the case of Cs-promoted catalysts the *TOF* follows the same trend as a function of the Ru particle size, although the *TOF*-values are decreased by a factor which seems to be independent of metal particle size. In terms of catalytic activity the effectiveness of promotion is similar for small and large particles. Recent studies reported that the critical Ru-particle size below which the CO consumption rate becomes structure sensitive is in the 6-10 nm [18, 19]. This structure-sensitive behavior has been attributed to the decreasing stability of step-edge sites on the surface of smaller particles. These sites, which consist of an ensemble of five metal atoms located at the step edges of large particles and referred to as B5 sites, have been proposed to be essential for low-barrier CO dissociation [20, 21, 22]. In this line, our data support the assumption that a minimum size of the nanoparticles is required to sustain surface sites needed for facile CO dissociation.

Regarding product selectivities, Figure 5.9 shows the changes in selectivity towards different hydrocarbons with the average size of Ru particles for unpromoted (Figure 5.9a) and promoted (Figure 5.9b) catalysts. Selectivity differences between catalysts should be considered with care in the case of large conversion differences between catalysts in view of possible different extents of secondary reactions. In our case, the CO conversion over the non-promoted 5Ru/G100 and 20Ru/G400 catalysts with very similar Ru particle size, 3.4 and 3.6 nm, respectively (see Figure 5.3 and Table 5.2), varied from 35 to 74 % (Table 5.4), whereas the selectivity towards the different products only slightly changed. A similar picture can be described for the promoted 5Ru0.25Cs/G100 and

20Ru1Cs/G400 catalysts (both with mean Ru particle size of 4.2 nm), which gave similar product distributions for CO conversions of 15 and 43 %, respectively. Therefore, under the FTS reaction conditions used in this work CO conversion changes in the range 15-75 % have little influence on the product distribution over unpromoted and Cs-promoted Ru catalysts supported on high surface area graphite. Early results [23, 24] on the effect of CO conversion level for Ru based catalysts supported on metal oxides reported changes in the product distribution. The discrepancy between these studies and our results may be due to metal-support interaction phenomena between the Ru particles and metal oxides such as Al_2O_3 and TiO_2, which may mask the intrinsic effect of the CO conversion. Therefore, the use of a support displaying weak metal-support interactions such as the one used in our work is crucial for the elucidation of ruthenium particle size effects.

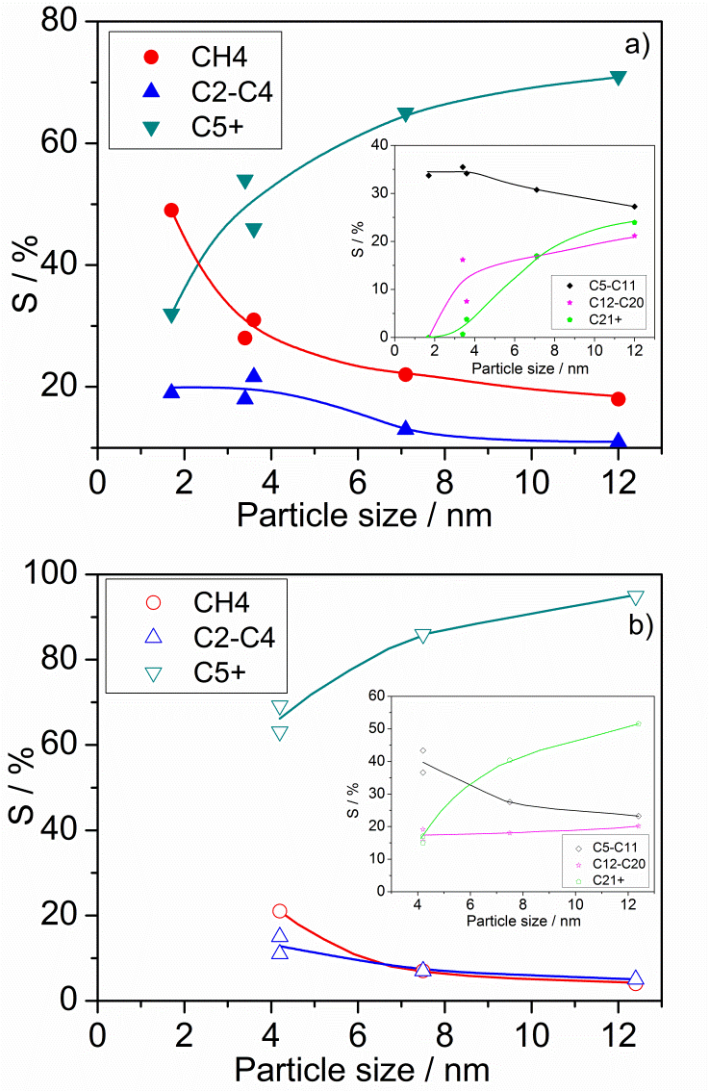

Figure 5.9. Effect of Ru particle size in FTS on selectivity towards different hydrocarbons for (a) unpromoted and (b) Cs-promoted catalysts. Inserts show the variation of C_5-C_{11}, C_{12}-C_{20} and C_{21+} selectivities with particle size.

Figure 5.9 shows that the product selectivity changes significantly with Ru particle size. Selectivities to CH_4 and C_2-C_4 clearly decrease with increasing Ru particle size from 1.7 to 7.1 nm and from 4.2 to 7.5 nm for unpromoted and promoted catalysts, respectively. A further increase in the Ru particle size to 12.0 nm (or 12.7 nm) slightly decreases the selectivities to these light hydrocarbons. Simultaneously, the selectivity to C_{5+} hydrocarbons, particularly that for C_{21+}

(wax) (see insert in Figure 5.9) increases with Ru particle size. The high selectivity toward CH_4 (49 %) obtained over the non-promoted Ru catalysts with the smallest particle size (1.7 nm) demonstrates that the presence of edges and sites with strong CO heat of adsorption results in very poor FTS performance. On the other hand, non-promoted catalysts with Ru particle size of 3.5 nm and above, and Cs-promoted catalyst with Ru particle size of 4.2 nm mainly produce hydrocarbons in the gasoline range (C_5-C_{11}), with a slight increase in the amount of C_{21+} for bigger particle sizes. However, over Cs-promoted catalysts with Ru particle sizes of 7.5 nm and above, C_{21+} hydrocarbons are much more abundant in the product. These results are in good agreement with FTS literature and particularly with results reported by Kang *et al*. [25] for Ru nanoparticles loaded on carbon nanotubes. They found that the selectivities to CH_4 and C_2-C_4 hydrocarbons decreased with increasing the size of the Ru nanoparticles, whereas that to C_{5+} hydrocarbons increased. It has been postulated that the higher C_{5+} selectivity of the larger Ru nanoparticles may be due to their higher active site densities, which may result in higher probability of re-adsorption and polymerization of α-olefin intermediates [26].

Figure 5.10 depicts the effect of Ru particle size on the olefin to paraffin (O/P) ratio in the range of C_2-C_4 hydrocarbons. A continuous decline in the O/P ratio with the increasing size of the Ru particles for the non-promoted catalysts is observed, in agreement with the above speculation that on larger Ru particles the olefins are prone to re-adsorb and to be further hydrogenated. However, over Cs-promoted catalysts, the O/P ratio remains constant in the range of Ru particle size between 4.2-12.4 nm. It seems that for Cs-promoted catalysts the effect of the Cs promoter prevails over the Ru particle size effect. The presence of the promoter,

as above discussed, hinders the hydrogen adsorption on the catalyst surface reducing the possibility to hydrogenate re-adsorbed olefins.

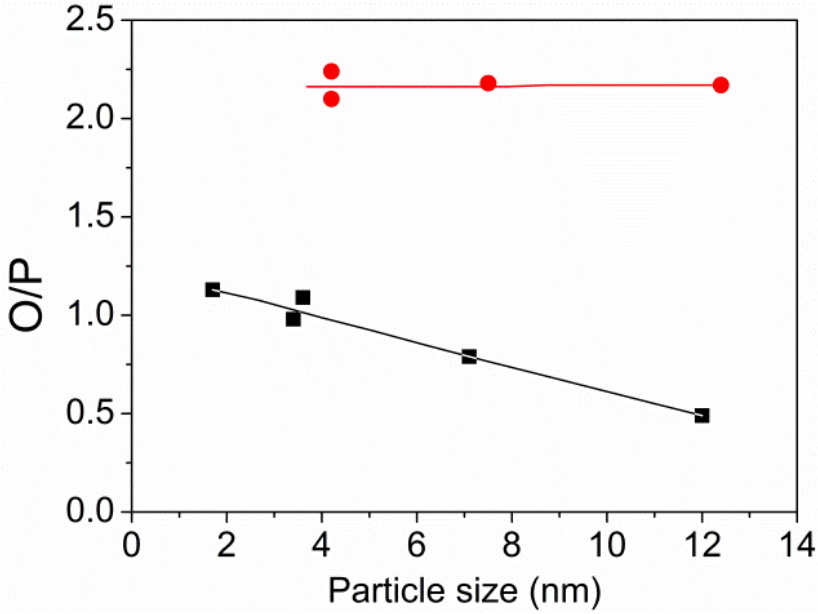

Figure 5.10. Effect of particle size on the olefins to paraffin ratio in the range of C_2-C_4 hydrocarbons for (■) unpromoted and (●) Cs promoted catalysts.

5.2. References

[1] M. Cerro-Alarcón, A. Maroto-Valiente, I. Rodríguez-Ramos, A. Guerrero-Ruiz, *Carbon* 43 (2005) 2711.

[2] A. Guerrero-Ruiz, P. Badenes, I. Rodríguez-Ramos, *Appl. Catal. A* 173 (1998) 313.

[3] B. Bachiller-Baeza, A. Guerrero-Ruiz, P. Wang, I. Rodríguez-Ramos, *J. Catal.* 204 (2001) 450.

[4] K. Lu, B. J. Tatarchuk, *J. Catal.* 106 (1987) 166.

[5] A. Guerrero-Ruiz, E. Gallegos-Suarez, L. Gonzalo-Chacón, I. Rodríguez-Ramos, *Thermochim. Acta* 567 (2013) 112.

[6] M. Guraya, S. Sprenger, W. Rarog-Pilecka, D. Szmigiel, Z. Kowalczyk, M. Muhler, *Appl. Surf. Sci.* 238 (2004) 77.

[7] K. Aika, K. Shimazaki, Y. Hattori, A. Ohya, S. Ohshima, K. Shirota, A. Ozaki, *J. Catal.* 92 (1985) 296.

[8] I. Rossetti, N. Pernicone, L. Forni, *Appl. Catal. A.* 208 (2001) 271.

[9] J. L. Eslava, A. Iglesias-Juez, G. Agostini, M. Fernández-García, A. Guerrero-Ruiz, I. Rodríguez-Ramos, *ACS Catal.* 6 (2016) 1437.

[10] L. Gonzalo-Chacón, M. Almohalla, E. Gallegos-Suarez, A. Guerrero-Ruiz, I. Rodríguez-Ramos, *Appl. Catal. A* 480 (2014) 86.

[11] C. D. Wagner, W. M. Riggs, L. E. Davis, J. F. Moulder, G. E. Muilenberg, Handbook of X-Ray Photoelectron Spectroscopy, Perkin-Elmer Corp., Eden Prairie, Minnesota (1979) pp. 106.

[12] D. Uzio, G. Berhault, *Catal. Rev.* 52 (2010) 106.

[13] V. Ponec, G. C. Bond, Catalysis by Metals and Alloys, Elsevier (1995) pp. 239.

[14] J. K. Nørskov, Prog. *Surf. Sci.* 38 (1991) 103.

[15] R. A. van Santen, I. M. Ciobica, E. van Steen, M. M. Ghouri, *Adv. Catal.* 54 (2011) 127.

[16] H. Schulz, *Appl. Catal. A* 186 (1999) 3.

[17] S. B. Vendelbo, M. Johansson, D. J. Mowbray, M. P. Andersson, F. Abild-Pedersen, J. H. Nielsen, J. K. Nørskov, I. Chorkendorff, *Top. Catal.* 53 (2010) 357.

[18] J. C. Kang, S. L. Zhang, Q. H. Zhang, Y. Wang, *Angew. Chem.* Int. Ed. 48 (2009) 2565.

[19] J. M. G. Carballo, J. Yang, A. Holmen, S. García-Rodríguez, S. Rojas, M. Ojeda, J. L. G. Fierro, *J Catal.* 284 (2011) 102.

[20] R. A. van Santen, *Acc. Chem. Res.* 42 (2009) 57.

[21] S. Shetty, R. A van Santen, *Catal. Today*, 171 (2011) 168.

[22] R. A. van Santen, I. M. Ciobica, E. van Steen, M. M. Ghouri, *Adv. Catal.* 54 (2011) 127.

[23] E. Iglesia, S. C. Reyes, R. J. Madon, *J. Catal.* 129 (1991) 238.

[24] J. Yang, W. Ma, D. Chen, A. Holmen, B. H. Davis, *Appl. Catal. A.* 470 (2014) 250.

[25] J. Kang, W. Deng, Q. Zhang, Y. Wang, *J. Energy Chem.* 22 (2013) 321.

[26] E. Iglesia, *Appl Catal A* 161 (1997) 59.

Chapter 6

Effect of Different Promoter Precursors in a Model Ru-Cs/HSAG System on the Catalytic Selectivity for Fischer-Tropsch Reaction

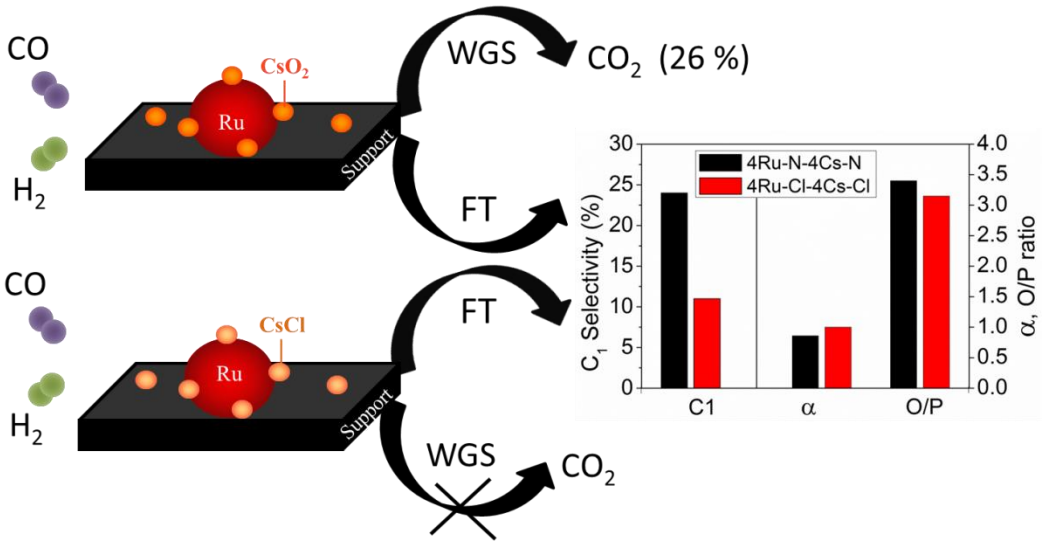

The effect of the promoter precursor on the Fischer-Tropsch synthesis was studied over cesium promoted ruthenium catalysts supported on a high surface area graphite support. In this work we observe significant modifications in the selectivity values for Fischer-Tropsch reaction depending on the Cs promoter precursor (CsCl vs $CsNO_3$). Specifically the bimetallic catalyst (4Ru-4Cs), prepared from nitrogen containing metal and promoter precursors, showed a high selectivity to CO_2 during reaction. By modifying the cesium precursor, it was possible to inhibit the water gas shift reaction, decreasing significantly the selectivity to CO_2. In order to understand the chemical origin of these modifications a careful characterization of the materials was performed including: X-ray absorption near edge spectroscopy, transmission electron microscopy measurements, temperature programmed reduction studies, determination of the CO uptakes on the catalysts and the evolution of the CO adsorption heats as a function of surface coverages. It was found that upon reduction and under reaction atmosphere the promoter in the ex-nitrate catalyst appears as Cs_2O which is considered responsible of the CO_2 production, while in the catalysts prepared with Cs chloride the promoter remains as CsCl suffering a slight partial reduction.

6.1 Results and Discussion

Catalysts Characterization. Table 6.1 summarizes the chemical composition of the prepared catalysts determined by total reflection X-ray fluorescence (TRXF).

Table 6.1. Ruthenium and cesium loading for all catalysts determined by TRXF.

Catalyst	Ru (wt%)	Cs (wt%)
4Ru-N	3.7	-
4Ru-Cl	3.6	-
4Ru-N-4Cs-N	4.2	3.8
4Ru-Cl-4Cs-Cl	3.6	3.4
4Ru-N-4Cs-Cl	3.6	3.6
4Cs-Cl	-	3.7
4Cs-NO	-	3.6

Figure 6.1 shows the TPR profiles of the non-promoted and Cs promoted ruthenium catalysts. Ru-N and Ru-Cl monometallic catalysts show one peak of hydrogen consumption centered at 458 and 450 K respectively that can be assigned to the reduction of Ru^{3+} to Ru^{o} species [1]. When cesium promoter is added the temperature of ruthenium reduction shifted toward higher values in the range 480 to 501 K. This behaviour is due to the existing interaction between ruthenium and cesium salts which is favored on the carbon support owing to the non-interaction of these species with the graphite support. From the TPR experiments, it can be assured that all the catalysts are completely reduced during the treatment in hydrogen at 673 K previous to the FT reaction tests.

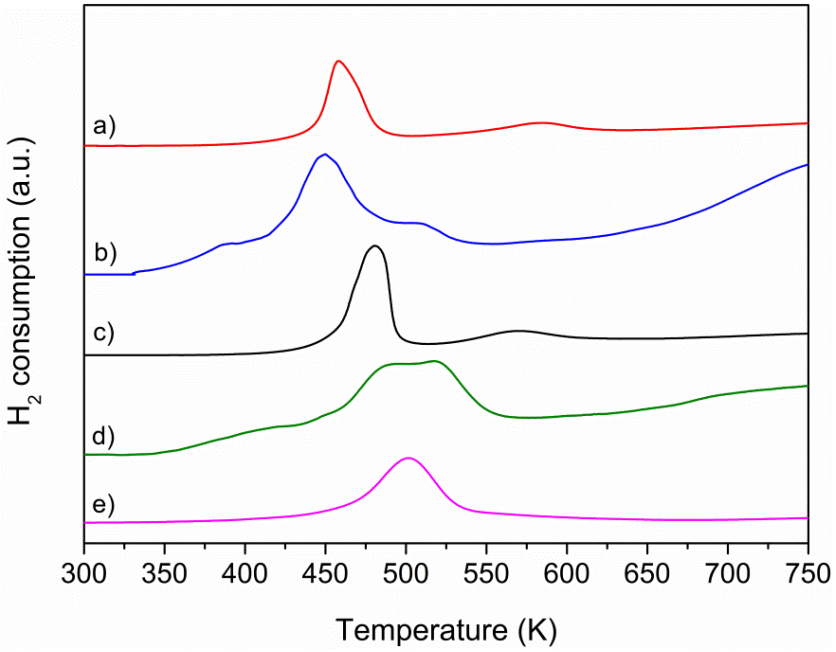

Figure 6.1. Hydrogen consumption profiles during temperature programmed reduction for the catalysts: a) 4Ru-N, b) 4Ru-Cl, c) 4Ru-N-4Cs-N, d) 4Ru-Cl-4Cs-Cl, e) 4Ru-N-4Cs-Cl.

Figure 6.2 presents the microcalorimetric CO adsorption profiles, which allow to obtain information about the strength and energetic distribution of the surface adsorption sites on the catalysts. It can be seen that adsorption heat profiles are different depending on the metal precursor as well as with the incorporation of promoter. 4Ru-N and 4Ru-Cl catalysts exhibit a high initial adsorption heat of 138 kJ/mol. This high value is associated with small ruthenium metal nanoparticles located preferentially at edges or corners where the coordination number is low. This initial adsorption heat quickly decreases to reach a constant value of 122 and 106 kJ/mol for 4Ru-N and 4Ru-Cl, respectively, for surface coverage from 0.2 to 0.7 and finally drops down to 40 kJ/mol (physisorption values). Thus, it has been detected that CO adsorption heats for 4Ru-N sample are higher than for 4Ru-Cl throughout the experiment. This finding

agrees with previous results obtained over ex-choride Ru catalysts [2] and it can be explained because after pretreatment reduction step residual chlorine can remain on the catalyst surface removing electron density from the ruthenium metal nanoparticles and therefore CO adsorption heat on this catalyst is lower.

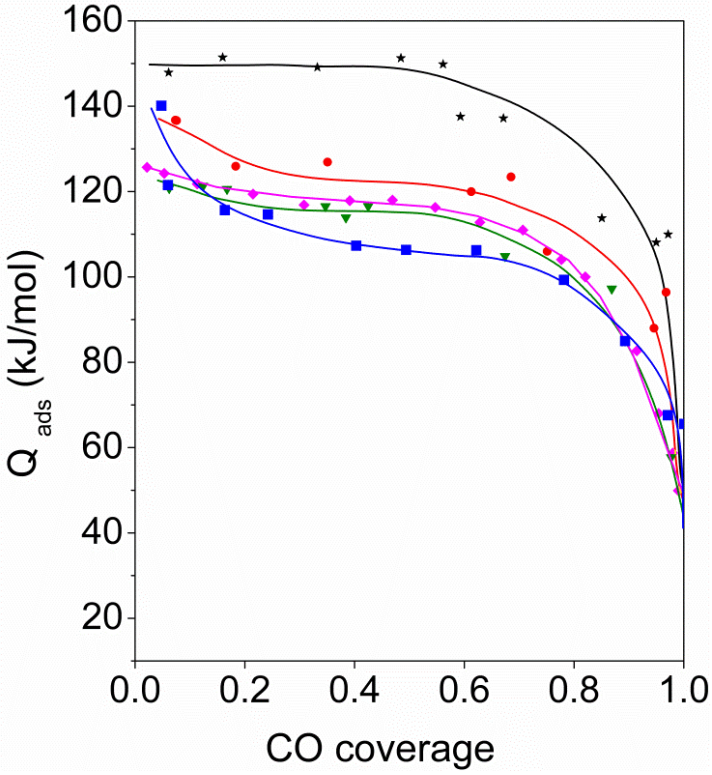

Figure 6.2. Differential CO adsorption heats at 331 K as a function of surface coverage for: (●) 4Ru-N, (■) 4Ru-Cl, (∗) 4Ru-N-4Cs-N, (▼) 4Ru-Cl-4Cs-Cl and (◆) 4Ru-N-4Cs-Cl catalysts.

When cesium is added a diminution in the initial high heats of CO chemisorption is observed between 0.05-0.2 coverages. This fact suggests that Cs ions are likely localized on the highly reactive Ru positions blocking their adsorption properties. Moreover if the monometallic catalyst is compared with the promoted one, when using the same precursor (4Ru-Cl vs 4Ru-Cl-4Cs-Cl or 4Ru-N vs 4Ru-N-4Cs-N) it is revealed that the CO adsorption heats on promoted

ruthenium catalyst are higher than those on non-promoted Ru catalysts. Cesium is believed to be an electronic promoter [3, 4, 5], because it donates part of its electron density to Ru nanoparticles, even in its oxidized form. A strengthening in the Ru-CO bond and higher CO adsorption heats is guessed due to such electronic transfer. On the other hand the sample 4Ru-N-4Cs-Cl shows a CO chemisorption profile very similar to 4Ru-Cl-4Cs-Cl with CO adsorption heats higher than that on 4Ru-Cl but below the 4Ru-N in the whole coverage range. This can be explained considering the residual chlorine withdraws electron density from the ruthenium nanoparticles decreasing the CO adsorption heats, as was explained above, partially neutralizing the promoter effect in the case of the 4Ru-N catalyst.

Representative TEM images of the catalysts and their histograms with particle size distributions are shown in Figure 6.3. Table 6.2 shows the CO uptakes and the average metal particle sizes (nm) obtained from chemisorption measurements and from TEM measurements for the non-promoted and Cs-promoted ruthenium catalysts. It is worth noting that CO uptakes grow for all promoted ruthenium catalysts with respect to the non-promoted catalysts which could have an important effect modifying the Fischer-Tropsch synthesis mechanism. It is observed for all the catalysts that particle sizes determined by CO chemisorption are larger than those obtained by TEM. A reason to explain this fact may rest on the considered adsorption stoichiometry of CO over Ru, since more than one Ru surface atom per chemisorbed CO molecule might be involved. So, we have considered a Ru-CO stoichiometry of 1:1 in order to calculate the number of Ru surface atoms and the metal dispersion, though CO adsorption in bridging configuration on two Ru atoms is also possible and this would be reflected in larger average particle sizes of ruthenium. Therefore, due to these

facts for comparison of the different catalysts we will use hereafter the metal dispersion derived from the metal particle sizes measured by TEM. In addition, TEM measurements reveal a broadening of the particle size distribution for all catalysts after the Cs addition (see figures 6.3a, 6.3b versus 6.3c, 6.3d and 6.3e), especially the frequency of particles larger than 2.5 nanometers.

Table 6.2. CO uptakes and average metal particle sizes obtained from CO chemisorption measurements and from TEM measurements after H_2 pretreatment at 673 K for 2 h.

Catalyst	CO uptake ($\mu mol/g_{cat}$)	d_{CO} (nm)	d_{TEM} (nm)
4Ru-N	115	4.1	1.7
4Ru-Cl	98	4.5	1.7
4Ru-N-4Cs-N	126	4.3	1.9
4Ru-Cl-4Cs-Cl	115	4.5	2.3
4Ru-N-4Cs-Cl	135	4.0	1.9
4Cs-Cl	-	-	-
4Cs-NO	-	-	-

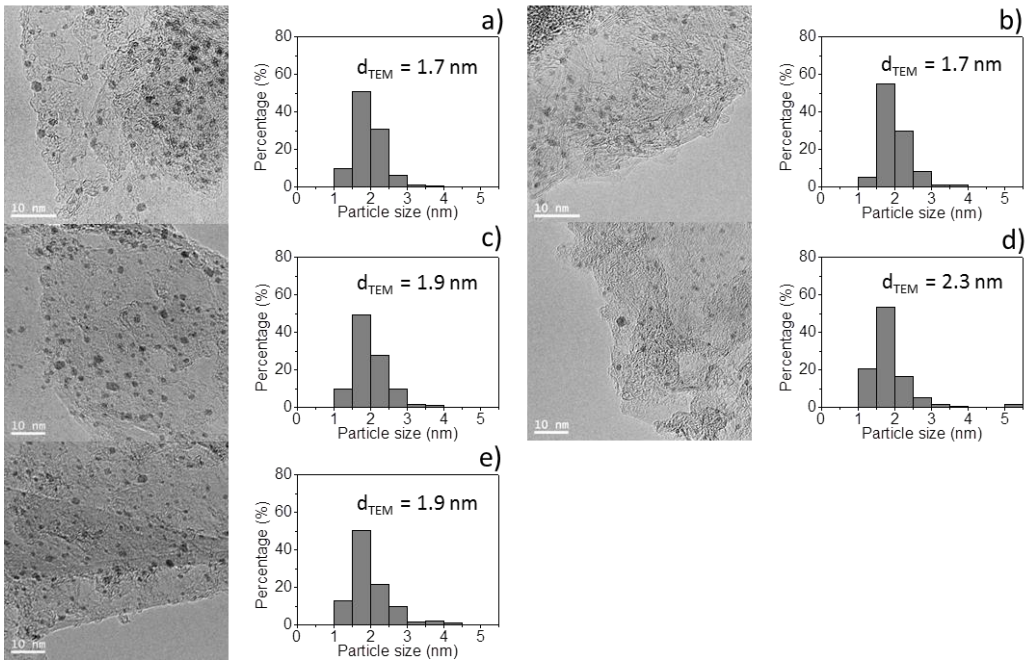

Figure 6.3. TEM images and particle size distribution of reduced Ru catalysts. (a) 4Ru-N, (b) 4Ru-Cl, (c) 4Ru-N-4Cs-N, (d) 4Ru-Cl-4Cs-Cl and (e) 4Ru-N-4Cs-Cl.

In-situ Ru K-edge XANES spectra during the temperature programmed reduction are compiled in Figure 6.4. Above 393-473 K, a decreasing intensity of the white line and a shift of the absorption edge toward lower energies are observed obtaining a spectrum similar to that of Ru^0. The sets of XANES were examined by principal component analysis (PCA) to interpret the reduction process [6, 7]. By means of PCA is possible to determine the number of Ru chemical species and quantify their concentration during the reduction process. Figure 6.5 presents the concentration profiles and XANES spectra corresponding to the pure chemical species of Ru observed during the H_2-TPR experiments. Thus, this indicates two Ru chemical species in the samples 4Ru-N and 4Ru-N-4Cs-N, respectively, during the H_2 treatment. In the case of the 4Ru-Cl and 4Ru-Cl-4Cs-Cl samples two and three Ru chemical species were detected respectively. The reduction of the 4Ru-Cl-4Cs-Cl catalyst is a more complex process, occurring

in two stages with the detection of an intermediate component as it was demonstrated previously [8]. The formation of an intermediate Ru oxidized species at low temperatures for the sample 4Ru-Cl-4Cs-Cl suggests a modification of the electronic properties of Ru entities via interaction with the Cs atoms. Also this behavior indicates that an intimated contact of the Ru nanoparticles and the Cs promoter entities takes place during the reduction process.

In order to determine the oxidation state of the different Ru chemical species, some Ru references were analyzed by XANES representing the edge position versus the oxidation state (presented as Figure 6.6). Below 673 K (reduction temperature for FTS) the total reduction of Ru is achieved for all the catalysts.

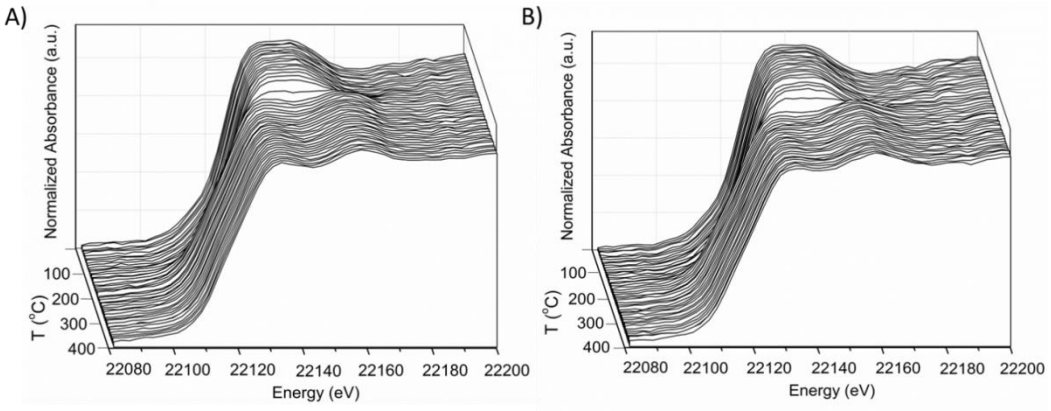

Figure 6.4. Ru K-edge XANES spectra collected at different temperatures during the reduction process. (A) 4Ru-N, (B) 4Ru-N-4Cs-N. The spectra of 4Ru-Cl and 4Ru-Cl-4Cs-Cl have been provided in a previous study [8].

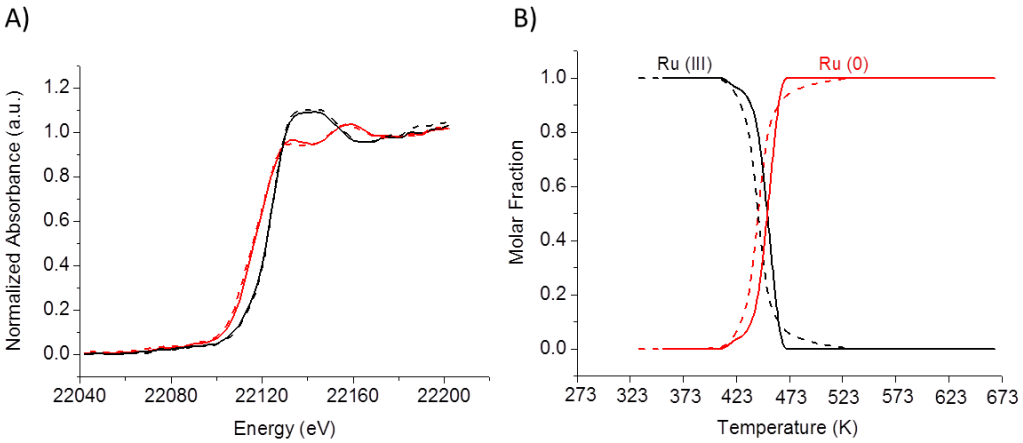

Figure 6.5. Ru K-edge XANES spectra and concentration profiles obtained by PCA corresponding to pure chemical species along H_2-TPR until 673 K for 4Ru-N (solid line) and 4Ru-N-4Cs-N (dashed line) catalysts.

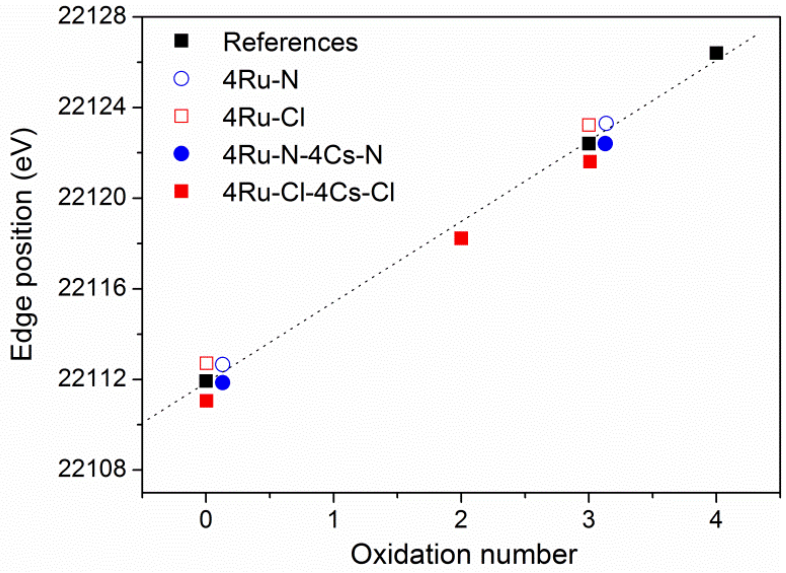

Figure 6.6. Edge position of pure species from FA for 4Ru-N, 4Ru-Cl, 4Ru-N-4Cs-N and 4Ru-Cl-4Cs-Cl catalysts versus oxidation number of selected references: Ru (foil), $RuCl_3$ and RuO_2.

The Cs L_1 edge XANES spectra recorded during the temperature-programmed reduction for the promoted catalysts 4Ru-Cl-4Cs-Cl and 4Ru-N-4Cs-N are reported in Figure 6.7. It can be noticed that the non-reduced samples give

rise to a sharp feature at approximately 5712 eV. For the sample 4Ru-Cl-4Cs-Cl, as already reported [8], the white line intensity suffers a severe decrease attributed to an increase of the d state electron density involved in the 2s-3d resonance transition. In addition, a significant 0.68 eV shift of the absorption edge toward lower energies was observed after reduction at 673 K. The study concludes [8], in agreement with other authors [5], that partial reduction of CsCl is produced by H species coming from the dissociative chemisorption of H_2 on Ru. By contrast, for the 4Ru-N-4Cs-N sample a spectra with nearly equal edge shape and with identical absorption edge energy values (a shift < 0.26 eV) was observed during temperature programmed reduction treatment in hydrogen (see Figure 6.7B). On the other hand, Ru-free Cs blank samples (not shown for the sake of brevity) showed XANES spectra with shapes similar to those corresponding to the 4Ru-N-4Cs-N sample, without any change during temperature programmed reduction treatment in hydrogen. This can be interpreted considering that the $CsNO_3$ decomposition originates a mixture of CsOH and Cs_2O species over the catalyst surface and these species seem to be more hardly reduced than CsCl preventing the cesium partial reduction.

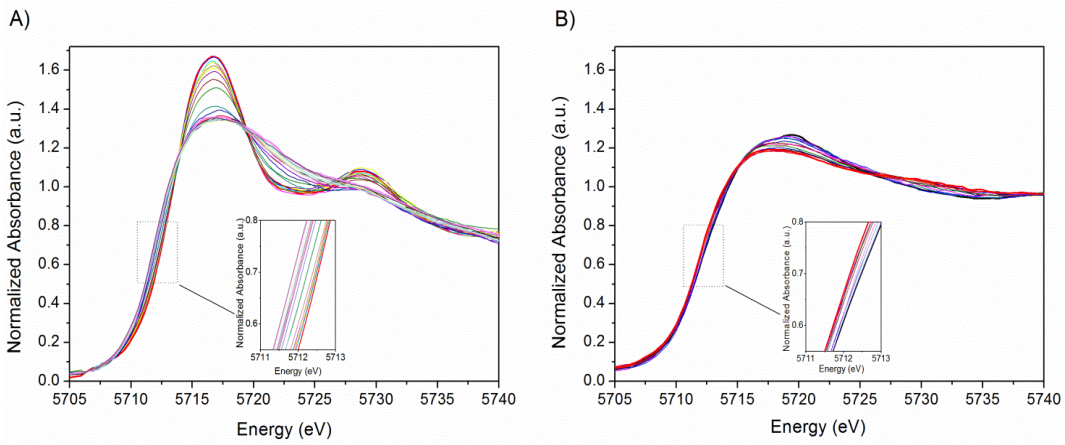

Figure 6.7. Cs L_1–edge XANES spectra collected during temperature programmed reduction in hydrogen and inset showing an enlargement of their absorption edges at the inflection point for 4Ru-Cl-4Cs-Cl (A) and 4Ru-N-4Cs-N (B) catalysts.

Fischer-Tropsch Synthesis. Promoted and unpromoted catalysts were tested at 523 K and 3.5 bar for the Fischer-Tropsch reaction to determine the effect of metal and promoter precursors. The evolution of CO conversion as a function of the reaction time is plotted in Figure 6.8. Most of the catalysts showed a slight decrease in activity during the first 4 hours of reaction before reaching stability, which is maintained during the time studied.

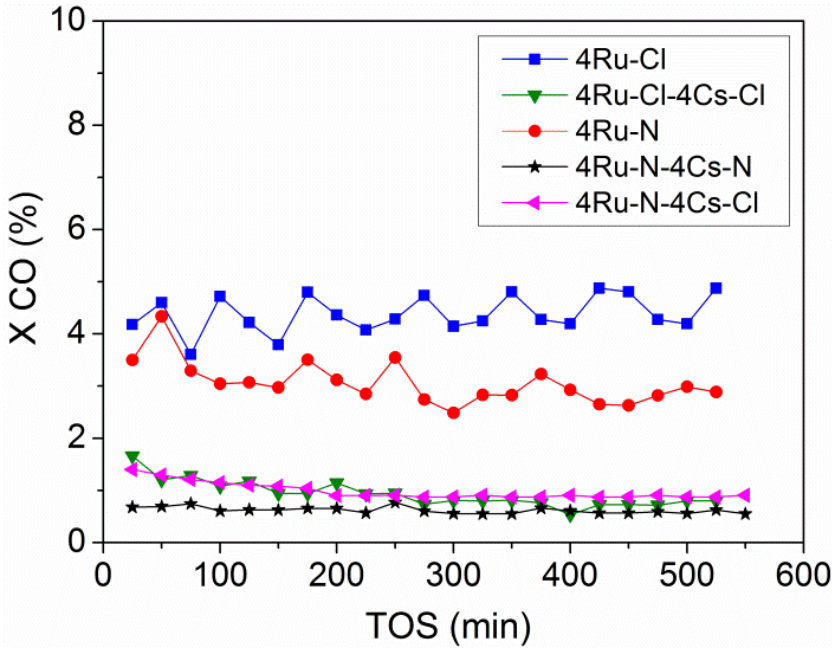

Figure 6.8. Time-on-stream (TOS) evolution of CO conversion during FTS at 523 K, 3.5 bar, flow rate = 45 cm^3 min^{-1} and $H_2/CO = 2$.

Steady-state catalytic results are compiled in Table 6.3 for all the catalysts. A comparison of the two unpromoted Ru catalysts reveals that they have basically the same catalytic activity but there are some differences in the product distribution. So, ex-chloride Ru catalyst shows higher selectivity for methane formation and lower olefin to paraffin ratio in the range of C_2-C_3 hydrocarbons. This agrees with earlier literature report [9] where the influence of the chlorine ions presence in Ru/SiO_2 catalysts for the FTS was studied. In our case only traces of chloride (as revealed by XPS analysis) remain on the reduced catalyst, therefore, no loss of activity with respect to the ex-nitrate catalyst was observed. The differences in product selectivity between the two Ru catalysts can be interpreted taking into account the above discussed microcalorimetry experiments. These latter show that CO adsorption heats for 4Ru-N sample are higher than for 4Ru-Cl for the whole coverage range which could imply that the dissociative

adsorption of CO is easier on the former. Typical product composition in the Fischer-Tropsch reaction is described by the Anderson-Schulz-Flory distribution [10,11]. Following this latter, long-chain-hydrocarbon formation involves the polymerization of CH_x species, formed from CO dissociation and subsequent C hydrogenation [12]. According to this mechanism the surface concentration of CH_x species and hydrogen atoms determine the growth of the hydrocarbon chain and the formation of paraffin or olefins. Therefore, the stronger CO adsorption for the 4Ru-N catalyst measured by microcalorimetry can be related with a higher population of adsorbed dissociative CO and the formation of CH_x species (which helps to increase the rate of C-C coupling [13]) on the catalyst surface, favoring the chain growth and the olefin formation. This reasoning is particularly evident when Cs is added to the Ru catalysts (compare 4Ru-N vs. 4Ru-N-4Cs-N and 4Ru-Cl vs. 4Ru-Cl-4Cs-Cl). The role of Cs promoter is evidenced by the lower activity for CO conversion, the increase of light olefins selectivity, the minor methane production and the increased chain growth probability (α) compared with the non-promoted catalyst for each pair of catalysts, independently of the precursor used. This kind of promotional effect (the so-called electronic effect) has been commonly observed for FTS catalysts involving group VIII metals [14, 15, 16, 17, 18]. This result is consistent with the increase in the CO adsorption heats by the presence of cesium compared to the non-promoted Ru catalyst observed by microcalorimetry (Figure 6.2). It is worth noting that comparing the two Cs promoted, 4Ru-Cl-4Cs-Cl and 4Ru-N-4Cs-N, catalysts only the latter produce an appreciable amount of CO_2. According to the literature [15, 19, 20], the action of alkaline in FTS is not only promoting the formation of C-C bonds, but also enhancing the water gas shift (WGS) reaction. The vast majority of the alkali

promoted catalysts studied for FTS contains the alkali oxide. The TPR-XANES of our two promoted catalysts showed that Cs in the reduced 4Ru-Cl-4Cs-Cl sample is as partially reduced CsCl, whereas in the reduced 4Ru-N-4Cs-N it is present in an oxygen environment as Cs_2O phase. These results indicate that though CsCl and Cs_2O have similar electro donating properties as revealed for their equal impact on the hydrocarbon distribution, only the Cs_2O enhance the activity for the WGS reaction. Therefore, throughout the pretreatment step in hydrogen atmosphere at 673 K of the 4Ru-N-4Cs-N catalyst, ruthenium precursor is decomposed liberating NO_x species. Also, cesium nitrate is decomposed remaining as a mixture of CsOH and Cs_2O species, which would bring the water molecules (produced during FT) closer and then they might interact with the adsorbed CO molecules on the Ru nanoparticles. The promoting effect of alkine oxides accelerating the WGS has been repeatedly reported. J.M. Campbell et al. [21] demonstrated that Cs introduction into Cu(110) enhanced the WGS rate by a factor of 5, due to the enhancement of H_2O byproduct activation over Cs. It was affirmed that a mixture of cesium-oxygen is present under reaction conditions. Richard G. Mallinson and coworkers also observed a high intrinsic activity for WGS when 2-4 wt% of Na was added to Pt particles [22]. Pt-NaO_x interactions provide highly active sites for the WGS reaction at the periphery of the Pt-NaO_x interface and also inhibit Pt particles from sintering. In order to further explore this phenomenon, an additional Cs promoted Ru catalyst was prepared using the ruthenium nitrate precursor but in this case it was promoted with the cesium chloride salt (Table 6.3, 4Ru-N-4Cs-Cl catalyst). It was observed that the CO_2 selectivity, mainly produced through WGS, significantly decreases, passing from 42 % to 7 % the CO_2 production. Moreover, 4Ru-N-4Cs-Cl catalyst has a FTS

performance identical to the 4Ru-Cl-4Cs-Cl and therefore, Cs remains as partially reduced CsCl presumably in both catalysts.

Table 6.3. Catalytic performance in the Fischer–Tropsch synthesis of Ru and Ru-Cs catalysts at 523 K and 3.5 bar.

3.5 bar	4Ru-N	4Ru-Cl	4Ru-N-4Cs-N	4Ru-N-4Cs-Cl	4Ru-Cl-4Cs-Cl
Activity (μmol/(g_{Ru} s))	6.2	8.5	1.0	2.1	2.0
CO conversion (%)	3.6	4.3	0.6	1.1	1.0
CO_2 selectivity (%)	6	2	42	7	7
TOF_{TEM} (s^{-1}) x 10^4	8.1	11.1	1.5	3.5	3.1
product distribution					
CH_4	72	82	46	65	63
C_2-C_6	28	18	54	35	37
α^a	0.57	0.56	0.68	0.62	0.64
O/P^b	0.3	0.1	3.4	2.3	2.8

Reaction conditions: CO/H_2/He (5/10/30, flow rate 45 mL/min), pressure 3.5 bar, temperature 523 K, catalyst (0.5 g), TOS 9 h. [a]The α value was calculated using the Anderson−Schulz−Flory (ASF) distribution in the hydrocarbon range of C_2-C_6. [b]The O/P value was calculated from the ratio of olefin divided by paraffin in the range of C_2-C_3 hydrocarbons.

Additional tests were carried out at medium pressure, 15 bar, to observe the performance of promoted and non-promoted catalysts under industrially relevant conditions. Figure 6.9 shows the time-on-stream (TOS) evolution of CO conversion during 50 h, where it is revealed that all the catalysts are stable throughout the studied reaction time. The maintained stability during 50 h fully supports the non-occurrence of the undesirable Boudouard reaction [23], which leads to the deposition of carbon blocking the active sites.

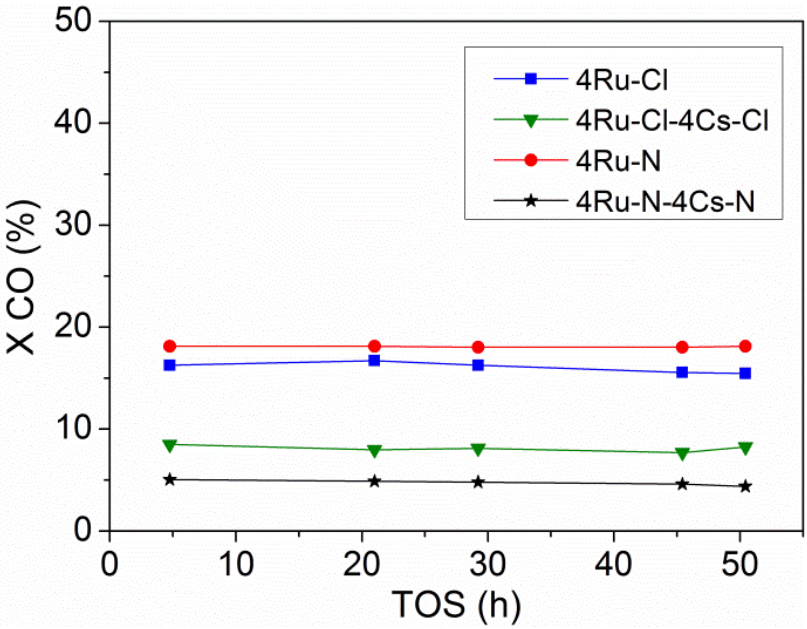

Figure 6.9. Time-on-stream (TOS) evolution of CO conversion during FTS at 523 K, 15 bar, flow rate = 45 cm^3 min^{-1} and $H_2/CO = 2$.

Catalytic properties at 15 bar for promoted and unpromoted Ru catalysts are presented in Table 6.4. It is observed an enhancement of both, the chain-growth probability (α) and the olefin selectivity (higher O/P ratio) by effect of the higher reaction pressure. In addition, the WGS reaction is diminished whereas the FT activity is enhanced, which is particularly evident for the 4Ru-N-4Cs-N catalyst.

Table 6.4. Catalytic performance in the Fischer-Tropsch synthesis of Ru and Ru-Cs catalysts at 523 K and 15 bar.

15 bar	4Ru-N	4Ru-Cl	4Ru-N-4Cs-N	4Ru-Cl-4Cs-Cl
Activity (μmol/(g_{Ru} s))	124	107	26	57
CO conversion (%)	18.1	15.5	4.4	8.2
CO_2 selectivity (%)	1	0	26	5
TOF_{TEM} (s^{-1}) x 10^3	16.1	14.0	3.8	10.1
product distribution				
CH_4	38	49	24	11
C_2-C_6	51	34	51	33
C_{7+}	11	17	25	56
α^a	0.68	0.76	0.86	1.0
O/P[b]	2.10	0.97	3.40	3.15

Reaction conditions: CO/H_2/He (5/10/30, flow rate 45 mL/min, pressure 15 bar, temperature 523 K, catalyst (0.5 g), 50 h. [a]The α value was calculated using the Anderson−Schulz−Flory (ASF) distribution in the hydrocarbon range of C_2-C_6. [b]The O/P value was calculated from the ratio of olefin divided by paraffin in the range of C_2-C_3 hydrocarbons.

6.2. References

[1] M. Cerro-Alarcón, A. Maroto-Valiente, I. Rodríguez-Ramos, A. Guerrero-Ruiz, *Carbon* 43 (2005) 2711-2722.

[2] A. Guerrero-Ruiz, E. Gallegos-Suarez, L. Gonzalo-Chacón, I. Rodríguez-Ramos, *Thermochim. Acta* 567 (2013) 112-117.

[3] M. Guraya, S. Sprenger, W. Rarog-Pilecka, D. Szmigiel, Z. Kowalczyk, M. Muhler, *Appl. Surf. Sci.* 238 (2004) 77-81.

[4] K. Aika, K. Shimazaki, Y. Hattori, A. Ohya, S. Ohshima, K. Shirota, A. Ozaki, *J. Catal.* 92 (1985) 296-304.

[5] I. Rossetti, L. Sordelli, P. Ghigna, S. Pin, M. Scavini, L. Forni, *Inorg. Chem.* 50 (2011) 3757-3765.

[6] M. Fernández-García, C. Márquez, G. L. Haller, *J. Phys. Chem.* 99 (1995) 12565-12569.

[7] C. Márquez-Alvarez, I. Rodríguez-Ramos, A. Guerrero-Ruiz, G. L. Haller, M. Fernández-García, *J. Am. Chem. Soc.* 119 (1997) 2905-2914.

[8] J. L. Eslava, A. Iglesias-Juez, G. Agostini, M. Fernández-García, A. Guerrero-Ruiz, I. Rodríguez-Ramos, *ACS Catal.* 6 (2016) 1437-1445.

[9] E. lyagaba, E. Hoost, J. Nwalor, J.G. Goodwin Jr, *J. Catal.* 123 (1990) 1.

[10] H. Schulz, *Appl. Catal. A: Gen*. 186 (1999) 3-12.

[11] G. P. van der Laan, A. A. C. M. Beenackers, *Catal. Rev. Sci. Eng.* 41 (1999) 255-318.

[12] R. A. van Santen, I. M. Ciobica, E. van Steen, M. M. Ghouri, *Adv. Catal.* 54 (2011) 127-187.

[13] J. Chen, Z.-P. Liu, *J. Am. Chem. Soc.* 130 (2008) 7929-7937.

[14] T. E. Hoost, J. G. Goodwin Jr, *J. Catal*. 137 (1992) 22-35.

[15] N. Lohitharn, J. G. Goodwin Jr, *J. Catal*. 260 (2008) 7-16.

[16] M. Guraya, S. Sprenger, W. Rarog-Pilecka, D. Szmigiel, Z. Kowalczyk, M. Muhler, *Appl. Surf. Sci.* 238 (2004) 77-81.

[17] K. Aika, K. Shimazaki, Y. Hattori, A. Ohya, S. Ohshima, K. Shirota, A. Ozaki, *J. Catal*. 92 (1985) 296-304.

[18] Z. Kowalczyk, M. Krukowski, W. Raróg-Pilecka, D. Szmigiel, J. Zielinski, *Appl. Catal*. A 248 (2003) 67-73.

[19] H. M. Torres-Galvis, KP. De Jong, *ACS Catal*. 3 (2013) 2130-2149.

[20] Q. H. Zhang, J.C. Kang, Y. Wang, *ChemCatChem* 2 (12) 10-1058.

[21] J. M. Campbell, J. Nakamura, C.T. Campbell, *J. Catal*. 136 (1992) 24-42.

[22] X. Zhu, M. Shen, L. L. Lobban, R. G. Mallinson, *J. Catal*. 278 (2011) 123-132.

[23] M. E. Dry, *Catal. Today* 71 (2002) 227-241.

Chapter 7

Effect of Mo promotion on the activity and selectivity of Ru/Graphite catalysts for Fischer-Tropsch synthesis

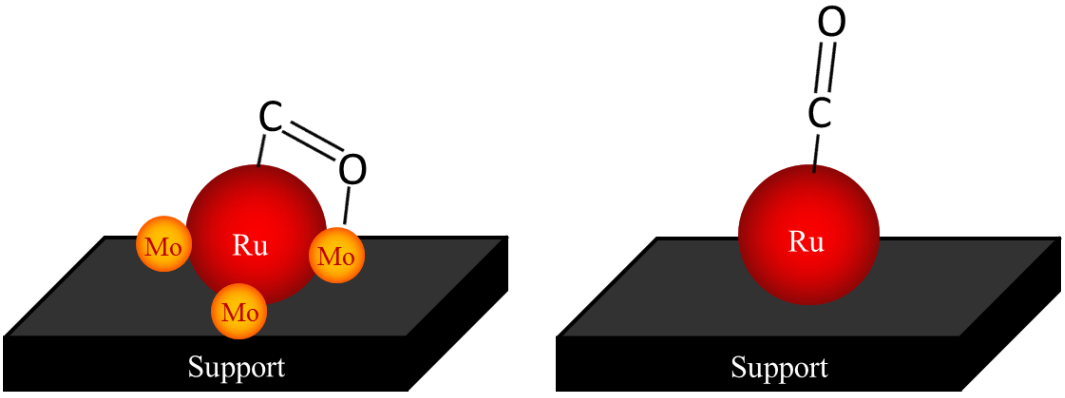

We present here molybdenum oxide promoted graphite supported ruthenium catalysts highly active and selective for Fischer-Tropsch synthesis (FTS). The effects of Mo loading (0-5 wt%) on Ru (2 wt%) were studied at 523 K, $H_2/CO = 2$ and 3.5 bar. Mean diameters of Ru were all close to 3 nm independently of the molybdenum loading used. Microcalorimetric characterization during CO adsorption at 330 K reveals a clear interaction between Ru and Mo observing an important increase of CO adsorption heats when Mo/Ru ratio was ≤ 0.26 . XPS performed to 2Ru0.5Mo/G catalyst after in-situ reduction showed the presence of Mo^{VI} (MoO_3) and Mo^{IV} (MoO_2) species on the catalyst surface which could be located around the ruthenium nanoparticles acting as a Lewis acid and therefore facilitating the CO dissociation. Mo promotion increased the activity with respect to unpromoted Ru catalyst 4 times, increased the selectivity to C_{5+} products and improved the olefin to paraffin ratio in the C_2-C_3 hydrocarbons range. These conclusions contribute to understand the Mo promotion effect in the FTS, because realistic deductions have been be obtained using a proper inert support for studying the molybdenum promotion effect in ruthenium based catalysts, avoiding strong metal-support interaction effects.

7.1 Results and Discussion

Catalysts Characterization. Table 7.1 summarizes the chemical composition of the prepared catalysts.

Table 7.1. Ruthenium and molybdenum loadings for all catalysts

Catalyst	Ru (wt%)	Mo* (wt%)
2Ru/G	1.98	-
2Ru0.05Mo/G	2.04	0.05
2Ru0.1Mo/G	2.03	0.10
2Ru0.5Mo/G	2.02	0.50
2Ru1Mo/G	2.05	1.00
2Ru5Mo/G	2.01	5.00

*Nominal content of Mo wt%.

Figure 7.1 shows the TPR profiles of the non-promoted and Mo promoted ruthenium catalysts. Ru monometallic catalyst shows one peak of hydrogen consumption centered at 360 K which corresponds to the reduction of the salt precursor to metallic ruthenium [1, 2, 3]. At temperatures above 500 K hydrogen is also consumed due to the partial gasification of the carbon support around metallic particles to give CH_4, as previously reported for other carbon supported Ru catalysts [1,4]. When molybdenum promoter is added the position of this peak shifted toward higher value and also it becomes wider (e.g. 2Ru0.5Mo catalyst the peak position is centered at 372 K). The amount of hydrogen consumption corresponding to this peak increases with the molybdenum loading, suggesting that the peak has to be associated with the reduction of not only Ru but also Mo as will be discussed later. The TPR profiles of promoted Ru catalysts show also the peak corresponding to the gasification of the support, but it is less marked than that observed for the Ru monometallic catalyst. These results reveal the reduction in catalytic activity for methane production by the gasification of the carbon support when molybdenum is added as promoter to Ru and can be indicative of specific metal-promoter interactions. Therefore, the TPR patterns of the promoted Ru catalysts indicate close proximity of molybdenum and ruthenium. From the

TPR characterization, it can be assured that all the catalysts are completely reduced during the treatment in hydrogen at 673 K.

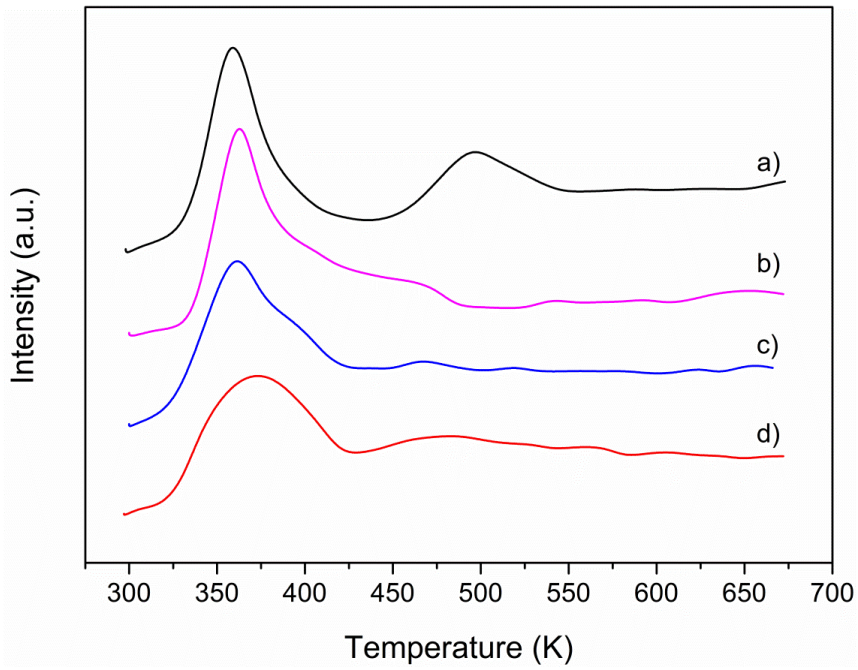

Figure 7.1. Hydrogen consumption profiles during temperature programmed reduction for: (a) 2Ru/G, (b) 2Ru0.05Mo/G, (c) 2Ru0.1Mo/Gand (d) 2Ru0.5Mo/G catalysts.

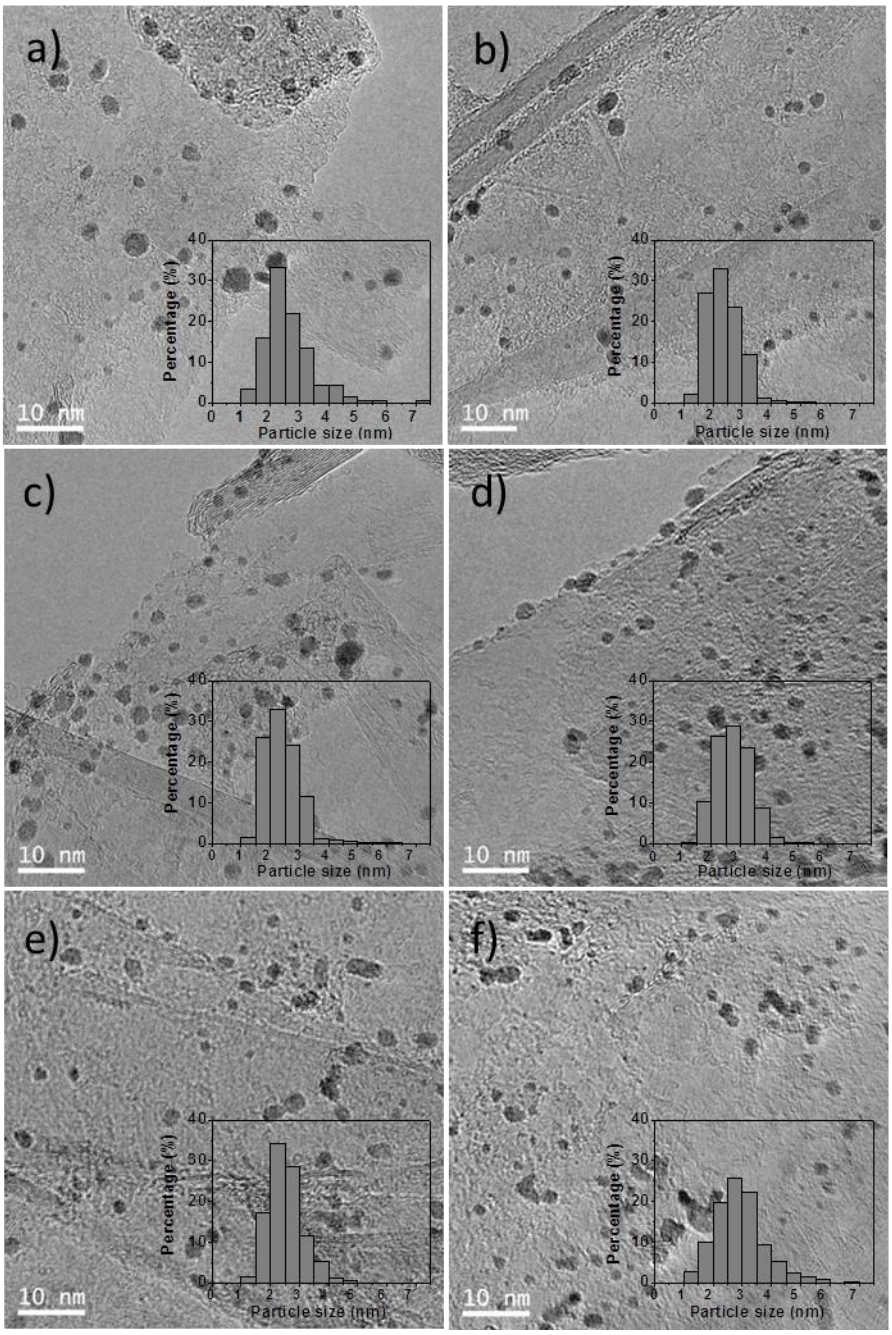

Figure 7.2. Particle size distribution and TEM images of reduced Ru catalysts. (a) 2Ru/G, (b) 2Ru0.05Mo/G, (c) 2Ru0.1Mo/G, (d) 2Ru0.5Mo/G, (e) 2Ru1Mo/G, (f) 2Ru5Mo/G.

Representative TEM images of the reduced catalysts and histograms with particle size distributions are shown in Figures 7.2. Table 7.2 summarizes the mean particle sizes calculated from the TEM measurements. The TEM images of

the catalysts show that the inclusion of Mo in the catalyst formulation does not significantly affect the distribution of particle sizes in the catalysts. Only in the case of the catalyst with the highest Mo loading, 2Ru5Mo/G, some broadening and shift to higher particle sizes is observed. So, small changes in particle sizes were observed since mean diameters of Ru nanoparticles were all between 3 and 3.6 nm (see Table 7.2).

Table 7.2. Main characteristics of the unpromoted and Mo promoted Ru catalysts.

Catalyst	d_{TEM} (nm)	CO uptake ($\mu mol/g_{Cat}$)
2Ru/G	3.4	22
2Ru0.05Mo/G	3.4	28
2Ru0.1Mo/G	3.0	35
2Ru0.5Mo/G	3.3	27
2Ru1Mo/G	3.0	22
2Ru5Mo/G	3.6	20

Surface composition and electronic state of Ru and Mo in 2Ru/G and 2Ru0.5Mo/G catalysts reduced in hydrogen at 673 K were investigated by XPS. Table 7.3 compiles the data obtained from the analysis of the XPS spectra.

Table 7.3. Data of XPS spectra analysis for the Ru catalysts.

Catalyst	B.E. (eV)		XPS ratios	
	Ru $3p_{3/2}$	Mo $3d_{5/2}$*	Ru/C	Mo/C
2Ru/G	461.54	-	0.0014	-
2Ru0.5Mo/G	461.54	226.28 (Mo^0, 16.8%)	0.0041	0.0010
		228.21 (Mo_2C, 35.2%)		
		229.10 (MoO_2, 20.1%)		
		232.26 (MoO_3, 27.9%)		

* Between brackets the relative percentage of the different Mo species.

Ru 3*p* core-level spectra of the Ru catalysts are shown in Figure 7.3. The binding energy of Ru $3p_{3/2}$ was of 461.54 eV for both promoted and unpromoted

catalysts, which is assigned in the literature to reduced forms of ruthenium [5]. The distribution of the oxidation states for molybdenum in the 2Ru0.5Mo/G catalyst was determined by deconvolution of the Mo 3d envelope and it is shown in Figure 7.4. The Mo 3d spectrum exhibits a complex envelope in accordance with different Mo components at the surface. The dominant peak of Mo $3d_{5/2}$ at 228.21 eV is consistent with the carbidic phase [6, 7]. Moreover the peak fitting suggests that there are three oxidation states for Mo ($3d_{5/2}$ Mo^{VI} (MoO_3), $3d_{5/2}$ Mo^{IV} (MoO_2) and $3d_{5/2}$ Mo^0 at 232.26, 229.10 and 226.28 eV respectively) at the surface [7, 8, 9, 10, 11]. It was found that the XPS peak fitting gives 27.9% of surface Mo atoms corresponding to Mo^{VI} (MoO_3), 20.1% Mo^{IV} (MoO_2), 16.8% Mo^0 and 35.2% of surface Mo corresponding to Mo_2C (see Table 7.3.). The formation of reduced species of Mo, particularly Mo^0, is likely brought about by H species coming from the dissociative chemisorption of H_2 on Ru and confirms the close contact of Ru and Mo species envisioned in the TPR experiments. Moreover, the formation of Mo carbide is understood is we consider that during reduction treatment at 673 K some methane is evolved by carbon gasification, which easily may originate the Mo carburization.

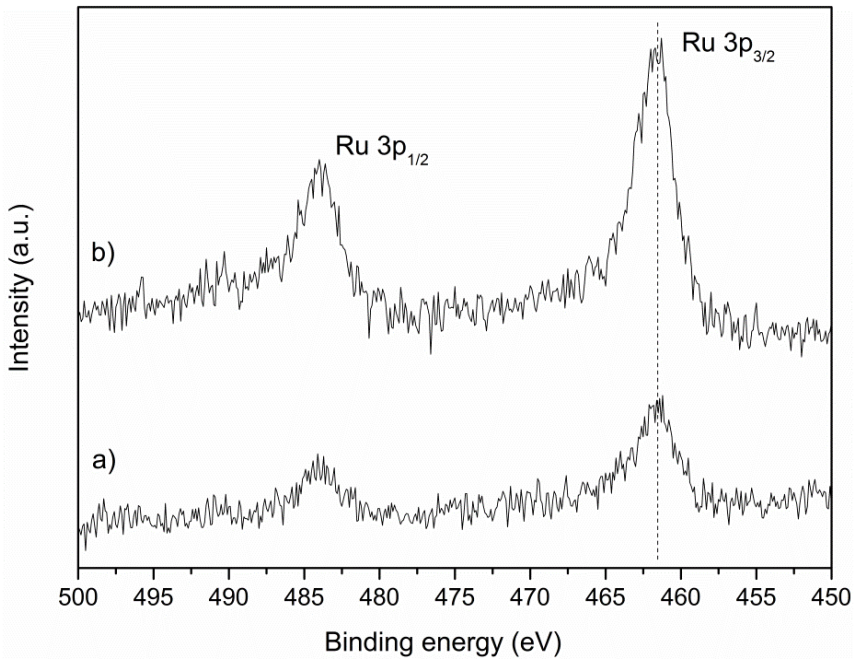

Figure 7.3. XPS spectra in the Ru 3*p* region for 2Ru/G (a) and 2Ru0.5Mo/G (b) catalysts after in-situ reduction treatment at 673 K.

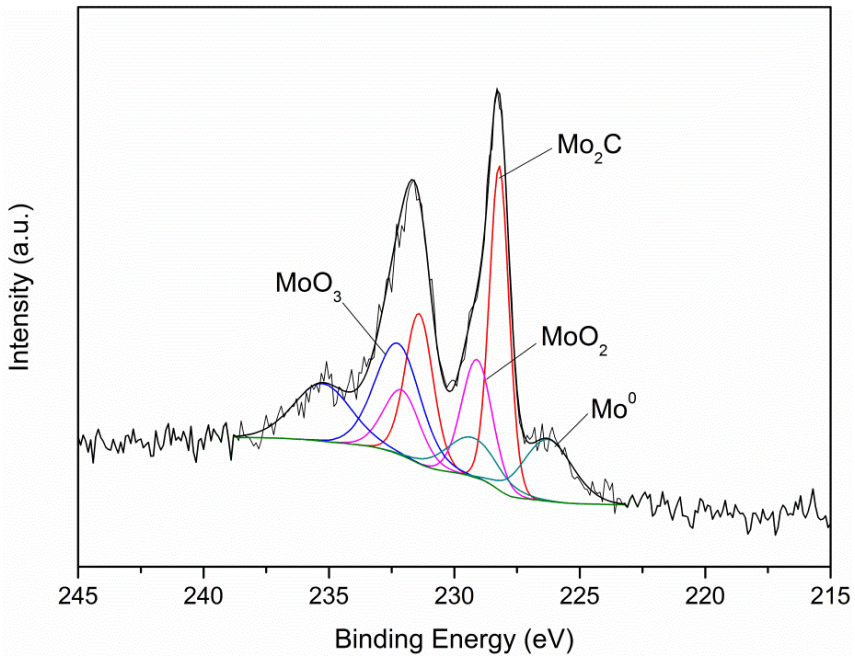

Figure 7.4. XPS spectra in the Mo 3*d* region for 2Ru0.5Mo/G catalyst after in-situ reduction treatment at 673 K.

To investigating the strength and energetic distribution of the surface sites on the catalysts for CO adsorption microcalorimetric measurements were performed. Figure 5 presents the microcalorimetric CO adsorption profiles. The monometallic Ru catalyst shows an initial adsorption heat value of 115 kJ/mol which is maintained approximately constant for surface coverages from 0.1 to 0.6 and finally drops down to 40 kJ/mol (physisorption values). Comparing the Ru monometallic catalyst versus Ru promoted with molybdenum catalysts at low wt% (2Ru vs 2Ru0.05, 2Ru0.1Mo and 2Ru0.5Mo), it is observed an important increase of CO adsorption heats throughout the experiment, the initial CO adsorption heat being of around 120 kJ/mol for the Mo promoted catalysts. It could be explained because the CO molecule might bind to metal oxides of Mo through the O atom while being simultaneously bound to the Ru metal through the C atom [12, 13, 14, 15] increasing significantly the adsorption heat with respect to the monometallic catalyst of Ru. In this system, the Mo oxide would act as a Lewis acid drawing electron density from the O atom and strengthening the bond of the CO molecule with the catalyst surface.

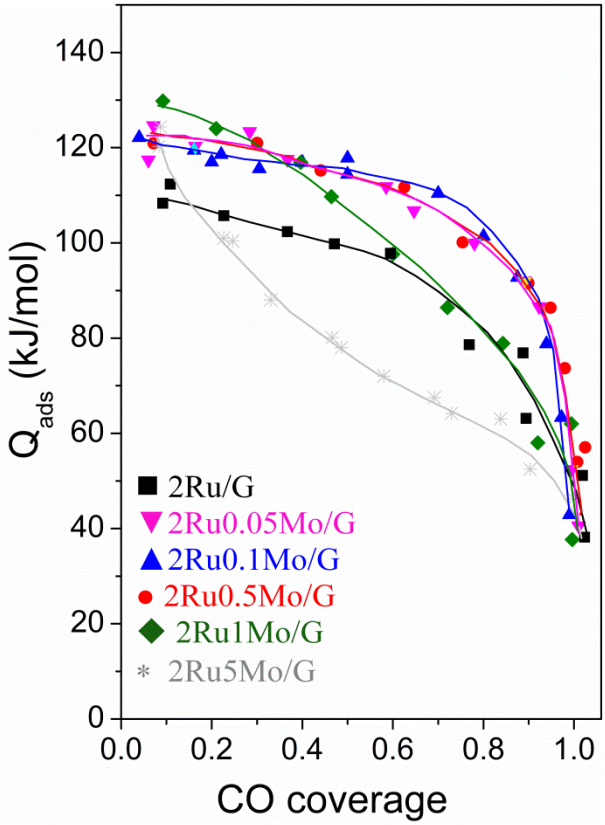

Figure 7.5. Differential heats of CO adsorption at 331 K as a function of surface coverage for all the catalysts.

When the Mo loading is higher than 0.5 wt% the plateau observed within 0.1 to 0.6 coverages disappears and a continuous decline of the CO adsorption heat occurs along the experiment. In the case of 2Ru1Mo sample it is observed that only at coverages between 0.1-0.5 the CO adsorption heats are higher than those corresponding to the monometallic catalyst of Ru. For larger CO coverages, the adsorption profile is similar to Ru monometallic catalyst. This fact indicates a partial segregation of metal phases in this catalyst. So, part of the molybdenum promoter likely as oxide form is located around some of the ruthenium nanoparticles participating in the adsorption of CO molecules to the catalyst surface, but there are also some Mo free Ru nanoparticles with similar behavior to that of the monometallic catalyst of ruthenium. In addition, there is an excess of

molybdenum and it may form agglomerates which do not affect the adsorption behavior of the Ru nanoparticles. A similar phenomenon was observed recently by G. R. Johnson et al. [12] in a study where Mn promoted Co/SiO_2 was used. It was found that Mn is accumulated preferentially on the surface of Co nanoparticles at low Mn loadings but at higher promoter loadings (Mn/Co > 0.1), larger Mn oxide particles were formed, which are considered to act as spectators having no influence on the CO adsorption. Finally, 2Ru5Mo catalyst shows an initial adsorption heat (120 kJ/mol) similar to that shown for the rest of the promoted catalysts. But for coverages higher than 0.1 a continuous and sharp decay of the differential heats is observed to CO adsorption heats lower than those of the ruthenium monometallic catalyst. In this case the agglomerates of molybdenum formed could cover part of Ru metal exposed on the surface and the surface sites with lower adsorption heats could be assigned to the Mo carbide phase. This is in agreement with the reported CO adsorption ability on different sites of Mo carbide [16, 17] as well as its potential activity for the CO hydrogenation reaction [18]. Numerous studies have investigated the catalytic activity of molybdenum carbide in reactions traditionally catalyzed by transition metals in order to be used as an alternative.

CO uptakes for all the catalysts are presented in Table 7.2. It can be seen that the Mo promotion increases the amount of CO adsorbed, the highest CO uptake being reached when the Mo/CO ratio is low. Specifically, 2Ru0.1Mo catalyst presents the highest CO uptake (35 $\mu mol/g_{Cat}$) and 2Ru5Mo sample the lowest (20 $\mu mol/g_{Ru}$). Particularly in this latter catalyst the contribution of the surface molybdenum carbide sites to the CO adsorption is more important and likely dominates given the large amount of Mo loading in this catalyst. Therefore,

excessive coverage of molybdenum could block part of the active sites avoiding the accessibility of CO molecules to the surface of ruthenium nanoparticles as above discussed for the microcalorimetric measurements.

Fischer-Tropsch Synthesis. Promoted and unpromoted Ru catalysts were examined under FTS conditions at 523 K and at 3.5 bar. Equal amount of catalyst was used in all the experiments. Figure 6 shows the time-on-stream (TOS) evolution of CO conversion and reveals that after 550 min the reaction reaches stable steady state conditions.

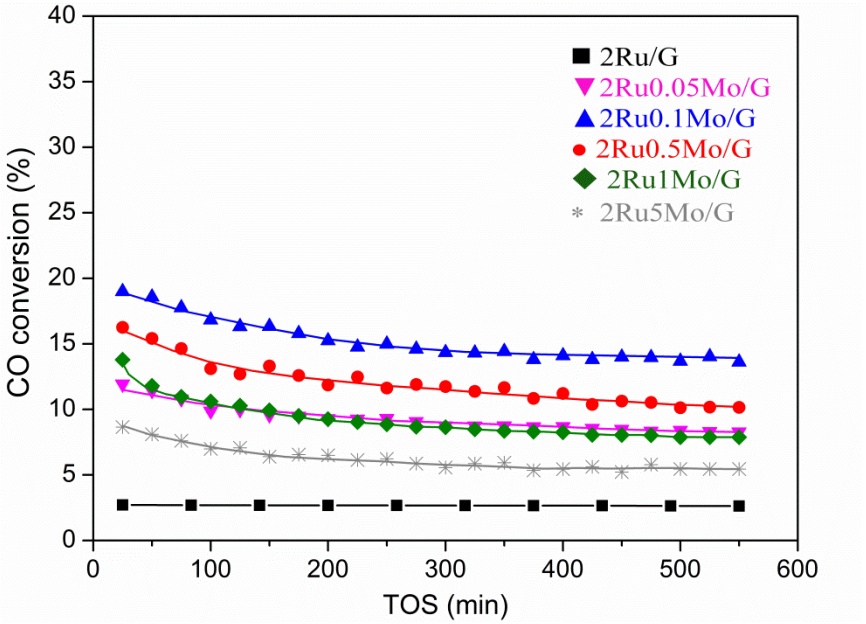

Figure 7.6. Time-on-stream (TOS) evolution of CO conversion during FTS at 523 K, 3.5 bar, $H_2/CO = 2$, GHSV = 5.4 $m^3_{STP}\ kg^{-1}_{cat}\ h^{-1}$ during 550 min.

Catalytic properties at a time on stream of 550 min for all Ru catalysts are presented in Table 7.4.

Table 7.4. Catalytic performance in the Fischer–Tropsch synthesis of Ru and Ru-Mo catalysts reduced at 673 K.

	2Ru/G[a]	2Ru0.05Mo/G[a]	2Ru0.1Mo/G[a]	2Ru0.5Mo/G[a]	2Ru1Mo/G[a]	2Ru5Mo/G[a]
d_{TEM} (nm)	3.4	3.4	3.0	3.3	3.0	3.6
TOF x 10^3 (s^{-1})	2.61	8.08	11.62	9.61	6.79	5.65
Activity ($\mu mol/g_{cat}$ s)	0.20	0.62	1.01	0.76	0.59	0.41
CO Conversion (%)	3	8	14	10	8	6
CO_2 Selectivity (%)	2	11	19	27	26	25
Product distribution:						
CH_4	83	47	45	45	40	36
C_2-C_4	14	36	38	40	46	48
C_{5+}	3	17	17	15	14	16
α^b	0.50	0.55	0.56	0.56	0.57	0.58
O/P[c]	0.27	0.35	0.41	0.36	0.36	0.38

[a] Reaction conditions: CO/H_2 (1/2, flow rate = 45 cm^3/min), pressure of 3.5 bar, temperature of 523 K, 0.5 g catalyst and a time on stream of 550 min.

[b] The α value was calculated using Anderson–Schulz–Flory (ASF) distribution in the hydrocarbon range of C_2–C_6.

[c] The O/P value was calculated from the ratio of olefin divided by total hydrocarbons paraffin in the range of C_2–C_3 hydrocarbons.

Comparing the catalytic activity of all the samples the role of Mo promoter on the high-surface-area-graphite-supported Ru catalysts under Fischer-Tropsch reaction conditions is evidenced by the higher activity for CO conversion, enhanced light olefins selectivity, lower methane production and increased chain growth probability (α) in comparison with the non-promoted catalyst. These promoting effects are consistent with those reported by other authors [19, 20, 21] over Ru-Mo catalysts supported on traditional metal oxide supports (SiO_2, Al_2O_3).

Turnover frequency (TOF) for CO conversion over the unpromoted and promoted Ru catalysts was calculated based on the Ru dispersion from TEM measurements. It is observed that 2 Ru0.1Mo/G catalyst presents the highest TOF value being 4 times greater than the activity shown by the non-promoted

ruthenium catalyst. Higher loadings of promoter decreased the rate but always the catalytic activity remains higher than the unpromoted catalyst. This fact agrees with the fact that the 2 Ru0.1Mo/G sample has the largest CO uptakes (Table 7.2) and with the conclusions obtained from CO chemisorption microcalorimetry (Figure 7.5) where higher CO adsorption heats were observed for Mo promoted catalysts when the Mo/Ru ratio is ≤ 0.26. It can be explained because part of the molybdenum promoter, likely as oxide form, might be located around the ruthenium nanoparticles acting as a Lewis acid drawing electron density from the O atom. According to Blyholder model [12, 13, 14, 22], it can be argued that at the same time the C-O bond strength decreases its dissociation is favored. A lower barrier for the CO dissociation leads to a higher surface coverage of adsorbed dissociative CO. In this way it is possible to say that during FT reaction a higher population of adsorbed dissociative CO and formation of CH_x species (which helps to increase the rate of C-C coupling) on the surface of promoted catalysts occur, favoring the chain grow and the olefin formation. At the same time the adsorption of H_2 is hindered on the surface active sites blocked by adsorbed CH_x species. This effect is directly involved in the increased production of olefins in the Mo-promoted catalyst, because the chain growth termination step by H_2 addition is suppressed. In addition, the hydrocarbon chains adsorbed at the ruthenium surface have a greater chance to grow, thereby resulting in longer hydrocarbon chains as products. The formation of long-chain-hydrocarbons in the Fischer-Tropsch reaction has been proposed to occur through the carbide mechanism which involves the polymerization of CH_x building blocks generated from syngas by CO dissociation followed by C hydrogenation [23] in accordance with the Anderson-Schulz-Flory distribution [24, 25, 26]. Using the ASF

distribution, we determined the chain growth probability (α) from the slope of the linear part of the plot. The α values change significantly on Mo addition, increasing from $\alpha = 0.50$ for the unpromoted catalyst to $\alpha = 0.58$ for 2Ru5Mo/G. Moreover, the results clearly indicate that Mo at the surface of the Ru particles at the same time that suppresses CH_4 formation by decreasing the likelihood of hydrogenation reaction in FTS, catalyzes partially the water gas shift reaction. Particularly, for the higher Mo loadings, 2Ru0.5Mo/G, 2Ru1Mo/G and Ru5Mo/G catalysts, selectivity towards CO_2 production of 25-27% was reached. The catalytic activity of Mo oxycarbide surfaces for the WGS reaction has been earlier reported [27].

To further analyze the Mo promoter effects, the changes in selectivity towards C_1 and C_{5+} and also the site time yield (STY) to C_{5+} for promoted and unpromoted catalysts are shown in Figure 7.7.

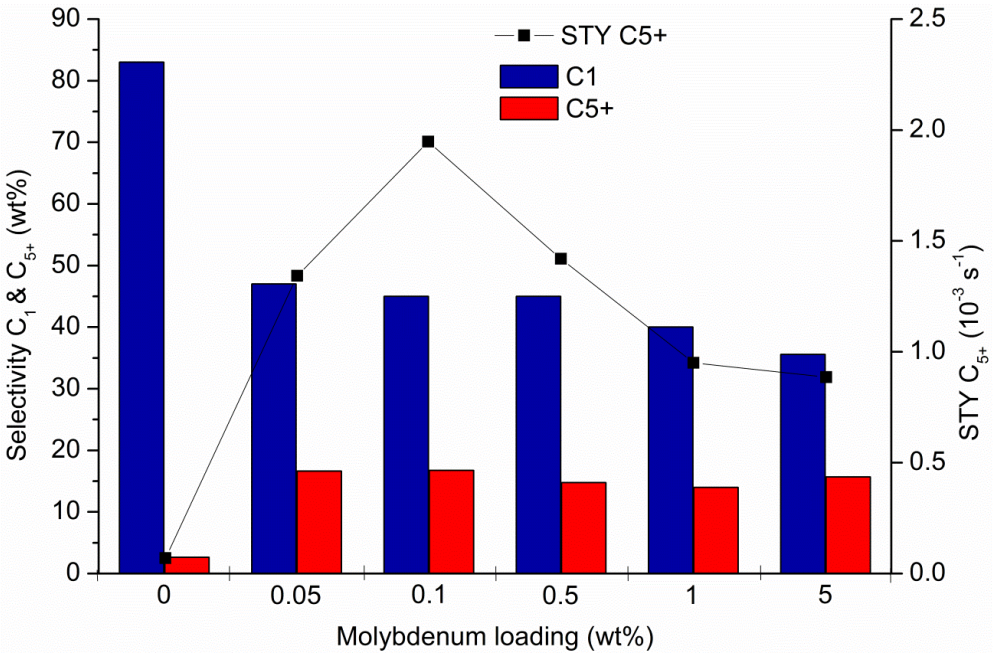

Figure 7.7. Influence of Mo loading on selectivity and site time yield to C_{5+} of 2 wt% Ru/G, measured at 523 K, 3.5 bar, $H_2/CO = 2$, GHSV = 5.4 m^3_{STP} kg^{-1}_{cat} h^{-1}. Reported data are for stable performance after 550 min of operation.

For all bimetallic catalysts the methane production is reduced increasing the C_{5+} one. This indicates an increased CO dissociation activity and decreased hydrogenation ability of ruthenium particles with the addition of Mo. Specifically, when the STY to C_{5+} ruthenium is considered, the 2Ru0.1Mo/G sample shows the highest value, this being 28 times higher than the value obtained for the ruthenium unpromoted catalyst. For higher Mo loadings the promotion effects are reduced though still observable with respect to the Ru monometallic catalyst. It seems that there is a Mo/Ru ratio (~0.05) for what presumably the number of Ru-Mo pairs, where the CO adsorption and FT reaction happen, is maximized.

7.2. References

[1] A. Guerrero-Ruiz, P. Badenes, I. Rodríguez-Ramos, Appl. Catal. A: Gen. 173 (1998) 313-321.

[2] B. Bachiller-Baeza, J. Álvarez-Rodríguez, A. Guerrero-Ruiz, I. Rodríguez-Ramos, Appl. Catal A: Gen. 333 (2007) 281-289.

[3] J. G. C. Shen, A. M. Liu, T. Tanaka, M. Ichikawa, J. Phys. Chem. B 102 (1998) 7782.

[4] B. Bachiller-Baeza, A. Guerrero-Ruiz, P. Wang, I. Rodríguez-Ramos, J. Catal. 204 (2001) 450-459.

[5] C. D. Wagner, W. M. Riggs, L. E. Davis, J. F. Moulder, G. E. Muilenberg, Handbook of X-Ray Photoelectron Spectroscopy, Perkin-Elmer Corp., Eden Prairie, Minnesota (1979) pp. 106.

[6] T. P. S. Clair, S. T. Oyama, D. F. Cox, S. Otani, Y. Ishizama, R.-L. Lo, K.-I. Fukui, Y. Iwasawa, Surf. Sci. 426 (1999) 187.

[7] A. G. Constant, J.-M. Giraudon, G. Leclercq, L. Leclercq, Appl. Catal. A: Gen. 260 (2004) 35-45.

[8] K. Oshikawa, M. Nagai, S. Omi, J. Phys. Chem. B 105 (2001) 9124-9131.

[9] C. Wan, Y. N. Regmi, B. M. Leonard, Angew. Chem. 126 (2014) 6525-6528.

[10] D. J. Moon, J. W. Ryu, Catal. Lett. 92 (2004) 17-24.

[11] T. St. Clair, S. T. Oyama, D. F. Cox, S. Otani, Y. Ishizawa, R.-Li. Lo, K.-I. Fukui, Y. Iwasawa, Surf. Sci. 426 (1999) 187-198.

[12] G. R. Johnson, S. Werner, A. T. Bell, ACS Catal. 5 (2015) 5888-5903.

[13] W. M. H. Sachtler, M. J. Ichikawa, J. Phys. Chem. 90 (1986) 4752-4758.

[14] A. B. Boffa, C. Lin, A. T. Bell, G. A. Somorjai, Catal. Lett. 27 (1994) 243-249.

[15] B. Bachiller-Baeza, I. Rodríguez-Ramos, A. Guerrero-Ruiz, Appl. Catal A: Gen. 205 (2001) 227-237.

[16] T. Wang, Q. Luo, Y.-W. Li, J.G. Wang, M. Beller, H.J. Jiao, Appl. Catal. A: Gen. 478 (2014)146-156.

[17] A. J. Medford, A. Vojvodic, F. Studt, F. Abild-Pedersen, J. K. Nørskov, J Catal. 290 (2012) 108-117.

[18] A. Griboval-Constant, J.-M. Giraudon, G. Leclercq, L. Leclercq, Appl. Catal. A: Gen. 260 (2004) 35-45.

[19] N. Takahashi, T. Mori, A. Miyamoto, T. Hattori, Y. Murakami, Appl. Catal. 22 (1986) 137-146.

[20] A. Juan, D. E. Damiani Catal. Today, 15 (1992) 469-480.

[21] M. J. P. Zurita, I. S. Henriquez, M. R. Goldwasser, M. L. Cubeiro, G. C. Bond, J. Mol. Catal. 88 (1994) 213-222.

[22] G. J. Blyholder, Phys. Chem. 68 (1964) 2772-2777.

[23] R. A. van Santen, I. M. Ciobica, E. van Steen, M. M. Ghouri, Adv. Catal. 54 (2011) 127-187.

[24] H. Schulz, Appl. Catal. A 186 (1999) 3-12.

[25] G. P. van der Laan, A.A.C.M. Beenackers, Catal. Rev. Sci. Eng. 41 (1999) 255–318.

[26] E. Iglesia, Appl. Catal. A 161 (1997) 50.

[27] P. Liu , J.A. Rodriguez, J. Phys. Chem. B, 110 (2006) 19418-25.

Chapter 8

General conclusions/Conclusiones generales

Several studies with Ru-based catalysts for the Fischer-Tropsch synthesis have been carried out in this PhD Thesis whose main conclusions are described next:

Time-Resolved XAS Investigation of the Local Environment and Evolution of Oxidation States of a Fischer-Tropsch Ru-Cs/C Catalyst.

Specially designed time-resolved X-ray absorption spectroscopy experiments, performed under programmed temperature reduction conditions and during FT reactant (H_2/CO) switching, have allowed us to unravel Fischer-Tropsch gas phase component interactions with the active metal Ru mediated by Cs promotion and to determine the electronic properties and local chemical environment of the metal and the promoter supported on graphite materials.

XANES analysis at both Ru K and Cs L_1 edges was carried out under TPR conditions. This allowed us to find that Ru reduction is a complex process, occurring in two steps via an intermediate oxidation state, and to show the concomitant Cs partial reduction. Time-resolved EXAFS analysis at the Ru K edge soundly proves the presence of Cs atoms as first neighbors of Ru. Fitting of the data gives structural parameters which match with Ru-Cs nanoparticles where the Cs atoms are surrounding the Ru cluster. In addition, the Ru-Cs particle morphology is reversely changed (from flat 2D to 3D shape with low first- and second-shell coordination numbers) when the H_2 atmosphere is switched to CO, staging the strong interaction of CO with the surface of the Ru-Cs nanoparticles supported on graphite. The latter has been straightforwardly measured by microcalorimetry of CO adsorption.

Therefore, our study provides sound evidence of the electronic interaction between Cs and Ru. The presence of the alkali metal leads to a stronger

interaction with the CO molecule. This in turn results in an increase of the adsorbed CO coverage and likely hinders the hydrogen adsorption, resulting in higher olefin selectivity and more long-chain hydrocarbon production in the Fischer-Trospch reaction.

Ruthenium particle size and cesium promotion effects in Fischer-Tropsch synthesis over high-surface-area graphite supported catalysts.

The influence of ruthenium particle size on the performance in FTS for Cs promoted and unpromoted high-surface-area-graphite supported catalysts has been studied. The use of a support with large surface area and weak interactions with Ru allows to independently study these effects without the influence of parasitic metal-support interactions. Microcalorimetric measurements of CO adsorption evidenced an increase in the heat of CO adsorption upon promoter addition. XPS demonstrates a clear interaction between Ru and Cs.

The *TOF* for CO conversion increases significantly with Ru particle size from 1.7 to 7.1 nm or 4.2 to 7.5 nm for unpromoted and promoted catalysts, respectively, and then change slightly up to 12 nm. The selectivity to C_{5+} hydrocarbons increases gradually with the Ru particle size for both series of catalysts. The O/P ratio over unpromoted catalysts decreases, whereas it remains constant over Cs promoted catalysts. Altogether, our results demonstrate the structure sensitive nature of FTS over Ru catalysts for Ru particles <7 nm, and highlight the great stability of these catalysts and the potential of Cs promotion for the preferential formation of waxes, even at high conversion levels.

Effect of Different Promoter Precursors in a Model Ru-Cs/HSAG System on the Catalytic Selectivity for Fischer-Tropsch Reaction.

Two different ruthenium and cesium precursors supported on a high surface area graphite material were used to prepare catalysts for application in the Fischer-Tropsch process. TPR experiments showed that cesium promoters shifted the ruthenium reduction temperature toward higher values and it was confirmed that Ru is completely reduced after the pretreatment step in hydrogen at 673 K for 2h for all catalysts. From CO chemisorption microcalorimetry measurements it was concluded that independently of the used metal and promoter precursor, cesium has an important contribution in the electronic properties of ruthenium nanoparticles producing a strengthening in the Ru-CO bond evidenced by higher CO adsorption heats. In particular, in the case of 4Ru-N-4Cs-N catalyst, the highest values of CO adsorption heats (throughout the analysis) were obtained due to the non-presence of residual chlorine species, since these latter withdraw electron density from the ruthenium nanoparticles decreasing the CO adsorption heats. Fischer-Tropsch reaction results revealed that all catalysts were stable throughout the experiment and therefore, the occurrence of the Boudouard reaction is discarded. The role of Cs was evidenced by an increase of the olefins-paraffins ratio, by a decrease in the methane production and consequently by higher formation of long-chain-hydrocarbons, either olefins or paraffins. Interestingly, the 4Ru-N-4Cs-N catalyst provided a high value of CO_2 production which can be related with its catalytic activity for WGS reaction. XANES analysis at Cs L_1 edge was recorded during the temperature-programmed reduction, observing a partial reduction of the CsCl species for the 4Ru-Cl-4Cs-Cl catalyst. By contrast, for the 4Ru-N-4Cs-N sample similar Cs spectrum with equal

absorption edge energy values were observed along all the H_2 TPR which is attributed to the formation of hardly reducible CsOH and Cs_2O species over the catalyst surfaces as consequence of the $CsNO_3$ precursor decomposition. These species are able to adsorb water molecules (co-product of the FT reaction), and then these water intermediates can interact with the CO molecules adsorbed on the Ru nanoparticles improving the WGS reaction and giving place to undesired production of CO_2.

Effect of Mo promotion on the activity and selectivity of Ru/Graphite catalysts for Fischer-Tropsch synthesis.

In this chapter we have shown that graphitic material (G) provides a suitable support for studying the molybdenum promotion effect in ruthenium based FT catalysis, because it enables the study of a transition metal oxide promoter effect without interference of support effects. Therefore, ruthenium properties can be influenced by the addition of Mo loadings as low as 0.05 wt%. The presence of molybdenum in a bimetallic ruthenium-molybdenum catalyst improves the catalytic behavior of ruthenium in terms of catalytic activity, long-chain hydrocarbon selectivity and the olefin-to-paraffin ratio. Thus promotion could be explained by assuming that molybdenum affects the dissociation rate of CO by weakening the CO bond. TEM images of the catalysts show that the addition of Mo does not significantly affect the mean diameters of the Ru nanoparticles so it is unlikely that the variations observed in catalyst activity and selectivity are attributable to particle size effects. Microcalorimetric CO adsorption profiles carried out at 330 K showed an important increase of CO adsorption heats for the Mo promoted samples with respect to ruthenium monometallic catalyst when the Mo/Ru atomic ratio was in the range 0.02 to 0.26. This fact was explained

because CO molecules might bind to metal oxides of Mo through the O atom while being simultaneously bound to the Ru metal through the C atom increasing significantly the adsorption heat. XPS performed to 2Ru0.5Mo/G catalyst after in-situ H_2 reduction treatment determined the presence of Mo^{VI} (MoO_3) and Mo^{IV} (MoO_2), MoC and Mo^0 species on the catalyst surface. The Mo particles could be located around the ruthenium nanoparticles acting as a Lewis acid and therefore facilitating the CO dissociation. These findings suggest that a performance-structure relationship may exist whereby higher special association between Ru and Mo is linked to improve the product selectivity in carbon monoxide hydrogenation. These conclusions represent a major contribution to the understanding of the Mo promotion effect in the FTS.

Conclusiones generales

En esta tesis doctoral se han llevado a cabo varios estudios con catalizadores basados en Ru para la síntesis de Fischer-Tropsch cuyas principales conclusiones se describen a continuación:

Investigación XAS Resuelta a Tiempo real del Entorno Local y de la Evolución de los Estados de Oxidación de un Catalizador de Fischer-Tropsch Ru-Cs/C.

Los experimentos de espectroscopia de absorción de rayos X fueron especialmente diseñados realizándose bajo condiciones de reducción a temperatura programada y durante la alternancia de los reactantes de FT (H_2/CO). Estos experimentos nos han permitido esclarecer las interacciones del gas de síntesis con el metal activo Ru promovido con Cs y determinar las propiedades

electrónicas y el ambiente químico local del metal y el promotor soportados en materiales de grafito.

Los análisis XANES realizados en ambos bordes, Ru-*K* y Cs-L_1, se llevaron a cabo en condiciones de TPR. Esto nos permitió descubrir que la reducción de Ru es un proceso complejo ocurriendo en dos etapas mediante la formación de un estado de oxidación intermedio, y además mostrar la reducción parcial de Cs. Los análisis EXAFS resueltos en el borde Ru-*K* demuestran la presencia de átomos Cs como primeros vecinos de Ru. El ajuste de los datos proporciona parámetros estructurales que coinciden con nanopartículas de Ru-Cs donde los átomos Cs están rodeando los agregados de Ru. Además, la morfología de las partículas de Ru-Cs se transforma de forma reversible (desde la forma plana 2D a la 3D con números bajos de coordinación en la primera y segunda capa) cuando la atmósfera de H_2 se cambia a CO, poniéndose de manifiesto una fuerte interacción del CO con la superficie de las nanopartículas Ru-Cs soportadas sobre grafito, hecho confirmado mediante microcalorimetría de adsorción de CO.

Por lo tanto, nuestro estudio proporciona pruebas sólidas de la interacción electrónica entre Cs y Ru. La presencia del metal alcalino conduce a una interacción más fuerte del Ru con las moléculas de CO. Esto a su vez da como resultado un aumento del cubrimiento de CO sobre la superficie del catalizador que probablemente obstaculiza la adsorción de hidrógeno, dando lugar a una mayor selectividad hacia olefinas y a la producción de hidrocarburos de cadena más larga en la reacción de Fischer-Trospch.

Efectos del tamaño de partícula de rutenio y de la promoción de cesio en la síntesis de Fischer-Tropsch empleando catalizadores soportados sobre grafito de alta superficie.

Se ha estudiado la influencia del tamaño de partícula de catalizadores de rutenio soportados sobre grafito de alta superficie promovidos o no con Cs sobre su comportamiento en la síntesis de FT. El uso de un soporte con gran área superficial e interacciones débiles con el Ru permite estudiar estos efectos de forma independiente sin la influencia de las interacciones parasitarias metal-soporte. Las mediciones microcalorimétricas de adsorción de CO evidenciaron un aumento en el calor de adsorción de CO tras la adición del promotor. XPS demostró una clara interacción entre Ru y Cs.

Se observó que el TOF para la conversión de CO aumenta significativamente con el tamaño de partícula de Ru desde 1,7 hasta 7,1 nm o desde 4,2 hasta 7,5 nm, dependiendo si se usan catalizadores de Ru no promovidos o promovidos respectivamente, y que se modifica levemente hasta tamaños de partículas de 12 nm. La selectividad hacia hidrocarburos C_{5+} aumenta gradualmente con el tamaño de partícula de Ru para ambas series de catalizadores. La relación O/P sobre los catalizadores no promovidos disminuye, mientras que permanece constante en los catalizadores promovidos con Cs. En conjunto, nuestros resultados demuestran la naturaleza sensible a la estructura de los catalizadores de Ru para la síntesis de FT en partículas de Ru <7 nm, destacan la gran estabilidad de estos catalizadores y el potencial de promoverlos con Cs conduciendo la selectividad hacia la preferente formación de ceras, incluso cuando se trabaja a altos niveles de conversión.

Efecto de diferentes precursores del promotor en un sistema modelo Ru-Cs/HSAG sobre la selectividad catalítica en la reacción de Fischer-Tropsch.

Se utilizaron dos precursores diferentes de rutenio y cesio para preparar catalizadores soportados sobre un material grafítico de alta superficie y aplicarlos en la reacción de Fischer-Tropsch. Los experimentos de TPR mostraron que los promotores de cesio desplazaron la temperatura de reducción de rutenio hacia valores más altos y se confirmó que el Ru se reduce completamente después del proceso de pretratamiento en hidrógeno a 673 K durante 2 h para todos los catalizadores. De las mediciones de microcalorimetría de quimisorción de CO se concluyó que independientemente del precursor metálico o del precursor del promotor utilizado, el cesio tiene una contribución importante en las propiedades electrónicas de las nanopartículas de rutenio provocando un fortalecimiento en el enlace Ru-CO evidenciado por los mayores calores de adsorción de CO obtenidos. En particular, en el caso del catalizador 4Ru-N-4Cs-N, se obtuvieron los valores más altos de calores de adsorción de CO (a lo largo de todo el análisis) debido a la ausencia de especies de cloro residual, ya que éstas intervienen retirando parte de la densidad electrónica de las nanopartículas de rutenio disminuyéndose por consiguiente los calores de adsorción de CO. Los resultados de la reacción de Fischer-Tropsch revelaron que todos los catalizadores fueron estables a lo largo del experimento y, por lo tanto, se descartó la influencia de la reacción de Boudouard. El papel del Cs se evidenció debido al aumento en la relación olefinas-parafinas, debido a la disminución de la producción de metano y consecuentemente por la mayor formación de hidrocarburos de cadena larga, ya sea olefinas o parafinas. Curiosamente, el catalizador 4Ru-N-4Cs-N proporcionó

un alto valor de producción de CO_2 que puede relacionarse con su actividad catalítica en la reacción de WGS. Se registraron XANES en el borde Cs-L_1 durante la reducción a temperatura programada en H_2, observándose una reducción parcial de la especie CsCl en el catalizador 4Ru-Cl-4Cs-Cl. Por el contrario, en la muestra 4Ru-N-4Cs-N se observó un espectro XANES de Cs similar a lo largo de toda el TPR atribuyéndose a la formación de especies de CsOH y Cs_2O, apenas reducibles, originadas durante la descomposición de la sal de $CsNO_3$. Estas especies son capaces de adsorber moléculas de agua (subproducto de la reacción de FT) que podrían interaccionar con las moléculas de CO adsorbidas sobre las nanopartículas de Ru promoviendo la reacción de WGS y por lo tanto dando lugar a la producción no deseada de CO_2.

Efecto de la promoción de Mo sobre la actividad y selectividad de catalizadores Ru/Grafito para la síntesis de Fischer-Tropsch.

En este capítulo hemos demostrado que el material grafítico (G) es un soporte adecuado para el estudio del efecto promotor de molibdeno en catalizadores de rutenio para la síntesis de FT, ya que permite centrarse en el efecto del promotor sobre el metal evitándose las interferencias no deseadas producidas por la interacción entre el metal y el soporte. Así, las propiedades catalíticas del rutenio pueden ser modificadas por la adición de cargas de Mo tan bajas como 0.05% en peso. La presencia de molibdeno en un catalizador bimetálico Ru-Mo mejora el comportamiento catalítico del rutenio en términos de actividad, selectividad hacia hidrocarburos de cadena larga y la relación entre olefinas-parafinas. Este efecto podría explicarse asumiendo que el molibdeno afecta a la disociación de CO mediante la debilitación del enlace entre el C-O. Las imágenes TEM de los catalizadores muestran que la adición de Mo no afecta

significativamente los diámetros medios de las nanopartículas de Ru por lo que es poco probable que las variaciones observadas en la actividad y la selectividad del catalizador sean atribuibles a los efectos del tamaño de partícula. Los perfiles de microcalorimetría de adsorción de CO llevados a cabo a 331 K mostraron un aumento importante de calores de adsorción en las muestras promovidas con Mo respecto al catalizador monometálico de rutenio. Este fenómeno se observó para una relación atómica Mo/Ru comprendida entre 0.02-0.26. Este hecho fue explicado porque las moléculas de CO podrían unirse a los óxidos de Mo a través del átomo de O mientras que al mismo tiempo enlazarse al metal de Ru a través del átomo de C aumentando significativamente el calor de adsorción. El análisis de XPS realizado a la muestra 2Ru0,5Mo/G después de la reducción in-situ en H_2, determinó la presencia de Mo^{VI} (MoO_3) y Mo^{IV} (MoO_2), MoC y Mo^0 en la superficie del catalizador. Las partículas de Mo podrían estar localizadas alrededor de las nanopartículas de rutenio actuando como un ácido de Lewis y por lo tanto facilitando la disociación de CO. Estos hallazgos sugieren que existe una relación óptima entre Ru y Mo en cuanto a comportamiento-morfología para la cual se produce una mejora de la selectividad hacia hidrocarburos en la reacción de hidrogenación de monóxido de carbono. Estas conclusiones representan importantes contribuciones a la comprensión del efecto promotor del Mo en la síntesis de Fischer-Tropsch.

Appendix I

Symbols and acronyms

List of Symbols

^{o}C	degree Celsius
D	Metal dispersion
D_{CO}	Particle size obtained from CO microcalorimetry
D_{XRD}	Particle size obtained from XRD
d_{TEM}	Particle size obtained from TEM
d	Distance between two consecutive planes
d_g	Grain diameter
d_r	Reactor diameter
Eb	Binding energy
E_C	Kinetic energy
G	Graphite
hυ	Photon energy
$k_{p,n}$	Velocity of propagation of the chain growth of n carbon
$k_{t,n}$	Termination rate of the chain of n carbon atoms
L_{CB}	Catalyst bed length
M	Molar volume
M_s	Metal atoms number on the surface
M_t	Total metal atoms number.
m/z	Mass / ion charge number
N_A	Avogadro number
N_s	Number of atoms per unit area of metal on the surface
N_v	Concentration of atoms per unit volume

n	Carbon number
n_i	Number of particles with diameter d_i
O/P	Olefin / paraffin ratio
P	Pressure
P_0	Saturation pressure of N_2 at -196 °C
Q_{ads}	CO adsorption enthalpy
S	Carbon selectivity
S_{BET}	Catalyst specific surface area
T	Temperature
V_{ads}	Adsorbed gas volume
Vm	Monolayer volume
W_n	Mass fraction of chain with n carbon atoms
wt%	Percentage by weight
X	Conversion
Y	Molar fraction
α	Growth probability factor
θ	Incidence angle
λ	Incident wavelength
σ	Cross-sectional area covered by N_2 molecule
Φ	Spectrometer work function

List of Acronyms

ASF	Anderson-Schulz-Flory
a.u.	Arbitrary Units
BET	Brunauer-Emmett-Teller
BTL	Biomass-to-Liquids
COD	Conversion of olefins to diesel
CPS	Counts per second
CTL	Coal-to-Liquids
DR	Dry reforming
EDXAS	Energy dispersive X-ray absorption spectroscopy
FID	Flame ionization detector
FT	Fischer Tropsch
FTS	Fischer Tropsch synthesis
GC	Gas chromatograph
GHSV	Gas hourly space velocity
GTL	Gas-to-Liquids
HRTEM	High resolution transmission electron microscopy
HSAG	High surface area graphite
HTFT	High temperature Fischer-Tropsch
IUPAC	International Union of Pure and Applied Chemistry
IWI	Incipient wetness impregnation

JCPDS	Joint Committee on Powder Diffraction Standards
LTFT	Low temperature Fischer-Tropsch
MFC	Mass flow controller
MS	Mass spectrometer
PC	Pressure controller
PCA	Principal component analysis
ppb	Parts per billon
ppm	Parts per million
TCD	Thermal conductivity detector
TEM	Transmission electron microscopy
TGA	Termogravimetric analysis
TOF	Turnover frecuency
TOS	Time-on-stream
TPD	Temperature programmed desorption
SMSI	Strong metal-support interaction
STEM	Scanning transmission electron microscopy
STP	Standard temperature and pressure
TPR	Temperature programmed reduction
TRXF	Total-reflection X-ray fluorescence
WGS	Water-Gas Shift
WI	Wetness impregnation
XANES	X-ray absorption near edge structure
XAS	X-ray absorption spectroscopy
XPS	X-ray photoelectron spectroscopy

XRD	X-ray diffraction

Appendix II

Tables index

Chapter 1: Introduction

Chapter 3: Experimental

Chapter 4: Time-Resolved XAS Investigation of the Local Environment and Evolution of Oxidation States of a Fischer-Tropsch Ru-Cs/C Catalyst

Chapter 5: Ruthenium particle size and cesium promotion effects in Fischer-Tropsch synthesis over high-surface-area graphite supported catalysts

Chapter 6: Effect of Different Promoter Precursors in a Model Ru-Cs/HSAG System on the Catalytic Selectivity for Fischer-Tropsch Reaction

Chapter 7: Effect of Mo promotion on the activity and selectivity of Ru/Graphite catalysts for Fischer-Tropsch synthesis

Appendix III

Figures index

Chapter 1: Introduction

Chapter 3: Experimental

Chapter 4: Time-Resolved XAS Investigation of the Local Environment and Evolution of Oxidation States of a Fischer-Tropsch Ru-Cs/C Catalyst

Chapter 5: Ruthenium particle size and cesium promotion effects in Fischer-Tropsch synthesis over high-surface-area graphite supported catalysts

Chapter 6: Effect of Different Promoter Precursors in a Model Ru-Cs/HSAG System on the Catalytic Selectivity for Fischer-Tropsch Reaction

Appendix IV

Publications derived from this Doctoral Thesis

ACS Catalysis

Research Article

pubs.acs.org/acscatalysis

Time-Resolved XAS Investigation of the Local Environment and Evolution of Oxidation States of a Fischer–Tropsch Ru–Cs/C Catalyst

José L. Eslava,[†] Ana Iglesias-Juez,[*,†] Giovanni Agostini,[‡] Marcos Fernández-García,[†,§] Antonio Guerrero-Ruiz,[§,∥] and Inmaculada Rodríguez-Ramos[*,†,§]

[†]Instituto de Catálisis y Petroleoquímica, CSIC, C/Marie Curie 2, 28049 Madrid, Spain

[‡]European Synchrotron Radiation Facility, 71 Avenue des Martyrs, 38000 Grenoble, France

[§]Grupo de Diseño y Aplicación de Catalizadores Heterogéneos, Unidad Asociada UNED-CSIC (ICP), 28040 Madrid, Spain

[∥]Departamento de Química Inorgánica y Química Técnica, UNED, C/Senda del Rey 9, 28040 Madrid, Spain

Supporting Information

ABSTRACT: Here we present a time-resolved in situ X-ray absorption spectroscopy investigation of the local chemical environment and the electronic structure of the active metal (Ru) and the promoter (Cs) present in catalysts supported over high-surface-area graphite. These catalysts were submitted to a reduction treatment under hydrogen gas and then to alternate atmospheres of Fischer–Tropsch reactants, CO/He, and H_2/He atmospheres, respectively. This study reveals that Ru reduction is a complex process taking place through a two-step mechanism via an intermediate oxidation state and occurs in parallel to the Cs partial reduction. It also demonstrates a close association between Cs and Ru atoms as first neighbors. The evidence that the Ru–Cs particle morphology reverses (from flat 2D to a 3D shape with low coordination numbers) when the H_2 atmosphere is changed with CO proves the strong interaction of CO with the surface of the Ru–Cs nanoparticles, a point confirmed by microcalorimetry of CO adsorption. To our knowledge, this is the first time that this reversible particle reconstruction upon syngas reactant switching has been demonstrated.

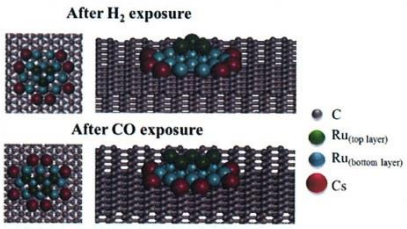

KEYWORDS: *ruthenium, cesium, electronic promoter, X-ray absorption spectroscopy, Fischer–Tropsch reaction*

INTRODUCTION

Fischer–Tropsch (FT) synthesis is a key technology which allows the transformation of synthesis gas, a mixture of CO and H_2 issued traditionally from natural gas or coal but at present derived from biomass, into clean hydrocarbons that are convenient substitutes for useful compounds such as naphtha, diesel, lubricants, and others produced by oil refining. Although iron, cobalt, and ruthenium are active catalysts for the FT reaction, Co and Fe are most commonly employed. However, ruthenium catalysts, despite their higher price, possess some unique features in FT synthesis. In comparison with Co, Ru catalysts possess higher intrinsic activity and can work under higher partial pressures of water or other oxygenate-containing atmospheres, this latter feature being particularly important for the conversion of syngas produced from biomass. In addition, Ru catalysts are suitable for fundamental research to gain insights into the catalyst functioning and/or reaction mechanisms.[1−4]

FT catalysts often contain chemical promoters such as alkali-metal elements. The presence of alkali metal increases both the activity and selectivity for high-molecular-weight hydrocarbons and also favors olefinic product formation.[5,6] Explanations for this enhanced activity/selectivity are often given in terms of the basicity of the alkali-metal promoter, which is suggested to increase the CO dissociative adsorption rate, resulting in an increase in the surface coverage of dissociated CO species. This in turn results in higher selectivities toward longer chain hydrocarbon and olefin products.[1,7] Moreover, groups working with alkali-metal-doped ruthenium-based catalysts have suggested, mainly on the basis of indirect evidence, that the alkali-metal element (Na, K, or Cs) is an electronic promoter which donates a part of its electron density to Ru even in its oxidized state.[5,8−10] According to these authors, the electron transfer from the promoter to the metal causes the strengthening of the CO–metal interaction, while the C–O bond is weakened. Recently, some experimental evidence of the partial reduction of Cs in ammonia synthesis Cs–Ru/C catalysts during temperature-programmed reduction has been provided by X-ray absorption spectroscopy.[11] On the other hand, there is another open debate in the literature, in addition to that on the oxidation state of the promoter, on the location of the alkali-metal promoter in the catalyst system. Different possible locations have been proposed where the alkali-metal atoms are sometimes assumed to be located inside or at the surface of the

Received: November 5, 2015
Revised: January 17, 2016
Published: January 19, 2016

DOI: 10.1021/acscatal.5b02489
ACS Catal. 2016, 6, 1437−1445

Articles in preparation

1) "Ruthenium particle size and cesium promotion effects in Fischer-Tropsch synthesis over high-surface-area graphite supported catalysts", José L. Eslava, Xiaohui Sun, Jorge Gascon, Freek Kapteijn and Inmaculada Rodríguez-Ramos. Submitted to Catal. Sci. Technol.

2) "Effect of Different Promoter Precursors in a Model Ru-Cs/HSAG System on the Catalytic Selectivity for Fischer-Tropsch Reaction", José L. Eslava, Ana Iglesias-Juez, Marcos Fernández-García, Antonio Guerrero-Ruiz and Inmaculada Rodríguez-Ramos. Submitted to Catal. Today.

3) "Effect of Mo promotion on the activity and selectivity of Ru/Graphite catalysts for Fischer-Tropsch synthesis", José L. Eslava, Esteban Gallegos-Suárez, Antonio Guerrero-Ruiz and Inmaculada Rodríguez-Ramos.